

College of Engineering
Virginia Polytechnic Institute & State University
Blacksburg, Virginia 24061

VPI-E-74-10

A FINITE DEFORMATION ANALYSIS OF THE
NEAR FIELD SURROUNDING THE TIP OF
CRACK-LIKE ELLIPSES

J. J. McGowan* and C. W. Smith**

Department of Engineering Science & Mechanics

May 1974

RETURN TO: AEROSPACE STRUCTURES
INFORMATION AND ANALYSIS CENTER
AFFDL/FBR
WPAFB, OHIO 45433

Reporting Period: 1973-74 Academic Year

Prepared For:

National Science Foundation
Washington, D. C.
Grant No. GK 39922

Approved for Public Release; distribution unlimited.

20000111 065

*Assistant Professor

**Professor

Department of Engineering Science & Mechanics
Virginia Polytechnic Institute & State University
Blacksburg, Virginia 24061

Reproduced From
Best Available Copy

1. Report No. 2. Government Accession No. 3. Recipient's Catalog No.

VPI-E-74-10

4. Title
A FINITE DEFORMATION ANALYSIS OF THE NEAR FIELD SURROUNDING THE TIP OF CRACK-LIKE ELLIPSES

7. Authors
J. J. McGowan and C. W. Smith

9. Performing Organization Name & Address
Department of Engineering Science & Mechanics
Virginia Polytechnic Institute & State University
Blacksburg, Virginia 24061

12. Sponsoring Agency Name and Address
National Science Foundation
Washington, D. C.

16. Abstract
A finite deformation analysis of the region surrounding the tip of small crack-like ellipses in an infinite plate under all around tension is presented. The study is carried out in the deformed geometry and includes the effects of finite strains and rotations. A stress function is first introduced to the complete compatibility equations through linear constitutive relations; the resulting governing equation is solved through finite differences. The range of root radii investigated varies from one to nine times that of a deformed crack. Normal stresses and strains, maximum in-plane shear stress, displacements and stress intensity factors are presented. The results of the analysis are compared to the linear analysis of Inglis. The effects of finite strains and rotations are shown to be large but are concentrated within a few root radii of the tip. It has been found that two types of behavior exist at the tip of notches, depending on the size of the root radius: small root radii produce maximum stresses away from the tip, whereas larger root radii produce maximum stresses at the tip itself.)

17. Key Words
Stress Fields, Crack Tips,
Finite Deformations,
Fracture Mechanics

18. Distribution Statement
Approved to Public
Release Distribution
Unlimited

19. Security Classif. (report)
Unclassified

20. Security Classif. (page)
Unclassified

NOMENCLATURE

$A_1-A_3, B_0-B_6, C_1-C_3$	Coefficients as defined in (2.7)
\vec{b}	Base vectors in the deformed system
\bar{c}	Dimensional 1/2 crack length as shown in Figure 2.2, mm
E	Young's modulus, N/mm ²
e^{ij}	Permutation tensor defined by (2.6)
F_{11}, F_{12}, F_{13}	Coefficients as defined in (2.5)
F_1, F_2, F_3	Coefficients as defined in (3.1)
g_{ij}, g^{ij}	Covariant and contravariant, respectively, deformed metric tensors nondimensionalized by $g_{ij} = \bar{g}_{ij}/\bar{c}^2 ; g^{ij} = \bar{g}^{ij}/\bar{c}^2$
h_{ij}, h^{ij}	Covariant and contravariant, respectively, undeformed metric tensors nondimensionalized by $h_{ij} = \bar{h}_{ij}/\bar{c}^2 ; h^{ij} = \bar{h}^{ij}/\bar{c}^2$
K	Stress intensity factor, N/mm ^{3/2}
K_{TH}	Theoretical stress intensity factor, N/mm ^{3/2}
K_{AP}	Apparent stress intensity factor, N/mm ^{3/2}
\vec{r}, \vec{r}_0	Position vector in the deformed and undeformed systems, respectively, mm
w_i, w^i	Covariant and contravariant displacements, respectively, nondimensionalized by $w_i = \bar{w}_i/\bar{c} ;$ $w^i = \bar{w}^i/\bar{c}$

x, y	Local cartesian coordinates nondimensionalized by $x = \bar{x}/\bar{c}$, $y = \bar{y}/\bar{c}$
$o_\beta - s_\beta$	Coefficients as defined in (3.2)
$\Delta, \Delta_1, \Delta_2, \Delta_3$	Coefficients as defined in (3.1)
ε	Perturbation parameter
ϵ_{ij}	Covariant strain tensor
$\epsilon_{ijk}, \epsilon_{ijkl}$	Strain functions as defined by (2.1)
$\vec{\zeta}$	Displacement vector
η, ξ	Local orthogonal curvilinear coordinates as shown in Figure 2.2
θ	Sum of physical normal stresses
ν	Poisson's ratio
ξ_0	Value of ξ at boundary of ellipse
ρ	Ellipse root radius nondimensionalized by $\rho = \bar{\rho}/\bar{c}$
$\bar{\sigma}$	Dimensional remote normal stress, psi
σ_{ij}, σ^{ij}	Covariant and contravariant, respectively, stress tensor nondimensionalized by $\sigma_{ij} = \bar{\sigma}_{ij}/\bar{\sigma}$, $\sigma^{ij} = \bar{\sigma}^{ij}/\bar{\sigma}$
τ_{max}	Maximum in-plane shear stress nondimensionalized by $\tau_{max} = \bar{\tau}_{max}/\bar{\sigma}$
Φ, ϕ	Outer and inner, respectively, stress function nondimensionalized by $\Phi = \bar{\Phi}/\bar{c}^2\bar{\sigma}$, $\phi = \bar{\phi}/\bar{c}^2\bar{\sigma}$
$ A $	Determinant of A_{ij}

v

Superscripts

-- Dimensional quantity

~ Physical quantity

^ Inner variable

* Outer variable

TABLE OF CONTENTS

	<u>Page</u>
NOMENCLATURE	iii
LIST OF FIGURES	vii
I. INTRODUCTION AND REVIEW OF THE LITERATURE	1
II. FORMULATION OF THE PROBLEM	5
A. Notation and Formulae	5
B. Perturbation Analysis	11
III. SOLUTION TO THE PROBLEM	16
A. Linearization of the Governing Equation	16
B. Finite-Difference Method	18
C. Internal Collocation Method	24
D. Integration of the Strain-Displacement Relations and Limit Analysis	25
IV. DISCUSSION OF THE RESULTS AND CONCLUSIONS	30
A. Discussion of the Results	30
B. Conclusions	37
ACKNOWLEDGEMENTS	38
REFERENCES	38
APPENDIX A	41
FIGURES	43

LIST OF FIGURES

<u>Figure</u>		<u>Page</u>
2.1 Coordinate System	43	
2.2 Problem Geometry	44	
2.3 Inner Region Geometry	45	
2.4 Perturbation Scheme	46	
3.1 One-Dimensional Finite Difference Schemes	47	
3.2 Two-Dimensional Finite Difference Schemes	48	
3.3 Grid Pattern	49	
3.4 Finite Difference Scheme Used for Strain Integration .	50	
4.1a Physical Normal Stress $\tilde{\sigma}_{nn}$ Distribution Along the Line of Symmetry for $\xi_0 = 1.0$	51	
4.1b Physical Normal Stress $\tilde{\sigma}_{nn}$ Distribution Along the Ellipse Border for $\xi_0 = 1.0$	52	
4.1c Physical Normal Stress $\tilde{\sigma}_{\xi\xi}$ Distribution Along the Line of Symmetry for $\xi_0 = 1.0$	53	
4.1d Apparent Stress Intensity Factor Distribution Along the Line of Symmetry for $\xi_0 = 1.0$	54	
4.1e Physical Maximum In-Plane Shear Stress Distribution for $\xi_0 = 1.0$	55	
4.1f Contravariant Displacement w^ξ Distribution Along the Line of Symmetry for $\xi_0 = 1.0$	56	
4.2a Physical Normal Stress $\tilde{\sigma}_{nn}$ Distribution Along the Line of Symmetry for $\xi_0 = 1.3$	57	
4.2b Physical Normal Stress $\tilde{\sigma}_{nn}$ Distribution Along the Ellipse Border for $\xi_0 = 1.3$	58	

<u>Figure</u>		<u>Page</u>
4.2c	Physical Normal Stress $\tilde{\sigma}_{\xi\xi}$ Distribution Along the Line of Symmetry for $\xi_0 = 1.3$	59
4.2d	Apparent Stress Intensity Factor Distribution Along the Line of Symmetry for $\xi_0 = 1.3$	60
4.2e	Physical Maximum In-Plane Shear Stress Distribution for $\xi_0 = 1.3$	61
4.2f	Contravariant Displacement w^ξ Distribution Along the Line of Symmetry for $\xi_0 = 1.3$	62
4.3a	Physical Stress $\tilde{\sigma}_{nn}$ Distribution Along the Line of Symmetry for $\xi_0 = 1.7$	63
4.3b	Physical Normal Stress $\tilde{\sigma}_{nn}$ Distribution Along the Ellipse Border for $\xi_0 = 1.7$	64
4.3c	Physical Normal Stress $\tilde{\sigma}_{\xi\xi}$ Distribution Along the Line of Symmetry for $\xi_0 = 1.7$	65
4.3d	Apparent Stress Intensity Factor Distribution Along the Line of Symmetry for $\xi_0 = 1.7$	66
4.3e	Physical Maximum In-Plane Shear Stress Distribution for $\xi_0 = 1.7$	67
4.3f	Contravariant Displacement w^ξ Distribution Along the Line of Symmetry for $\xi_0 = 1.7$	68
4.4a	Physical Normal Stress $\tilde{\sigma}_{nn}$ Distribution Along the Line of Symmetry for $\xi_0 = 2.5$	69
4.4b	Physical Normal Stress $\tilde{\sigma}_{nn}$ Distribution Along the Ellipse Border for $\xi_0 = 2.5$	70
4.4c	Physical Normal Stress $\tilde{\sigma}_{\xi\xi}$ Distribution Along the Line of Symmetry for $\xi_0 = 2.5$	71
4.4d	Apparent Stress Intensity Factor Distribution Along the Line of Symmetry for $\xi_0 = 2.5$	72
4.4e	Physical Maximum In-Plane Shear Stress Distribution for $\xi_0 = 2.5$	73
4.4f	Contravariant Displacement w^ξ Distribution Along the Line of Symmetry for $\xi_0 = 2.5$	74

<u>Figure</u>		<u>Page</u>
4.5	Physical Normal Stress $\tilde{\sigma}_{nn}$ Distribution Along the Line of Symmetry for Various Ellipse Root Radii	75
4.6	Physical Normal Strain $\tilde{\epsilon}_{nn}$ Distribution Along the Line of Symmetry for Various Ellipse Root Radii	76
4.7	Variation of Initial Root Radius with Respect to Final Ellipse Root Radius	77
4.8	Variation of Physical Normal Stress $\tilde{\sigma}_{nn}$ Maximum with Respect to Initial Root Radius	78
4.9	Variation of Location of Physical Normal Stress $\tilde{\sigma}_{nn}$ Maximum with Respect to Initial Root Radius . .	79

I. INTRODUCTION AND REVIEW OF THE LITERATURE

Although the use of photoelasticity in obtaining stress intensity factors was noted by Irwin [1] in the early 1950's, broad implementation of the method was slow to develop. The reason for this is believed due to the problems involved in extracting accurately the stress intensity factor (SIF) from photoelastic data. Several different approaches have been cited for achieving this purpose for two dimensional geometries: one developed by Marloff and his associates [2] in 1970; one recommended by Irwin (above) and applied by Smith and Smith [3-5]; and those developed by Kobayashi and his associates [6-9].

An attempt to quantify the errors involved in the determination of the SIF in two dimensions through photoelasticity has been presented by Schroedl, McGowan and Smith [10]. In this study strong emphasis was put on taking photoelastic data in a region where Irwin's two degree of freedom system would apply (referred to as a 'singular' zone). Outside of this zone effects of free surfaces other than the crack surface may dominate. A Taylor Series expansion approach (TSCM) was developed in [10] to account for these 'outer' effects. Inside of this 'singular' zone crack tip blunting, finite rotations and finite strains dominate the desired crack behavior. In [10] the crack tip blunting is treated superficially and the last two effects are not included. Near the tip of the deformed crack these effects are very significant and cannot be neglected.

In many materials tensorial nonlinearities, as discussed by Ronay and Freudenthal [11] and Poynting [12], play a large role when strains are high. However, the materials used in stress-freezing photoelasticity (Hysol's CP-4290 and Photolastic's PLM-4B and PSM-8, for example) do not exhibit any stress-strain nonlinearities, even at high stress levels, as reported by Fessler and Mansell [13] for Araldite. These tensorial effects are, therefore, neglected.

Determination of values of the SIF in three dimensional problems is discussed by Smith [14]. Although Kassir and Sih [15] have shown that locally along an embedded elliptical flaw a two dimensional representation is still possible, the 'valid data' zone may become so constricted that the 'inner' and 'outer' effects must be dealt with. Smith et al [16-19] have developed the TSCM approach for various geometries, effectively handling the 'outer' problem. It therefore becomes increasingly important to find a method for accounting for not only blunting but also finite rotations and finite strains in the tip region, the fracture aspects of which are described in [20].

Several approaches have been used for dealing with the non-linear effects in the 'inner' zone. Perhaps the best known of these is exemplified in the solutions of Rice and Rosengren [21] and Hutchinson [22]. These solutions imposed small strain restrictions on an elasto-plastic solution using a deformation type plasticity theory with power law constitutive relations. From the form of the linear solution a class of functions was selected to represent the stresses and strains near

the crack tip in an asymptotic sense. The solution was reduced to an eigenvalue problem which was solved numerically and the subsequent singularity was evaluated through use of the J integral. Ref [21] was carried out for plane strain and Ref [22] to plane stress.

A second approach due to Knowles and Sternberg [23], [24] concerns the same crack and loading geometry as above; however, this latter plane strain treatment includes the effects of finite geometry change and finite strains. A non-linear constitutive law is postulated for large deformations using a four parameter representation of the strain energy density in terms of the strain invariants. Again the asymptotic form of the displacements is deduced from the linear problem and the investigation reduced to an eigenvalue problem. The solution contains two arbitrary constants, one of which is obtained through a conservation law. This approach was then extended to clarify and improve the lowest order asymptotic solution.

Prior to either of the above approaches O. L. Bowie [25] studied the effect of the small geometry change assumption on the near field of an elliptical hole using classical theory. He found stresses of the order of Young's Modulus and strains of order unity at the notch tip. More recently, Mansfield [26] employed a procedure involving an incrementalized classical theory of plane strain in order to estimate stresses near the tip of a deformed crack which he took to be elliptical in shape. His stress increments were computed from the deformed geometry and also indicated that stresses at the crack tip were at the order of Young's Modulus. Although neither of these two studies utilize large strain

definitions, they do concern the very near field behavior as will the model described in the sequel.

The present study will focus on the behavior of small crack-like ellipses (the size of these ellipses will be the same as a deformed crack) in an infinite plate in biaxial tension. This investigation seeks to give a complete treatment of the results of crack-tip blunting, finite rotations and finite strains while still using linearly elastic constitutive relations. The problem will be studied in the deformed geometry to simplify the boundary conditions and overall approach.

In the first step of the investigation a generalized 'Airy-type' stress function is introduced through the linear constitutive equations to arrive at the governing equation. Next a perturbation analysis is performed to characterize the form of the equations in the 'inner' nonlinear region, and to determine the matching conditions of the nonlinear to the linear solution at some acceptably far distance from the ellipse tip. The nonlinear compatibility equation is then solved in the tip region through use of finite differences and collocation. Finally the complete strain-displacement relations are integrated to determine the initial geometry. The stress and strain distributions of an initial crack will then be ascertained as a limit to the small ellipses analyzed.

II. FORMULATION OF THE PROBLEM

The characterization of small crack-like ellipses in an infinite plate under biaxial tension, including the effects of blunting, finite rotations and finite displacements will now be presented. First the governing equation applicable to the problem will be derived and the tensorial notation will be introduced. Finally the perturbation considerations will be discussed, separating the inner from the outer regions (i.e., nonlinear from linear); and the resulting solution procedure will be outlined, setting the stage for the actual solution method.

A. Notation and Formulae

The generalized curvilinear orthogonal coordinate system used in this study is shown in Figure 2.1, and the compatibility equation as given by Sokolnikoff [27] is

$$\epsilon_{ijk1} + \bar{h}^{\alpha\beta} (\epsilon_{jk\beta} \epsilon_{il\alpha} - \epsilon_{jl\beta} \epsilon_{ik\alpha}) = 0 , \quad (2.1)$$

where

$$\epsilon_{ijk1} = \bar{\epsilon}_{j1,ik} + \bar{\epsilon}_{ik,j1} - \bar{\epsilon}_{jk,il} - \bar{\epsilon}_{il,jk}$$

$$\epsilon_{ijk} = \bar{\epsilon}_{ik,j} + \bar{\epsilon}_{kj,i} - \bar{\epsilon}_{ij,k}$$

and $\bar{h}^{\alpha\beta}$ is the contravariant metric tensor of the undeformed geometry.

Note that throughout this treatment the comma represents the covariant derivative with respect to the deformed coordinates.

The undeformed covariant metric tensor, $\bar{h}_{\alpha\beta}$, as given by [27] may be written

$$\bar{h}_{ij} = \bar{g}_{ij} - 2\bar{\epsilon}_{ij}, \quad (2.2a)$$

or

$$\bar{h}_{ij} = \begin{Bmatrix} (\bar{g}_{11} - 2\bar{\epsilon}_{11}) & -2\bar{\epsilon}_{12} \\ -2\bar{\epsilon}_{12} & (\bar{g}_{22} - 2\bar{\epsilon}_{22}) \end{Bmatrix}, \quad (2.2b)$$

so therefore

$$\bar{h}^{ij} = \frac{1}{|\bar{h}|} \begin{Bmatrix} (\bar{g}_{22} - 2\bar{\epsilon}_{22}) & 2\bar{\epsilon}_{12} \\ 2\bar{\epsilon}_{12} & (\bar{g}_{11} - 2\bar{\epsilon}_{11}) \end{Bmatrix}, \quad (2.2c)$$

with

$$|\bar{h}| = \bar{g}_{22}\bar{g}_{11} - 2\bar{g}_{11}\bar{\epsilon}_{22} - 2\bar{g}_{22}\bar{\epsilon}_{11} + 4\bar{\epsilon}_{22}\bar{\epsilon}_{12} - 4\bar{\epsilon}_{12}^2.$$

The linear constitutive relation can be written as:

$$\bar{\epsilon}_{jk} = \frac{(1+\nu)}{E} \bar{\sigma}_{jk} - \frac{\nu\bar{\theta}}{E} \bar{g}_{jk}, \quad (2.3)$$

$$\text{where } \bar{\theta} = \bar{\sigma}_i^i = \bar{g}^{ij} \bar{\sigma}_{ij} \quad i,j = 1,2,3.$$

For plane strain $\bar{\epsilon}_{ij} = 0$ if i or $j = 3$ so that (2.3) becomes

$$\bar{\epsilon}_{jk} = \frac{(1+\nu)}{E} \bar{\sigma}_{jk} - \frac{\nu(1+\nu)}{E} \bar{\theta} \bar{g}_{jk}, \quad (2.4)$$

$$\text{where } \bar{\theta} = \bar{\sigma}_i^i = \bar{g}^{ij} \bar{\sigma}_{ij} \quad i,j = 1,2.$$

The only non-zero, unique compatibility equation is for $ijkl = 2121$. Noting this and then introducing (2.2c) and (2.4) into (2.1) and collecting terms results in:

$$\begin{aligned} & \frac{(1+v)}{E} (\bar{\sigma}_{11,22} + \bar{\sigma}_{22,11} - 2\bar{\sigma}_{12,12}) - v \frac{(1+v)}{E} (\bar{\sigma}_{11,22} \\ & + \bar{\sigma}_{22,11} + \frac{\bar{g}_{11}}{\bar{g}_{22}} \bar{\sigma}_{22,22} + \frac{\bar{g}_{22}}{\bar{g}_{11}} \bar{\sigma}_{11,11}) + \bar{h}^{11} F_{11} + \bar{h}^{12} F_{12} \\ & + \bar{h}^{22} F_{22} = 0 , \end{aligned} \quad (2.5)$$

with

$$\begin{aligned} F_{11} &= \left(\frac{1+v}{E} \right)^2 [\{ (1+v) \bar{\sigma}_{11,2} - v \frac{\bar{g}_{11}}{\bar{g}_{22}} \bar{\sigma}_{22,2} \}^2 \\ &+ \{ (1-v) \bar{\sigma}_{11,1} - v \frac{\bar{g}_{11}}{\bar{g}_{22}} \bar{\sigma}_{22,1} \} \{ (1-v) \bar{\sigma}_{22,1} \\ &- v \frac{\bar{g}_{22}}{\bar{g}_{11}} \bar{\sigma}_{11,1} - 2\bar{\sigma}_{12,2} \}] , \\ F_{22} &= \left(\frac{1+v}{E} \right)^2 [\{ (1+v) \bar{\sigma}_{22,1} - v \frac{\bar{g}_{22}}{\bar{g}_{11}} \bar{\sigma}_{11,1} \}^2 \\ &+ \{ (1-v) \bar{\sigma}_{11,1} - v \frac{\bar{g}_{11}}{\bar{g}_{22}} \bar{\sigma}_{22,1} \} \{ (1-v) \bar{\sigma}_{22,1} \\ &- v \frac{\bar{g}_{22}}{\bar{g}_{11}} \bar{\sigma}_{11,1} - 2\bar{\sigma}_{12,2} \}] , \end{aligned}$$

$$\begin{aligned}
 F_{12} = & \frac{(1+v)}{E}^2 [2\{(1-v)\bar{\sigma}_{22,1} - v\frac{\bar{g}_{22}}{\bar{g}_{11}}\bar{\sigma}_{11,1}\}\{(1-v)\bar{\sigma}_{11,2} \\
 & - v\frac{\bar{g}_{11}}{\bar{g}_{22}}\bar{\sigma}_{22,2}\} - \{(1-v)\bar{\sigma}_{22,1} - v\frac{\bar{g}_{22}}{\bar{g}_{11}}\bar{\sigma}_{11,1} \\
 & - 2\bar{\sigma}_{12,2}\}\{(1-v)\bar{\sigma}_{11,2} - v\frac{\bar{g}_{11}}{\bar{g}_{22}}\bar{\sigma}_{22,2} - 2\bar{\sigma}_{12,1}\} \\
 & - \{(1-v)\bar{\sigma}_{11,1} - v\frac{\bar{g}_{11}}{\bar{g}_{22}}\bar{\sigma}_{22,1}\}\{(1-v)\bar{\sigma}_{22,2} \\
 & - v\frac{\bar{g}_{22}}{\bar{g}_{11}}\bar{\sigma}_{11,2}\}] ,
 \end{aligned}$$

also

$$\begin{aligned}
 \bar{h}^{22} = & \frac{1}{|\bar{h}|} \{\bar{g}_{11} - 2 \frac{(1+v)}{E} [(1-v)\bar{\sigma}_{11} - v\frac{\bar{g}_{11}}{\bar{g}_{22}}\bar{\sigma}_{22}]\} , \\
 \bar{h}^{11} = & \frac{1}{|\bar{h}|} \{\bar{g}_{22} - 2 \frac{(1+v)}{E} [(1-v)\bar{\sigma}_{22} - v\frac{\bar{g}_{22}}{\bar{g}_{11}}\bar{\sigma}_{11}]\} , \\
 \bar{h}^{12} = & \frac{1}{|\bar{h}|} \{2 \frac{(1+v)}{E} \bar{\sigma}_{12}\} , \\
 |\bar{h}| = & \bar{g}_{11} \bar{g}_{22} - 2 \frac{(1+v)}{E} (1-2v) (\bar{\sigma}_{11} \bar{g}_{22} + \bar{\sigma}_{22} \bar{g}_{11}) \\
 & + 4 \left(\frac{1+v}{E} \right)^2 [\bar{\sigma}_{11} \bar{\sigma}_{22} - v(1-v) \bar{g}_{11} \bar{g}_{22} \left(\frac{\bar{\sigma}_{22}}{\bar{g}_{22}} + \frac{\bar{\sigma}_{11}}{\bar{g}_{11}} \right)^2 \\
 & - \bar{\sigma}_{12}^2] .
 \end{aligned}$$

Introducing now a generalized 'Airy' stress-function as suggested by Adkins, Green and Shield [28]:

$$\bar{\sigma}_{st} = \bar{g}_{s\alpha} \bar{g}_{t\beta} e^{\alpha i} e^{\beta j} \bar{\phi},_{ij} \quad (2.6)$$

where

$$e^{ij} = \begin{cases} \frac{1}{\sqrt{|g|}} & \text{if } i = 1, j = 2 \\ \frac{-1}{\sqrt{|g|}} & \text{if } i = 2, j = 1 \\ 0 & \text{if } i = j \end{cases}$$

Non-dimensionalizing the following variables:

$$\bar{g}_{11} = \bar{c}^2 g_{11}, \quad \bar{g}_{22} = \bar{c}^2 g_{22}, \quad \bar{\epsilon}_{ij} = \epsilon_{ij}$$

$$\bar{\sigma}_{ij} = \bar{p} \sigma_{ij}, \quad \bar{\phi} = \bar{p} c^{-2} \phi, \quad \bar{w} = \bar{c} w,$$

where \bar{c} is some characteristic length and \bar{p} is some characteristic stress, and also defining a physical derivative:

$$\tilde{A},_i = \frac{A,i}{\sqrt{g_{ii}}} \quad \text{where } \underline{i} \text{ is not summed,}$$

and then finally introducing these substitutions plus (2.6) into (2.5) leads to the expression:

$$\begin{aligned} 0 = & \{1 + 2\varepsilon A_1 (\tilde{\phi},_{22} + \tilde{\phi},_{11}) + 4\varepsilon^2 [\tilde{\phi},_{11} \tilde{\phi},_{22} - \tilde{\phi},_{12}]^2 \\ & + A_2 (\tilde{\phi},_{22} + \tilde{\phi},_{11})^2]\} B_0 \{\tilde{\phi},_{1111} + 2\tilde{\phi},_{1122} + \tilde{\phi},_{2222}\} \\ & + \varepsilon \{1 + 2\varepsilon (A_3 \tilde{\phi},_{11} + A_4 \tilde{\phi},_{22})\} \{B_1 \tilde{\phi},_{111}^2 + B_2 \tilde{\phi},_{122}^2\} \end{aligned}$$

$$\begin{aligned}
& + B_3 \tilde{\phi}_{,111} \tilde{\phi}_{,122} + B_4 \tilde{\phi}_{,222}^2 + B_5 \tilde{\phi}_{,112}^2 + B_6 \tilde{\phi}_{,112} \tilde{\phi}_{,222} \} \\
& + \epsilon \{ 1 + 2\epsilon (A_3 \tilde{\phi}_{,22} + A_4 \tilde{\phi}_{,11}) \} \{ B_1 \tilde{\phi}_{,222}^2 + B_2 \tilde{\phi}_{,112}^2 \\
& + B_3 \tilde{\phi}_{,112} \tilde{\phi}_{,222} + B_4 \tilde{\phi}_{,111}^2 + B_5 \tilde{\phi}_{,122}^2 + B_6 \tilde{\phi}_{,111} \tilde{\phi}_{,122} \} \\
& + \epsilon^2 2 \tilde{\phi}_{,12} \{ C_1 \tilde{\phi}_{,122} \tilde{\phi}_{,112} + C_2 \tilde{\phi}_{,111} \tilde{\phi}_{,222} \\
& + C_3 (\tilde{\phi}_{,122} \tilde{\phi}_{,222} + \tilde{\phi}_{,111} \tilde{\phi}_{,112}) \} \tag{2.7}
\end{aligned}$$

where $\epsilon = \frac{\bar{P}}{E} (1 + v)$, $A_1 = -(1 - 2v)$, $A_2 = v(1 - v)$

$$\begin{aligned}
A_3 &= -(1 - v), A_4 = v, B_0 = (1 - v), B_1 = -v(1 - v) \\
B_2 &= (1 - v)(2 - v), B_3 = 1 - 4v + 2v^2, B_4 = (1 - v)^2, B_5 = v^2 \\
B_6 &= -2v(1 - v), C_1 = 5 - 6v, C_2 = -(1 - 2v), C_3 = 2(1 - v) .
\end{aligned}$$

The strain-displacement relations as shown by [27] are

$$2\epsilon_{ij} = w_{i,j} + w_{j,i} - g^{ik} w_{1,i} w_{k,j} , \tag{2.8}$$

$$\text{with } \vec{\zeta} = \vec{r} - \vec{r}_0 , \quad \vec{\zeta} = w^i \vec{b}_i , \quad w^i = g^{ij} w_j$$

where \vec{b}_i are the base vectors in the deformed system, and \vec{r} and \vec{r}_0 are the position vectors in the deformed and undeformed systems, respectively.

The boundary conditions as applied to the stress-function, $\tilde{\phi}$, on a free surface (e.g., along the crack surface) are given by [28]:

$$\tilde{\phi}_{,1} = 0 , \quad \tilde{\phi}_{,2} = 0 . \tag{2.9}$$

Thus the entire system of equations has been specified for an arbitrary stress-type problem in terms of orthogonal curvilinear

coordinates with all derivatives taken in the deformed geometry.

B. Perturbation Analysis

The problem to be considered is shown in Figure 2.2, and consists of a small ellipse in an infinite plate with all-around uniform tension. At some distance from the ellipse tip the stresses are reduced to $0(\bar{\sigma})$, the strains to $0(\bar{\sigma}/E)$, and the displacements to $0(\bar{c}\bar{\sigma}/E)$, where $\bar{\sigma}$ is the remote tension and \bar{c} is one-half the crack length. Therefore, the governing equation (2.7) and the strain-displacement relations (2.8) both reduce to the linear forms. Thus, the solution of Inglis [29] applies

$$\sigma_{\xi\xi} = \sinh 2\xi \frac{(\cosh 2\xi - \cosh 2\xi_0)}{(\cosh 2\xi - \cos 2\eta)}, \quad (2.10a)$$

$$\sigma_{\eta\eta} = \sinh 2\xi \frac{(\cosh 2\xi + \cosh 2\xi_0 - 2 \cos 2\eta)}{(\cosh 2\xi - \cos 2\eta)}, \quad (2.10b)$$

$$\sigma_{\xi\eta} = \sinh 2\eta \frac{(\cosh 2\xi - \cosh 2\xi_0)}{(\cosh 2\xi - \cos 2\eta)}, \quad (2.10c)$$

$$w_\xi = \varepsilon \frac{(1 - 2\nu) \cosh 2\xi - 2(1 - \nu) \cos 2\eta + \cosh 2\xi_0}{(\cosh 2\xi - \cos 2\eta)}, \quad (2.10d)$$

$$w_\eta = 0, \quad (2.10e)$$

where ξ and η are the elliptical coordinates defined by $x = (\cosh \xi \cos \eta)$, $y = \sinh \xi \sin \eta$; $\varepsilon = \frac{\bar{\sigma}}{E}(1 + \nu)$, the characteristic length is \bar{c} , the characteristic stress is $\bar{\sigma}$, and ξ_0^2 is the non-dimensional root radius of the ellipse.

The root radius of a crack of length $2\bar{c}$ after deformation is predicted by (2.10d) with $\xi_0 = 0: w^{\frac{1}{2}} = \rho^{\frac{1}{2}} = 2\varepsilon(1 - \nu)$. The size of the ellipses to be investigated here will be of the same order, i.e. $\xi_0 = 0[2\varepsilon(1 - \nu)]$. The local geometry surrounding the tip will then be as shown in Figure 2.3 and the coordinates will locally be reduced to parabolic:

$$x = \frac{\xi^2 - n^2 - \xi_0^2}{2}, \quad y = \xi n, \quad g = g_{\xi\xi} = g_{nn} = \xi^2 + n^2.$$

The ordering scheme will also change in the neighborhood of the tip: the stresses are $O(\frac{1}{\varepsilon})$, the strains are $O(1)$, and the displacements are $O(1)$. Therefore, it is necessary to scale the variables so that they are all $O(1)$ in this region:

$$\begin{aligned} \hat{\sigma}_{ij} &= \sigma_{ij}\varepsilon, & \hat{\epsilon}_{ij} &= \epsilon_{ij}, & \phi &= \Phi\varepsilon^3, \\ w_i &= w_i, & \hat{g}_{\xi\xi} &= \hat{g}_{nn} = \frac{g_{\xi\xi}}{\varepsilon^2} \end{aligned} \quad (2.11)$$

Substituting (2.11) into (2.7) yields

$$\begin{aligned} 0 &= \{1 + 2A_1 (\phi_{,\xi\xi} + \phi_{,nn}) + 4[\phi_{,\xi\xi}\phi_{,nn} - \phi_{,\xi n}] \\ &\quad + A_2 (\phi_{,\xi\xi} + \phi_{,nn})^2\} B_0 \{\phi_{,\xi\xi\xi\xi} + 2\phi_{,\xi\xi nn} + \phi_{,nnnn} \\ &\quad + \{1 + 2(A_3\phi_{,\xi\xi} + A_4\phi_{,nn})\} \{B_1\phi_{,\xi\xi\xi}^2 + B_2\phi_{,\xi\xi nn}^2 \\ &\quad + B_3\phi_{,\xi\xi\xi}\phi_{,nnn} + B_4\phi_{,nnnn}^2 + B_5\phi_{,\xi\xi n}^2 + B_6\phi_{,\xi\xi n}\phi_{,nnn}\} \\ &\quad + \{1 + 2(A_3\phi_{,nn} + A_4\phi_{,\xi\xi})\} \{B_1\phi_{,nnn}^2 + B_2\phi_{,\xi\xi n}^2 \\ &\quad + B_3\phi_{,\xi\xi n}\phi_{,nnn} + B_4\phi_{,\xi\xi\xi}^2 + B_5\phi_{,\xi\xi nn}^2 + B_6\phi_{,\xi\xi\xi}\phi_{,nnn}\} \} \end{aligned}$$

$$\begin{aligned}
& + 2\phi_{,\xi\eta} \{ C_1 \phi_{,\xi\eta\eta} \phi_{,\xi\xi\eta} + C_2 \phi_{,\xi\xi\xi} \phi_{,\eta\eta\eta} \\
& + C_3 (\phi_{,\xi\eta\eta} \phi_{,\eta\eta\eta} + \phi_{,\xi\xi\xi} \phi_{,\xi\xi\eta}) \} , \tag{2.12}
\end{aligned}$$

(The \sim notation has been dropped for simplicity.)

and, the substitution of (2.11) into (2.8) leaves it virtually unchanged.

Since the displacements in the tip region are large, the boundary conditions (i.e., $\phi_{,1} = \phi_{,2} = 0$) must be applied to the deformed geometry. As an additional boundary condition the inner solution must be 'matched' to the outer solution where they intersect. As Van Dyke [30] expresses, the outer solution (i.e., linear solution in this case) should be written in terms of the inner variables and then the perturbation parameter, ϵ , should be made very small, the inner solution should then be matched to the result. The inner solution would then approach, as ξ and η get large, these expressions for stress, strain and displacement:

$$\hat{\sigma}_{\eta\eta} = \frac{\xi(\xi^2 + 2\eta^2 + \xi_0^2)}{(\xi^2 + \eta^2)} \tag{2.13a}$$

$$\hat{\sigma}_{\xi\eta} = \frac{\eta(\xi^2 - \xi_0^2)}{(\xi^2 + \eta^2)} \tag{2.13b}$$

$$\hat{\sigma}_{\xi\xi} = \frac{\xi(\xi^2 - \xi_0^2)}{(\xi^2 + \eta^2)} \tag{2.13c}$$

$$\hat{w}^\xi = \frac{(1 - 2\nu) \xi^2 + 2(1 - \nu) \eta^2 + \xi_0^2}{(\xi^2 + \eta^2)} \tag{2.13d}$$

$$\hat{w}_n = 0 . \quad (2.13e)$$

As the problem is a quasi-elliptic fourth-order partial differential equation, there must be two boundary conditions at each of the four edges, as shown in Figure 2.4. At the inner edge of the ellipse ($\xi = \xi_0$) the boundary conditions are as discussed above:

$\phi_{,\xi} = 0$ and $\phi_{,n} = 0$ or alternately $\phi_{,n} = 0$ and $\phi = \text{constant}$ (where $\phi_{,n}$ indicates the covariant derivative of ϕ in the direction normal to the ellipse surface). Since the problem is symmetric about the x -axis the boundary conditions along $n = 0$ reduces to $\frac{\partial \phi}{\partial n} = 0$ and $\frac{\partial^3 \phi}{\partial n^3} = 0$. Now the matching conditions along $n = n_{\max}$ and $\xi = \xi_{\max}$ must be reduced to quasi-boundary conditions. Stress boundary conditions at an interface between two materials require that the normal normal stress and the tangential shear stress be the same on both sides. Therefore, these conditions shall be adopted at the boundary between the inner and outer regions (referring to Figure 2.3):

$$\phi = \phi_{\text{linear}}, \quad \frac{\partial \phi}{\partial \xi} = \frac{\partial \phi}{\partial \xi_{\text{linear}}}, \quad \text{at } \xi = \xi_{\max}$$

$$\phi = \phi_{\text{linear}}, \quad \frac{\partial \phi}{\partial n} = \frac{\partial \phi}{\partial n_{\text{linear}}}, \quad \text{at } n = n_{\max}$$

However, for matching to be complete the inner tangential normal stress at the interface must also be equal to the outer tangential normal stress. To insure this, the values of ξ_{\max} and n_{\max} will be enlarged until the matching occurs.

Thus the solution procedure can be summarized as follows: first, a deformed geometry is chosen; then, the linear outer solution is

computed; next the non-linear solution is determined subject to the deformed geometry by finite differences and is matched to the outer solution at a sufficiently large distance from the crack tip; finally, the non-linear strain-displacement relations are integrated to determine the displacements.

III. SOLUTION TO THE PROBLEM

The governing equation for the stress function will now be solved for various ellipses with small root radii approaching that of a deformed crack in an infinite plate. In order for the nonlinear quasi-elliptic equation to be solved it will be first reduced to linear form by a Newtonian method; the coefficients of this linearized equation, however, will depend upon the stress function itself. Therefore, the equation must be solved repeatedly, updating these coefficients each time, until the solution changes within some acceptably small amount. Since the convergence of the equation is questionable and because of the lack of experimental evidence, two general solution methods and one limit analysis will be presented. The first method to be discussed is a finite-difference analysis; the second is an internal collocation analysis based upon a truncated infinite orthogonal series which satisfies the boundary conditions exactly; and finally, the limit analysis which is based upon the integration of the strain-displacement relations.

A. Linearization of the Governing Equation

The one equation for the stress function (2.12) may be represented as

$$0 = \Delta \nabla^4 \phi + \Delta_1 F_1 + \Delta_2 F_2 + \Delta_3 F_3 \quad (3.1)$$

$$\text{where } \Delta = 1 + 2A_1(\phi_{\xi\xi} + \phi_{\eta\eta}) + 4[\phi_{\xi\xi}\phi_{\eta\eta} - \phi_{\xi\eta}]^2$$

$$+ A_2(\phi_{\xi\xi} + \phi_{\eta\eta})^2]$$

$$\Delta_1 = 1 + 2(A_3\phi_{\xi\xi} + A_4\phi_{\eta\eta}) ; \quad \Delta_2 = 1 + 2(A_3\phi_{\eta\eta} + A_4\phi_{\xi\xi}) ;$$

$$\Delta_3 = 2\phi_{\xi\eta} ; \quad F_1 = \frac{B_1}{B_0} \phi_{\xi\xi\xi}^2 + \frac{B_2}{B_0} \phi_{\xi\eta\eta}^2 + \frac{B_3}{B_0} \phi_{\xi\xi\xi}\phi_{\xi\eta\eta} \\ + B_4/B_0 \phi_{\eta\eta\eta}^2 + B_5/B_0 \phi_{\xi\xi\eta} + B_6/B_0 \phi_{\xi\xi\eta}\phi_{\eta\eta\eta} ;$$

$$F_2 = B_1/B_0 \phi_{\eta\eta\eta}^2 + B_2/B_0 \phi_{\xi\xi\eta}^2 + B_3/B_0 \phi_{\xi\xi\eta}\phi_{\eta\eta\eta} \\ + B_4/B_0 \phi_{\xi\xi\xi}^2 + B_5/B_0 \phi_{\xi\eta\eta}^2 + B_6/B_0 \phi_{\xi\xi\xi}\phi_{\xi\eta\eta} ;$$

$$F_3 = C_1/B_0 \phi_{\xi\eta\eta}\phi_{\xi\xi\eta} + C_2/B_0 \phi_{\xi\xi\xi}\phi_{\eta\eta\eta} \\ + C_3/B_0 (\phi_{\xi\eta\eta}\phi_{\eta\eta\eta} + \phi_{\xi\xi\xi}\phi_{\xi\xi\eta}) .$$

Expanding Δ in a Taylor series about some initial value of $\phi_{\xi\xi}$, $\phi_{\xi\eta}$, and $\phi_{\eta\eta}$ yields

$$\Delta = \Delta_0 + \xi\xi\Delta_0(\phi_{\xi\xi} - \phi_{\xi\xi|0}) + \xi\eta\Delta_0(\phi_{\xi\eta} - \phi_{\xi\eta|0}) \\ + \eta\eta\Delta_0(\phi_{\eta\eta} - \phi_{\eta\eta|0}) + O(\delta^2)$$

where $_0$ represents the initial value

$$\text{and } \delta = (\phi_{\xi\xi} - \phi_{\xi\xi|0}) \text{ or } (\phi_{\xi\eta} - \phi_{\xi\eta|0}) \text{ or } (\phi_{\eta\eta} - \phi_{\eta\eta|0})$$

$$\text{with } \xi\xi\Delta = \frac{\partial\Delta}{\partial\phi_{\xi\xi}} = 2A_1 + 4(\phi_{\eta\eta} + 2A_2(\phi_{\xi\xi} + \phi_{\eta\eta}))$$

$$\xi\eta\Delta = \frac{\partial\Delta}{\partial\phi_{\xi\eta}} = -8\phi_{\xi\eta}$$

$$\eta\eta\Delta = \frac{\partial\Delta}{\partial\phi_{\eta\eta}} = 2A_1 + 4(\phi_{\xi\xi} + 2A_2(\phi_{\xi\xi} + \phi_{\eta\eta}))$$

In like manner linearizing F_1 , F_2 , and F_3 and substituting these into (3.1) yields

$$\begin{aligned} {}^0\beta \nabla^4 \phi + {}^1\beta_0 \phi, \xi\xi\xi + {}^2\beta_0 \phi, \xi\xi\eta + {}^3\beta_0 \phi, \xi\eta\eta + {}^4\beta_0 \phi, \eta\eta\eta \\ + {}^5\beta_0 \phi, \xi\xi + {}^6\beta_0 \phi, \xi\eta + {}^7\beta_0 \phi, \eta\eta = {}^8\beta \end{aligned} \quad (3.2)$$

where ${}^0\beta = \Delta$; ${}^1\beta = \xi\xi\xi F_1 \Delta_1 + \xi\xi\xi F_2 \Delta_2 + \xi\xi\xi F_3 \Delta_3$

$${}^2\beta = \xi\xi\eta F_1 \Delta_1 + \xi\xi\eta F_2 \Delta_2 + \xi\xi\eta F_3 \Delta_3; \quad {}^3\beta = \xi\eta\eta F_1 \Delta_1 + \xi\eta\eta F_2 \Delta_2$$

$$+ \xi\eta\eta F_3 \Delta_3; \quad {}^4\beta = \eta\eta\eta F_1 \Delta_1 + \eta\eta\eta F_2 \Delta_2 + \eta\eta\eta F_3 \Delta_3;$$

$${}^5\beta = \xi\xi_{\Delta_1} F_1 + \xi\xi_{\Delta_2} F_2 + \xi\xi_{\Delta} \nabla^4 \phi; \quad {}^6\beta = \xi\eta_{\Delta_3} F_3 + \xi\eta_{\Delta} \nabla^4 \phi;$$

$${}^7\beta = \eta\eta_{\Delta_1} F_1 + \eta\eta_{\Delta_2} F_2 + \eta\eta_{\Delta} \nabla^4 \phi; \quad {}^8\beta = -(\Delta_1 F_1 + \Delta_2 F_2 + \Delta_3 F_3)_0$$

$$+ {}^1\beta_0 \phi, \xi\xi\xi_0 + {}^2\beta_0 \phi, \xi\xi\eta_0 + {}^3\beta_0 \phi, \xi\eta\eta_0 + {}^4\beta_0 \phi, \eta\eta\eta_0$$

$$+ {}^5\beta_0 \phi, \xi\xi_0 + {}^6\beta_0 \phi, \xi\eta_0 + {}^7\beta_0 \phi, \eta\eta_0;$$

(A complete listing of the quantities ${}^{ijk}F_m$, etc., and the necessary physical covariant derivatives are listed in the Appendix.)

B. Finite-Difference Method

The governing equation, having now been reduced to a tractable linear form, can now be solved by finite differences. Near the boundary of the nonlinear region (the boundary comprising the inner stress-free border at ξ_0 or the linear-nonlinear interface) the finite difference scheme, written at point 2 as shown in Figure 3.1a, becomes

$$\begin{aligned}
 \left. \frac{d^4 \phi}{dx^4} \right|_2 &= \frac{(-113\phi_1 - 60\Delta x \frac{d\phi}{dx})_1 + 192\phi_2 - 108\phi_3 + 32\phi_4 - 3\phi_5) + O(\Delta x^2)}{12\Delta x^4} \\
 \left. \frac{d^3 \phi}{dx^3} \right|_2 &= \frac{(8\phi_1 + 6\Delta x \frac{d\phi}{dx})_1 - 9\phi_2 + \phi_4) + O(\Delta x^2)}{3\Delta x^3} \\
 \left. \frac{d^2 \phi}{dx^2} \right|_2 &= \frac{(\phi_3 - 2\phi_2 - \phi_1) + O(\Delta x^2)}{\Delta x^2} \\
 \left. \frac{d\phi}{dx} \right|_2 &= \frac{\phi_3 - \phi_1}{2\Delta x} + O(\Delta x^2)
 \end{aligned} \tag{3.3}$$

Note that because of the boundary conditions both ϕ_1 and $\frac{d\phi}{dx}|_1$ are known.

In the region removed from the boundary by at least two steps the finite-difference scheme written about point 3, as shown in Figure 3.1b, becomes

$$\begin{aligned}
 \left. \frac{d^4 \phi}{dx^4} \right|_3 &= \frac{(\phi_5 - 4\phi_4 + 6\phi_3 - 4\phi_2 + \phi_1) + O(\Delta x^2)}{\Delta x^4} \\
 \left. \frac{d^3 \phi}{dx^3} \right|_3 &= \frac{(\phi_5 - 2\phi_4 + 2\phi_2 - \phi_1) + O(\Delta x^2)}{2\Delta x^3} \\
 \left. \frac{d^2 \phi}{dx^2} \right|_3 &= \frac{(\phi_4 - 2\phi_3 - \phi_1) + O(\Delta x^2)}{\Delta x^2}
 \end{aligned} \tag{3.4}$$

$$\left. \frac{d\phi}{dx} \right|_3 = \frac{(\phi_4 - \phi_2)}{2\Delta x} + O(\Delta x^2)$$

Various two-dimensional combinations of the two above mentioned schemes are used depending upon the placement of the grid point (at which the governing equation is being solved) in relation to the boundaries. Two specific cases of those possible will be discussed here: first, the scheme used when no boundaries are near; and second, the scheme used when two boundaries are near. In the first case as shown in Figure 3.2a the equation will be solved at point 13 with the resulting expressions for the partial derivatives:

$$\left. \frac{\partial^4 \phi}{\partial x^4} \right|_{13} = \frac{(\phi_{15} - 4\phi_{14} + 6\phi_{13} - 4\phi_{12} + \phi_{11})}{\Delta x^4} + O(\delta^2)$$

$$\left. \frac{\partial^4 \phi}{\partial x^2 \partial y^2} \right|_{13} = \frac{(\phi_{19} - 2\phi_{18} + \phi_{17} - 2\phi_{14} + 4\phi_{13} - 2\phi_{12} + \phi_9 - 2\phi_8 + \phi_7)}{\Delta x^2 \Delta y^2} + O(\delta^2)$$

$$\left. \frac{\partial^4 \phi}{\partial y^4} \right|_{13} = \frac{(\phi_{23} - 4\phi_{18} + 6\phi_{13} - 4\phi_8 + \phi_3)}{\Delta y^4} + O(\delta^2)$$

$$\left. \frac{\partial^3 \phi}{\partial x^3} \right|_{13} = \frac{(\phi_{15} - 2\phi_{14} + 2\phi_{12} - \phi_{11})}{2\Delta x^3} + O(\delta^2)$$

$$\left. \frac{\partial^3 \phi}{\partial x^2 \partial y} \right|_{13} = \frac{(\phi_{19} - 2\phi_{18} + \phi_{17} - \phi_9 + 2\phi_8 - \phi_7)}{2\Delta x^2 \Delta y} + O(\delta^2)$$

$$\left. \frac{\partial^3 \phi}{\partial x \partial y^2} \right|_{13} = \frac{(\phi_{19} - \phi_{17} - 2\phi_{14} + 2\phi_{12} + \phi_9 - \phi_7)}{2\Delta x \Delta y^2} + O(\delta^2) \quad (3.5)$$

$$\left. \frac{\partial^3 \phi}{\partial y^3} \right|_{13} = \frac{(\phi_{23} - 2\phi_{18} + 2\phi_8 - \phi_3)}{2\Delta y^3} + O(\delta^2)$$

$$\left. \frac{\partial^2 \phi}{\partial x^2} \right|_{13} = \frac{(\phi_{14} - 2\phi_{13} + \phi_{12})}{\Delta x^2} + O(\delta^2)$$

$$\left. \frac{\partial^2 \phi}{\partial x \partial y} \right|_{13} = \frac{(\phi_{19} - \phi_{17} - \phi_9 + \phi_7)}{4\Delta x \Delta y} + O(\delta^2)$$

$$\left. \frac{\partial^2 \phi}{\partial y^2} \right|_{13} = \frac{(\phi_{18} - 2\phi_{13} + \phi_8)}{\Delta y^2} + O(\delta^2)$$

$$\left. \frac{\partial \phi}{\partial x} \right|_{13} = \frac{(\phi_{14} - \phi_{12})}{2\Delta x} + O(\delta^2)$$

$$\left. \frac{\partial \phi}{\partial y} \right|_{13} = \frac{(\phi_{18} - \phi_8)}{2\Delta y} + O(\delta^2) \quad \text{where } \delta \text{ is either } \Delta x \text{ or } \Delta y.$$

For the second case when two boundaries are present as shown in Figure 3.2b, the governing equation will be solved at point 9 with the following expressions for the partial derivatives resulting:

$$\left. \frac{\partial^4 \phi}{\partial x^4} \right|_9 = \frac{(-113\phi_{10} + 60\Delta x \frac{\partial \phi}{\partial x})_{10} + 192\phi_9 - 108\phi_8 + 32\phi_7 - 3\phi_6}{12\Delta x^4} + O(\delta^2)$$

$$\left. \frac{\partial^4 \phi}{\partial x^2 \partial y^2} \right|_9 = \frac{(\phi_{15} - 2\phi_{14} + \phi_{13} - 2\phi_{10} + 4\phi_9 - 2\phi_8 + \phi_5 - 2\phi_4 + \phi_3)}{\Delta x^2 \Delta y^2}$$

$$+ O(\delta^2)$$

$$\left. \frac{\partial^4 \phi}{\partial y^4} \right|_9 = \frac{(-3\phi_{24} + 32\phi_{19} - 108\phi_{14} + 192\phi_9 - 60\Delta y \frac{\partial \phi}{\partial y})_4 - 113\phi_4}{12\Delta y^4} + O(\delta^2)$$

$$\left. \frac{\partial^3 \phi}{\partial x^3} \right|_9 = \frac{(-8\phi_{10} + 6\Delta x \frac{\partial \phi}{\partial x})_{10} + 9\phi_9 - \phi_7}{3\Delta x^3} + O(\delta^2)$$

$$\left. \frac{\partial^3 \phi}{\partial x^2 \partial y} \right|_9 = \frac{(\phi_{15} - 2\phi_{14} + \phi_{13} - \phi_5 + 2\phi_4 - \phi_3)}{2\Delta x^2 \Delta y} + O(\delta^2)$$

(3.6)

$$\left. \frac{\partial^3 \phi}{\partial x \partial y^2} \right|_9 = \frac{(\phi_{15} - \phi_{13} - 2\phi_{10} + 2\phi_8 + \phi_5 - \phi_3)}{2\Delta x \Delta y^2} + O(\delta^2)$$

$$\left. \frac{\partial^3 \phi}{\partial y^3} \right|_9 = \frac{(\phi_{19} - 9\phi_9 + 6\Delta y \frac{\partial \phi}{\partial y})_4 + 8\phi_4}{3\Delta y^3} + O(\delta^2)$$

$$\left. \frac{\partial^2 \phi}{\partial x^2} \right|_9 = \frac{(\phi_{10} - 2\phi_9 + \phi_8)}{\Delta x^2} + O(\delta^2)$$

$$\left. \frac{\partial^2 \phi}{\partial x \partial y} \right|_9 = \frac{(\phi_{15} - \phi_{13} - \phi_5 + \phi_3)}{4\Delta x \Delta y} + O(\delta^2)$$

$$\left. \frac{\partial^2 \phi}{\partial y^2} \right|_9 = \frac{(\phi_{14} - 2\phi_9 + \phi_4)}{\Delta y^2} + O(\delta^2)$$

$$\left. \frac{\partial \phi}{\partial x} \right|_9 = \frac{(\phi_{10} - \phi_8)}{2\Delta x} + O(\delta^2)$$

$$\left. \frac{\partial \phi}{\partial y} \right|_9 = \frac{(\phi_{14} - \phi_4)}{2\Delta y} + O(\delta^2)$$

(Note that the values of ϕ_{25} , ϕ_{20} , ϕ_{15} , ϕ_{10} , ϕ_5 , ϕ_4 , ϕ_3 , ϕ_2 , ϕ_1 , $\left. \frac{\partial \phi}{\partial x} \right|_{10}$ and $\left. \frac{\partial \phi}{\partial y} \right|_4$ are all known and treated as boundary conditions.)

Using equations (3.5) or (3.6) or an analogue of them, all of the partial derivatives necessary in the evaluation of the needed physical covariant derivatives in the governing equation (3.2) can be obtained. The region of interest should be divided up evenly in the parabolic coordinates ξ and η to give the necessary grid pattern as shown in Figure 3.3. Then at each grid point interior to the boundary a linear equation involving a bandwidth of $3N + 1$ (where N is the number of grid points in the η direction) is generated. This resulting linear system of equations may be solved simultaneously by any direct method, e.g. Gaussian elimination:

$$[A]\phi = B \quad (3.7)$$

where $[A]$ is a banded coefficient matrix depending upon the distribution; ϕ is the independent variable evaluated at each grid point; B is a vector of constants composed of β_β in equation (3.2) and the boundary conditions. Since the coefficient matrix and the right-hand-

side vector both depend upon the ϕ distribution, the solution must be iterated until the change is acceptably small.

C. Internal Collocation Method

The second method pursued involves selecting a series of orthogonal polynomials which satisfy the boundary conditions exactly. One such representation is the familiar double Fourier series:

$$\begin{aligned} \phi = \phi_{\text{linear}} + \sum_{m=1}^M \sum_{n=1}^N c_{mn} & \left\{ 1 - \cos \left(\frac{2m\pi(\xi - \xi_0)}{(\xi_{\max} - \xi_0)} \right) \right\} \left\{ 1 \right. \\ & \left. + \cos \left(\frac{(2n - 1)\pi n}{n_{\max}} \right) \right\} \end{aligned} \quad (3.8)$$

Note that this double series satisfies the symmetry condition at $n = 0$, the boundary conditions at $\xi = \xi_0$, the matching conditions at $\xi = \xi_{\max}$, and the matching conditions at $n = n_{\max}$. There are $M \times N$ unknown constants in this double series; these may be determined by solving the governing equation (3.2) at $M \times N$ discrete points in the region of interest by iteration. Figure 3.3 shows how the region is to be divided up evenly (equal divisions are not necessary; however, convergence of the method were helped by this). The resulting system of linear equations may be solved by direct methods:

$$[A]C_{mn} = B \quad (3.9)$$

where A is a full $M \times N$ by $M \times N$ coefficient matrix depending upon the C_{mn} distribution; C_{mn} are the coefficients in equation (3.8); and B is the

vector of constants depending on C_{mn} in the previous iteration.

The advantage of this method lies in its simplicity of formulation and in its satisfaction of the boundary conditions exactly. However, due to the ripples inherent in any Fourier representation, the method became unstable for large values of M and N. Also, since the coefficient matrix [A] in equation (3.9) is completely full, the solution time and core size became large for even moderate numbers of terms. The finite-difference formulation is complex because of the many types of grids possible; however, the method is stable and the coefficient matrix [A] in equation (3.7) is sparse and can be solved by banded Gaussian methods with a considerable savings in computing time on a digital computer.

D. Integration of the Strain-Displacement Relations and Limit Analysis

Whichever method is used to determine the stress function and subsequently the covariant strains ϵ_{ij} , these strains will be integrated through the complete strain-displacement equations (2.8) to determine the displacements. Writing equation (2.8) in terms of the parabolic coordinates yields

$$2\epsilon_{\xi\xi} = 2w_{\xi,\xi} - w_{\xi,\xi}^2/g - w_{n,\xi}^2/g \quad (3.9a)$$

$$2\epsilon_{\xi n} = w_{\xi,n} + w_{n,\xi} - w_{\xi,\xi} w_{\xi,n}/g - w_{n,n} w_{n,\xi}/g \quad (3.9b)$$

$$2\epsilon_{nn} = 2w_{n,n} - 2w_{n,n}^2/g - w_{\xi,n}^2/g \quad (3.9c)$$

(The $\hat{}$ notation has been dropped for simplicity.)

These equations (3.9) will be finite-differenced to yield a system of first order nonlinear differential equations which must be solved simultaneously through iteration. The finite difference scheme to be used here is shown in Figure 3.4 and the resulting partial derivatives solved at point 3 are

$$\left. \frac{\partial u}{\partial x} \right|_3 = \frac{(u_1 - 4u_2 + 3u_3)}{2\Delta x} + O(\Delta x^2)$$

$$\left. \frac{\partial u}{\partial y} \right|_3 = \frac{(-u_5 + 4u_4 - 3u_3)}{2\Delta y} + O(\Delta y^2).$$

Since there are only two unknowns (w_{ξ} and w_{η}) to be determined, only two of the three equations (3.9) are necessary in the procedure. Equations (3.9a) and (3.9c) are chosen because of their superior stability in the iterative calculations. Solving (3.9a) for $w_{\xi,\xi}$ and (3.9c) for $w_{\eta,\eta}$ yields

$$w_{\xi,\xi} = g (1 \pm \sqrt{1 - w_{\eta,\xi}^2/g^2 - 2\varepsilon_{\xi\xi}/g})$$

$$w_{\eta,\eta} = g (1 \pm \sqrt{1 - w_{\xi,\eta}^2/g^2 - 2\varepsilon_{\eta\eta}/g}).$$

The lower sign will be chosen because the expression would then reduce to the linear result for small strains and displacements; hence, the above result would become

$$w_{\xi,\xi}/g = (1 - \sqrt{1 - w_{\eta,\xi}^2/g^2 - 2\varepsilon_{\xi\xi}/g})$$

$$w_{\eta,\eta}/g = (1 - \sqrt{1 - w_{\xi,\eta}^2/g^2 - 2\varepsilon_{\eta\eta}/g}).$$

Introduction of a \tilde{w} to represent a physical quantity gives the following expressions:

$$\tilde{w}_{\xi,\xi} = (1 - \sqrt{1 - \tilde{w}_{\eta,\xi}^2 - 2\varepsilon_{\xi\xi}}) \quad (3.11a)$$

$$\tilde{w}_{\eta,\eta} = (1 - \sqrt{1 - \tilde{w}_{\xi,\eta}^2 - 2\varepsilon_{\eta\eta}}) \quad (3.11b)$$

(The necessary physical covariant derivatives of w_ξ and w_η are found in the Appendix.)

After substituting the finite difference equations (3.10) into the linearized expressions for $\tilde{w}_{\xi,\xi}$ and $\tilde{w}_{\eta,\eta}$ in equations (3.11), the actual numerical procedure to find the displacements would then begin.

Referring to Figure 3.3, the integration procedure would begin one step from ξ_{\max} ($\xi = \xi_{\max} - \Delta\xi$) and at $\eta = 0$. Since at this grid point $w_\eta = 0$ equals zero and $w_{\xi,\eta} = 0$ equals zero from symmetry conditions, equation (3.11a) becomes uncoupled and can be solved for w_ξ directly without iteration. Next the procedure steps in the positive η -direction solving equations (3.11a) and (3.11b) simultaneously for w_ξ and w_η through iteration at each grid point until η_{\max} is reached. Then another step is taken toward ξ_0 ($\xi_{\text{new}} = \xi_{\text{old}} - \Delta\xi$) and the procedure is repeated. This stepping in both the negative ξ and the positive η -directions is carried out until w_ξ and w_η have been determined in the entire region.

The limit analysis consists of examining the existence of $\tilde{w}_{\eta,\eta}$ in equation (3.11b) at the ellipse tip along the line of symmetry.

The discriminant of this equation is $1 - \tilde{w}_{\xi,\eta}^2 - 2\tilde{\epsilon}_{nn}$. Noting that $\tilde{w}_{\xi,\eta}$ is equal to zero along the line of symmetry reduces the expression to $1 - 2\tilde{\epsilon}_{nn}$. From equation (2.4) $\tilde{\epsilon}_{nn}$ can be written in terms of the stresses:

$$\tilde{\epsilon}_{nn} = (1 - v) \tilde{\sigma}_{nn} - v \tilde{\sigma}_{\xi\xi}$$

Along the ellipse $\tilde{\sigma}_{\xi\xi}$ equals zero, so that $\tilde{\epsilon}_{nn} = (1 - v) \tilde{\sigma}_{nn}$.

Inserting this result into the expression for the discriminant above yields

$$\text{discriminant} = 1 - 2(1 - v) \tilde{\sigma}_{nn}.$$

For $\tilde{w}_{\xi,\eta}$ to be real in equation (3.11b) the discriminant must be greater than or equal to zero:

$$0 \leq 1 - 2(1 - v) \tilde{\sigma}_{nn} \quad \text{at } \xi = \xi_0, n = 0;$$

or alternately (3.12)

$$\tilde{\sigma}_{nn} \leq \frac{1}{2(1 - v)} \quad \text{at } \xi = \xi_0, n = 0.$$

To understand the result expressed in equation (3.12) more fully it is necessary to study the unstrained metric tensor h_{ij} from equation (2.2b):

$$h_{ij} = g \begin{Bmatrix} (1 - 2\tilde{\epsilon}_{\xi\xi}) & -2\tilde{\epsilon}_{\xi\eta} \\ -2\tilde{\epsilon}_{\xi\eta} & (1 - 2\tilde{\epsilon}_{nn}) \end{Bmatrix}.$$

The determinant of this matrix may be written

$$|h| = g^2 \{(1 - 2\tilde{\varepsilon}_{\xi\xi}) (1 - 2\tilde{\varepsilon}_{nn}) - 4\tilde{\varepsilon}_{\xi\eta}^2\};$$

along the line of symmetry this expression may be simplified to

$$|h| = g^2 \{(1 - 2\tilde{\varepsilon}_{\xi\xi}) (1 - 2\tilde{\varepsilon}_{nn})\} \quad (3.13)$$

If the determinant $|h|$ is zero, this situation is equivalent to a mapping which takes a region in the deformed geometry and transforms it into a point in the initial geometry, i.e. an ellipse maps into a crack (a degenerate ellipse). At the ellipse tip $\tilde{\sigma}_{\xi\xi}$ becomes zero so that equation (2.4) would give the strains:

$$\tilde{\varepsilon}_{nn} = (1 - v)\tilde{\sigma}_{nn}, \quad \tilde{\varepsilon}_{\xi\xi} = -v\tilde{\sigma}_{nn};$$

substituting this result into (3.13) and equating this result to zero gives

$$0 = (1 + v\tilde{\sigma}_{nn}) (1 - 2(1 - v)\tilde{\sigma}_{nn}).$$

Because the plate is under uniform tension it is unlikely that $\tilde{\sigma}_{nn}$ would ever be negative, the above equation becomes

$$0 = (1 - 2(1 - v)\tilde{\sigma}_{nn}) \text{ or } \tilde{\sigma}_{nn} = \frac{1}{2(1 - v)}. \quad (3.14)$$

Comparing the results of (3.14) and (3.12) it is evident that a value of $\tilde{\sigma}_{nn}$ higher than $\frac{1}{2(1 - v)}$ is impossible because the ellipse would map past a crack. Therefore the maximum stress possible at the tip of an ellipse is $\tilde{\sigma}_{max} = \frac{1}{2(1 - v)}$, which only occurs if the initial geometry is a crack of zero root radius.

IV. DISCUSSION OF THE RESULTS AND CONCLUSIONS

The physical stresses and strains in the field surrounding the tip will now be presented for small ellipses with Poisson's ratio equal to one-half; the contravariant displacements in the tip region will also be discussed. Finally, the results for these small ellipses will be extrapolated to determine the stress field around the deformed tip of a crack of zero initial root radius.

Throughout the following discussion reference will be made to the terms 'physical' and 'dimensional'. A 'physical dimensional' stress will be a stress as measured experimentally and will be denoted $\tilde{\sigma}_{ij}^*$. A 'physical nondimensional' stress can be found: $\tilde{\sigma}_{ij}^* = \tilde{\sigma}_{ij}^*/\bar{\sigma}$, where $\bar{\sigma}$ is the remote 'physical dimensional' stress. A covariant stress σ_{ij}^* may be written as $\sigma_{ij}^* = \tilde{\sigma}_{ij}^*(\xi^2 + \eta^2)$. Finally the scaled inner variables, e.g. σ_{ij} , will not have the star superscripts (*) whereas the outer variables will have them, e.g. σ_{ij}^* :

$$\sigma_{ij} = \epsilon \sigma_{ij}^* ; \quad \epsilon_{ij} = \epsilon_{ij}^* ; \quad w^\xi = \frac{w\xi^*}{\epsilon} ; \quad \rho = \frac{\rho^*}{\epsilon^2} ;$$

$$x = \frac{x^*}{\epsilon^2} ; \quad y = \frac{y^*}{\epsilon^2} ; \quad \text{where } \epsilon = \frac{\bar{\sigma}}{E} (1 + \nu).$$

A. Discussion of the Results

The selected root radii of the ellipses in the deformed state range from $\rho = 1$ to 9 which corresponds to a ξ_0 of 1 to 3. The minimum

root radius ($\rho = 1$) is that of a deformed crack as predicted by Inglis [29]. The physical normal stress $\tilde{\sigma}_{nn}$ distribution along the line of symmetry in front of the tip for $\xi_0 = 1.0, 1.3, 1.7$, and 2.5 is shown in Figures 4.1a, 4.2a, 4.3a, 4.4a.* The linear curve referred to here and afterwards concerns the analysis of Inglis. The physical normal stress $\tilde{\sigma}_{nn}$ distribution along the ellipse border for $\xi_0 = 1.0, 1.3, 1.7$ and 2.5 is shown in Figures 4.1b, 4.2b, 4.3b and 4.4b.

Examination of Figures 4.1a and 4.1b show the relative merit of the finite difference as opposed to the collocation methods for solving the nonlinear governing equation. As mentioned previously in Chapter III, for a small number of terms the collocation approach gave fair results; however, for larger numbers of terms the approach became unstable. Therefore the finite difference approach is viewed as being more accurate although they both give qualitatively the same results.

Referring to Figure 4.1a with $\xi_0 = 1.0$, the linear solution falls monotonically from 2.0 at the tip of the deformed ellipse. The nonlinear (finite difference) curve rises from very close to 1.0 to a maximum of 1.24 and then falls, approaching the linear curve from the top. The maximum error then is 50% and this occurs at ξ_0 . The limit analysis predicts that the value of $\tilde{\sigma}_{nn}$ at the ellipse tip should be less than or equal to 1.0 and this agrees with the nonlinear results to within 1%. Referring to Figure 4.1b with $\xi_0 = 1$, both the linear and the nonlinear curves fall monotonically with the linear curve being always above.

*In all of Figures 4, points where inner and outer solutions were matched fell well outside regions shown.

The physical normal stress $\tilde{\sigma}_{\xi\xi}$ distribution along the line of symmetry in front of the tip for $\xi_0 = 1.0, 1.3, 1.7$ and 2.5 is shown in Figures 4.1c, 4.2c, 4.3c and 4.4c. The disparity between the linear and the nonlinear analysis for the physical normal stress $\tilde{\sigma}_{\xi\xi}$ with $\xi_0 = 1.0$ along the line of symmetry can be seen in Figure 4.1c. The maximum difference between the two distributions is 0.05 and is not significant; although, the disparity represents a large percentage because of the small magnitude of the stress.

In linear fracture mechanics the single parameter of interest is the stress intensity factor K which defines the field strength of the singular behavior. For a crack, as shown in Figure 2.2, K as defined by Sneddon and Lowengrub [31] is $\lim_{x \rightarrow 0} \sqrt{2x^*} \tilde{\sigma}_{nn}^*(x,0)$. The linear solution with $\xi_0 = 0$ would then give K_{TH} as $\bar{\sigma}\sqrt{c}$. Defining an "apparent" stress intensity factor as $K_{AP} = \sqrt{2x^*} \tilde{\sigma}^*$, then one obtains

$\frac{K_{AP}}{K_{TH}} = \sqrt{2x} \tilde{\sigma}_{nn}$. Hence, in Figures 4.1d, 4.2d, 4.3d and 4.4d for $\xi_0 = 1.0, 1.3, 1.7$ and 2.5 the apparent stress intensity factor K_{AP} is shown, with the 'singular' curve representing the linear solution to the undeformed crack geometry ($\xi_0 = 0$). The error involved in the calculation of stress intensity factors for $\xi_0 = 1$ is shown in Figure 4.1d. The nonlinear curve represents the K_{AP} that would be calculated from data taken from an actual experiment. If the data were taken outside of $x = 16$, there would be only an error of 2%. However, the error would rise to +20% and then drop to -100% as x decreases to zero. The linear analysis predicts that the error would rise to +10% before

dropping to -100%. These results are consistent with recent experimental findings [10], [14], [18].

The physical maximum in-plane shear stress (the primary quantity used in photoelastic experiments) τ_{\max} along a line originating at the tip, perpendicular to the line of symmetry, for $\xi_0 = 1.0, 1.3, 1.7$ and 2.5 is shown in Figures 4.1e, 4.2e, 4.3e and 4.4e. The difference between the nonlinear and the linear formulations with $\xi_0 = 1$ for τ_{\max} is shown in Figure 4.1e. The maximum difference between the linear and the nonlinear is $+50\%$ and occurs at the tip. Therefore, the linear approach represents the τ_{\max} distribution well until $y < 1 \sim \rho$; i.e. inside of one root radius it is necessary to go to the nonlinear representation.

After integrating the strain displacement equations (3.9) for the covariant displacements (w_ξ, w_η) the contravariant counterparts can then be determined:

$$w^\xi = \frac{w_\xi}{(\xi^2 + \eta^2)} ; \quad w^\eta = \frac{w_\eta}{(\xi^2 + \eta^2)}$$

These displacements can then be used to find the initial geometry:

$$\xi_{\text{initial}} = \xi_{\text{final}} - w^\xi \quad (4.1a)$$

$$\eta_{\text{initial}} = \eta_{\text{final}} - w^\eta \quad (4.1b)$$

The contravariant displacement w^ξ distribution along the line of symmetry for $\xi_0 = 1.0, 1.3, 1.7$ and 2.5 is shown in Figures 4.1f, 4.2f, 4.3f and 4.4f. The difference between the linear and the nonlinear curves for $\xi_0 = 1$ is shown in Figure 4.1f. The error is within 3%

until very close to the tip: here the error rises to 8%. The linear displacements would map this ellipse exactly into a crack; and therefore, the small difference between the displacement curves indicates that the nonlinear analysis of an ellipse of $\xi_0 = 1$ would closely resemble that of a crack (in the initial geometry), except near the tip itself.

Figure 4.5 shows the variation of the physical normal stress $\tilde{\sigma}_{nn}$ distribution along the line of symmetry for the range of final, deformed root radii $\rho = 1 \rightarrow 9$. From this figure it can be seen that the maximum value of the physical normal stress $\tilde{\sigma}_{nn}$ occurs at the ellipse tip ($\xi = \xi_0$) for $\xi_0 \geq 1.7$; however, for $\xi_0 < 1.7$ the maximum occurs at some distance ($\xi > \xi_0$) in front of the tip. This phenomenon suggests two different types of crack growth: 1) if the root radius of the notch is above some critical level, the flaw will extend from the edge of the blunted notch as reported by Schijve and Jacobs [32]; 2) if the root radius of the notch is below some critical level, the flaw will extend by the creation of crack segments ahead of the sharp notch as cited by Yokobori [33].

The distribution of the physical normal strain $\tilde{\epsilon}_{nn}$ along the line of symmetry in front of the tip for the range of final root radii $\rho = 1 \rightarrow 9$ is shown in Figure 4.6. The limit analysis showed that a physical strain $\tilde{\epsilon}_{nn}$ value of 0.5 was impossible; in fact, this value would only be reached near the crack tip. The above figure bears out this conclusion in that all of the curves are asymptotic to 0.5 at $\xi = \xi_0$.

From the contravariant displacements shown in Figures 4.1f through 4.4f the initial geometry of the ellipses can be determined through equations (4.1). Via this procedure the initial root radii of the deformed ellipses are found and they are presented in Figure 4.7. The linear analysis as presented in this figure would give an ellipse as the initial geometry; however, the nonlinear analysis would not and the difference between the two curves represent the amount the initial geometry would differ from an ellipse. From the extrapolation of this curve it is clear that a crack initially with no load would deform into a quasi-elliptical shape with a root radius of $(0.92)^2$. From the displacements for $\xi_0 = 1.0$ it is clear that the crack will deform into an ellipse of shape $\xi_0 = 1.0$ at some distance from the tip. It can be stated, therefore, that the behavior in the neighborhood of the tip can be well approximated by an ellipse of $\xi_0 = 0.92$ and that away from the tip the behavior can be determined by an ellipse of $\xi_0 = 1.0$.

Using Figures 4.5 and 4.7 the magnitude and the location of the maximum normal stress $\tilde{\sigma}_{nn\max}$ can be plotted with respect to the initial root radius as is shown in Figures 4.8 and 4.9, respectively. Extrapolating the curve on Figure 4.8 the maximum normal stress $\tilde{\sigma}_{nn}$ becomes 1.3, approximately; and referring to Figure 4.9 the location of the maximum stress becomes $x/\rho = 0.33$, so that $x = 0.33(0.92)^2 = 0.28$. It could be conjectured that the shift of the maximum stress in front of the tip could be as a result of the additional constraint in the interior of the body.

The near field zone of the present model extends to $O(\epsilon^2)$ from the crack tip as contrasted with $O(\epsilon)$ in the Rice-Rosengren [21] and Hutchinson [22] models, and therefore is a very near field solution. The model reveals that the strains are limited as shown in Figure 4.6; physically this means that, upon application of small remote stresses, the portion of the crack surfaces nearest the tip each undergo a rotation of 90° in opposite directions in creating the notch tip. This produces stresses of the order of Young's modulus at the notch tip (Fig. 4.5) as in [25][26] but these local stresses are independent of the applied remote stress. Increasing the remote stress simply enlarges the root radius, and with it the size of the zone affected by the finite deformations. These features (i.e. stresses of the order of the modulus and independence of the near field stress from the remote loads) are also found in the "cohesive" stress field of the Barenblatt model [34]. Moreover, the "hump" in the $\tilde{\sigma}_{nn}$ stress distribution shown in Figure 4.5 for small root radii produces qualitatively the same sort of stress distribution very near the notch tip as Neuber obtained with his "limiting particle size" theory for pointed notches [35].

For stress freezing photoelastic materials above critical temperature, the maximum stress is expected to be one order of magnitude below Young's modulus and this adjustment might possibly be incorporated into the present model by introducing non-linear constitutive relations. This change would also be expected to enlarge the size of the affected zone (currently of the order of one root radius) to perhaps several root radii.

B. Conclusions

A finite deformation analysis of the near field surrounding the tip of small crack-like ellipses was performed in the deformed geometry using the complete compatibility equations and linear constitutive relations.

The effects of finite strains and rotations in the tip region of a deformed crack were found

- (1) to reduce $\tilde{\sigma}_{nn}$, $\tilde{\tau}_{max}$ and $\tilde{\epsilon}_{nn}$ at the tip by 50%;
- (2) to move $\tilde{\sigma}_{nn_{max}}$ 0.33 root radii away from the tip ($\tilde{\sigma}_{nn_{max}} = 1.3$);
- (3) to reduce ρ_{final} to $(0.92)^2$;
- (4) to change $\tilde{\sigma}_{\xi\xi}$ insignificantly.

These contributions are all extremely local and are concentrated within a few root radii of the tip and would not normally be measurable in a photoelastic experiment; however, the effects of crack tip blunting are more general and spread back to ten or more root radii. For initial geometries with blunted tips, the regions of influence cited above are generally the same (in terms of root radii) although the magnitudes of the above effects are less. The above results suggest that blunt notches propagate from the notch tip; however, sharp notches extend from the formation and subsequent growth of small cracks in front of the notch.

The features of the present model are believed to be qualitatively appropriate to behavior of photoelastic materials above critical temperature. Studies are currently underway for the inclusion of non-linear constitutive relations in order to improve its quantitative predictions and hopefully shed new light on the large strain region very near the crack tip.

ACKNOWLEDGEMENTS

The authors wish to acknowledge the assistance of G. W. Swift in formulating suitable computer programs, the staff and facilities of the Engineering Science and Mechanics Department at VPI and SU, and the support of the National Science Foundation under grant No. GK 39922.

REFERENCES

- [1] Irwin, G. R., Discussion of the paper "The Dynamic Stress Distribution Surrounding a Running Crack - A Photoelastic Analysis" by A. A. Wells and D. Post Proceedings Society for Experimental Stress Analysis 16, 1, 69-96 (1958).
- [2] Marloff, R. H., Leven, M. M., Johnson, R. L., and Ringler, T. N., "Photoelastic Determination of Stress Intensity Factors", Experimental Mechanics 11, 12, 529-239 (Dec., 1971).
- [3] Smith, D. G. and Smith, C. W., "A Photoelastic Evaluation of the Influence of Closure and Other Effects upon the Local Bending Stresses in Cracked Plates", International Journal of Fracture Mechanics 6, 3, 305-318 (Sept. 1970).
- [4] Smith, D. G. and Smith, C. W., "Influence of Precatastrophic Extension and Other Effects on Local Stresses in Cracked Plates under Bending Fields", Experimental Mechanics 11, 9, 394-401 (Sept. 1971).
- [5] Smith, D. G. and Smith, C. W., "Photoelastic Determination of Mixed Mode Stress Intensity Factors", VPI-E-70-16, June 1970. J. of Engineering Fracture Mechanics 4, 2, 357-366, (June 1972).
- [6] Bradley, W. B. and Kobayashi, A. S., "An Investigation of Propagating Cracks by Dynamic Photoelasticity," J. of Experimental Mechanics 10, 3, 106-113 (March, 1970).
- [7] Bradley, W. B. and Kobayashi, A. S., "Fracture Dynamics - A Photoelastic Investigation," J. of Engineering Fracture Mechanics 3, 3, 317-332 (October, 1971).
- [8] Kobayashi, A. S., Wade, B. G., Bradley, W. B., and Chiu, S. T., "Crack Branching in Homalite - 100 Sheets" TR-13 Dept. of Mechanical Engineering, College of Engineering, University of Washington, Seattle, Wash. (June 1972).
- [9] Kobayashi, A. S. and Wade, B. G., "Crack Propagation and Arrest in Impacted Plates" TR-14 Dept. of Mechanical Engineering, College of Engineering, University of Washington, Seattle, Wash. (July 1972).

- [10] Schroedl, M. A., McGowan, J. J. and Smith, C. W., "An Assessment of Factors Influencing Data Obtained by the Photoelastic Stress Freezing Technique for Stress Fields Near Crack Tips", J. of Engineering Fracture Mechanics 4, 4, Dec. 1972.
- [11] Ronay, M. and Freudenthal, A. M., "Second Order Effects in Dissipative Solids", Tech. Rep. No. 13, Dept. of Civil Eng. and Eng. Mech., Columbia University, New York, N.Y. (Jan. 1965).
- [12] Poynting, J. W., Proc. Roy. Soc. London A, Vol 82, 546-559 (1909) Vol. 86, 534-561 (1912).
- [13] Fessler, W. and Mansell, D. O., "Photoelastic Study of Stresses near Cracks in Thick Plates", Journal of Mechanical Engineering Science, 4 (3), 213-225 (Sept. 1962).
- [14] Smith, C. W., "Use of Three Dimensional Photoelasticity in Fracture Mechanics" (Invited Paper) Third International Congress on Experimental Mechanics, Los Angeles, Calif., May 13-18, 1973 (In Press), Conference Proceedings and J. of Experimental Mechanics.
- [15] Kassir, M. and Sih, G. C., "Griffith's Theory for Brittle Fracture in Three Dimensions", International Journal of Engineering Science 5, 12, 899-918, Dec. 1967.
- [16] Marrs, G. R. and Smith, C. W., "A Study of Local Stresses Near Surface Flaws in Bending Fields", Stress Analysis and Growth of Cracks, ASTM STP 513, 22-36 (Oct. 1972).
- [17] Schroedl, M. A. and Smith, C. W., "Local Stresses Near Deep Surface Flaws Under Cylindrical Bending Fields", VPI-E-72-9 (In Press) Progress in Flaw Growth and Fracture Toughness Testing, ASTM STP 536, Oct. 1973.
- [18] Schroedl, M. A., McGowan, J. J. and Smith, C. W., "Determination of Stress Intensity Factors from Photoelastic Data with Application to Surface Flaw Problems" (In Press), VPI-E-73-1, (Feb. 1973).
- [19] Harms, A. E. and Smith, C. W., "Stress Intensity Factors in Long Deep Surface Flaws in Plates Under Extensional Fields" (In Press) VPI-E-73-6 (Feb. 1973).
- [20] Rice, J. R. and Johnson M. A., "The Role of Large Crack Tip Geometry Changes in Fracture", Inelastic Behavior of Solids (M.F. Kanninen et al, eds.), McGraw-Hill, N. Y., 1920.

- [21] Rice, J. R., and Rosengren, G. F. , "Plane Strain Deformation Near a Crack Tip in a Power-Law Hardening Material", Journal of the Mechanics and Physics of Solids, 16, 1, 1 (1968).
- [22] Hutchinson, J. W., "Singular Behavior at the End of a Tensile Crack in a Hardening Material", Journal of the Mechanics and Physics of Solids, 16, 1, 13 (1968).
- [23] Knowles, J.K., and Sternberg, Eli, "Asymptotic Finite Deformation Analysis of the Elastostatic Field Near the Tip of the Crack", Cal. Inst. Tech., Div. Eng. and Appl. Sc., Tech. Rept. 27 (1973). (See also TR No. 29 March 1974)
- [24] Knowles, J.K. and Sternberg, E., "Finite Deformation Analysis of the Elastostatic Field Near the Tip of a Crack: Reconsideration of Higher Order Results" Cal. Inst. of Tech., Div. Eng. and Appl. Sc., Tech. Rept. 29, March (1974).
- [25] Bowie, O. L. "Effect of the Small Displacement Approximation in Elasticity on the Solution of an Elliptical Hole" Rept. No. WAL 893/185 Watertown Arsenal, Watertown, Mass. 02172
- [26] Mansfield, E. H., "On the Stresses Near a Crack in an Elastic Sheet", Int. J. Of Non-Linear Mechanics, 4, 129-142 (1969).
- [27] Sokolnikoff, I. S., Tensor Analysis, John Wiley and Sons, New York (1967).
- [28] Adkins, J. E., Green, A. E., and Shield, R. T., "Finite Plane Strain", Phil. Trans., A, 246 (1953).
- [29] Inglis, C. E., "Stresses in a Plate Due to the Presence of Cracks and Corners, Trans. Instn. Naval. Archit., 55, 219 (1913).
- [30] Van Dyke, M., Perturbation Methods in Fluid Mechanics, Academic Press, New York (1968).
- [31] Sneddon, I. N. and Lowengrub, M., Crack Problems in the Classical Theory of Elasticity, Wiley and Sons, 2-6 (1969).
- [32] Schijve, J. and Jacobs, F. A., "Fatigue Crack Propagation in Unnotched and Notched Aluminum Alloy Specimens", NLR-TR-M 2128 N.A.T. Aero-Astro. Res. Inst., Amsterdam, (1964).
- [33] Yokobori, T., The Strength, Fracture and Fatigue of Materials, P. Noordhoff, Groningen, 228 (1965).
- [34] Barenblatt, G. I., "Mathematical Theory of Equilibrium Cracks in Brittle Fracture," Advances in Applied Mechanics, VII, Academic Press, New York (1962).
- [35] Neuber, H., Kerbspennungslehre, Springer Berlin 1937, English Translation available from Edwards Bros. Ann Arbor, Michigan.

APPENDIX A

The coefficients $i j k F_m$ as they appear in equation (3.2) are

$$\begin{aligned}
 \xi\xi_{\Delta} &= 2A_1 + 4(\phi_{,\eta\eta} + 2A_2 (\phi_{,\xi\xi} + \phi_{,\eta\eta})); \quad \xi\eta_{\Delta} = -8\phi_{,\xi\eta} \\
 \eta\eta_{\Delta} &= 2A_1 + 4(\phi_{,\xi\xi} + 2A_2 (\phi_{,\xi\xi} + \phi_{,\eta\eta})); \quad \xi\xi_{\Delta 1} = 2A_3 \\
 \eta\eta_{\Delta 1} &= 2A_4; \quad \xi\xi_{\Delta} = 2A_4; \quad \eta\eta_{\Delta} = 2A_3; \quad \xi\eta_{\Delta} = 2; \\
 \xi\xi\xi F_1 &= 2B_1/B_0 \phi_{,\xi\xi\xi} + B_3/B_0 \phi_{,\xi\eta\eta}; \quad \xi\xi\eta F_1 = 2B_5/B_0 \phi_{,\xi\xi\eta} + B_6/B_0 \phi_{,\eta\eta\eta} \\
 \xi\eta\eta F_1 &= 2B_2/B_0 \phi_{,\xi\eta\eta} + B_3/B_0 \phi_{,\xi\xi\xi}; \quad \eta\eta\eta F_1 = 2B_4/B_0 \phi_{,\eta\eta\eta} + B_6/B_0 \phi_{,\xi\xi\eta} \\
 \xi\xi\xi F_2 &= 2B_4/B_0 \phi_{,\xi\xi\xi} + B_6/B_0 \phi_{,\xi\eta\eta}; \quad \xi\xi\eta F_2 = 2B_2/B_0 \phi_{,\xi\xi\eta} + B_3/B_0 \phi_{,\eta\eta\eta} \\
 \xi\eta\eta F_2 &= 2B_5/B_0 \phi_{,\xi\eta\eta} + B_6/B_0 \phi_{,\xi\xi\xi}; \quad \eta\eta\eta F_2 = 2B_1/B_0 \phi_{,\eta\eta\eta} + B_3/B_0 \phi_{,\xi\xi\eta} \\
 \xi\xi\xi F_3 &= C_2/B_0 \phi_{,\eta\eta\eta} + C_3/B_0 \phi_{,\xi\xi\xi}; \quad \xi\xi\eta F_3 = C_1/B_0 \phi_{,\xi\eta\eta} + C_3/B_0 \phi_{,\xi\xi\xi} \\
 \xi\eta\eta F_3 &= C_1/B_0 \phi_{,\xi\eta\eta} + C_3/B_0 \phi_{,\eta\eta\eta}; \quad \eta\eta\eta F_3 = C_2/B_0 \phi_{,\xi\xi\xi} + C_3/B_0 \phi_{,\xi\eta\eta}.
 \end{aligned}$$

The physical covariant derivatives of ϕ in the parabolic coordinate system with $h^2 = g = \xi^2 + \eta^2$ are

$$\begin{aligned}
 \nabla^4 \phi &= \left(\frac{\partial^4 \phi}{\partial \xi^4} + 2 \frac{\partial^4 \phi}{\partial \xi^2 \partial \eta^2} + \frac{\partial^4 \phi}{\partial \eta^4} - 4 \frac{\xi}{g} \frac{\partial^3 \phi}{\partial \xi^3} - 4 \frac{\eta}{g} \frac{\partial^3 \phi}{\partial \xi^2 \partial \eta} \right. \\
 &\quad \left. - 4 \frac{\xi}{g} \frac{\partial^3 \phi}{\partial \xi \partial \eta^2} - 4 \frac{\eta}{g} \frac{\partial^3 \phi}{\partial \eta^3} + \frac{4}{g} \frac{\partial^2 \phi}{\partial \xi^2} + \frac{4}{g} \frac{\partial^2 \phi}{\partial \eta^2} \right) / g^2 \\
 \phi_{,\xi\xi\xi} &= \left(\frac{\partial^3 \phi}{\partial \xi^3} - 3 \frac{\xi}{g} \frac{\partial^2 \phi}{\partial \xi^2} + 3 \frac{\eta}{g} \frac{\partial^2 \phi}{\partial \xi \partial \eta} + 3 \frac{(\xi^2 - \eta^2)}{g^2} \frac{\partial \phi}{\partial \xi} - 6 \frac{\xi \eta}{g^2} \frac{\partial \phi}{\partial \eta} \right) / h^3 \\
 \phi_{,\xi\xi\eta} &= \left(\frac{\partial^3 \phi}{\partial \xi^2 \partial \eta} - 2 \frac{\eta}{g} \frac{\partial^2 \phi}{\partial \xi^2} - 3 \frac{\xi}{g} \frac{\partial^2 \phi}{\partial \xi \partial \eta} + \eta/g \frac{\partial^2 \phi}{\partial \eta^2} + 6 \frac{\xi \eta}{g^2} \frac{\partial \phi}{\partial \xi} \right)
 \end{aligned}$$

$$+ 3 \frac{(\xi^2 - \eta^2)}{g^2} \frac{\partial \phi}{\partial \eta} / h^3$$

$$\begin{aligned}\phi_{,\xi\eta\eta} &= \left(\frac{\partial^3 \phi}{\partial \xi \partial \eta^2} + \frac{\xi}{g} \frac{\partial^2 \phi}{\partial \xi^2} - 3 \frac{\eta}{g} \frac{\partial^2 \phi}{\partial \xi \partial \eta} - 2 \frac{\xi}{g} \frac{\partial^2 \phi}{\partial \eta^2} - 3 \frac{(\xi^2 - \eta^2)}{g^2} \frac{\partial \phi}{\partial \xi} \right. \\ &\quad \left. + 6 \frac{\xi \eta}{g^2} \frac{\partial \phi}{\partial \eta} \right) / h^3\end{aligned}$$

$$\phi_{,\eta\eta\eta} = \left(\frac{\partial^3 \phi}{\partial \eta^3} + 3 \frac{\xi}{g} \frac{\partial^2 \phi}{\partial \xi \partial \eta} - 3 \frac{\eta}{g} \frac{\partial^2 \phi}{\partial \eta^2} - 6 \frac{\xi \eta}{g^2} \frac{\partial \phi}{\partial \xi} - 3 \frac{(\xi^2 - \eta^2)}{g^2} \frac{\partial \phi}{\partial \eta} \right) / h^3$$

$$\phi_{,\xi\xi} = \left(\frac{\partial^2 \phi}{\partial \xi^2} - \frac{\xi}{g} \frac{\partial \phi}{\partial \xi} + \frac{\eta}{g} \frac{\partial \phi}{\partial \eta} \right) / g$$

$$\phi_{,\xi\eta} = \left(\frac{\partial^2 \phi}{\partial \xi \partial \eta} - \frac{\eta}{g} \frac{\partial \phi}{\partial \xi} - \frac{\xi}{g} \frac{\partial \phi}{\partial \eta} \right) / g$$

$$\phi_{,\eta\eta} = \left(\frac{\partial^2 \phi}{\partial \eta^2} + \frac{\xi}{g} \frac{\partial \phi}{\partial \xi} - \frac{\eta}{g} \frac{\partial \phi}{\partial \eta} \right) / g .$$

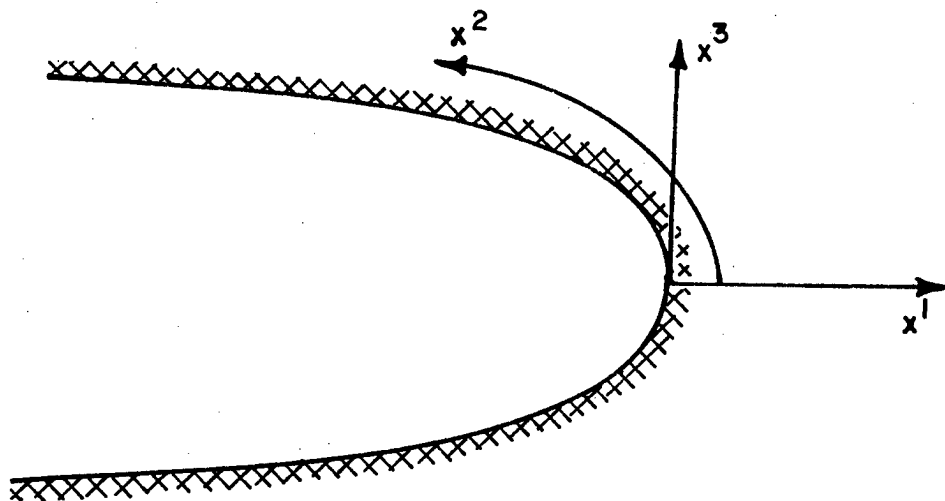
The physical covariant derivatives of w_ξ and w_η as they appear in equations (3.11) and (3.9) are

$$\tilde{w}_{\xi,\xi} = \left(\frac{\partial w_\xi}{\partial \xi} - \frac{\xi}{g} w_\xi + \frac{\eta}{g} w_\eta \right) / g$$

$$\tilde{w}_{\xi,\eta} = \left(\frac{\partial w_\xi}{\partial \eta} - \frac{\eta}{g} w_\xi - \frac{\xi}{g} w_\eta \right) / g$$

$$\tilde{w}_{\eta,\xi} = \left(\frac{\partial w_\eta}{\partial \xi} - \frac{\eta}{g} w_\xi - \frac{\xi}{g} w_\eta \right) / g$$

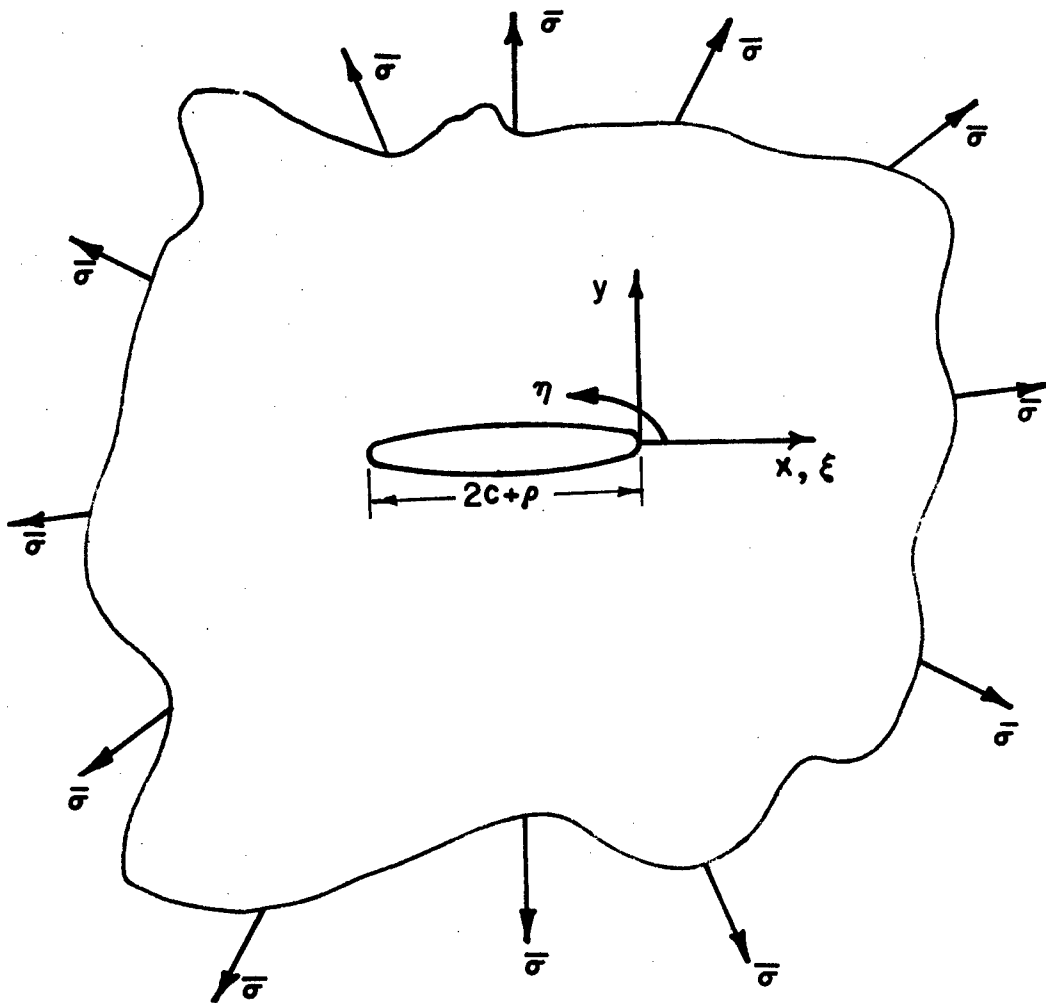
$$\tilde{w}_{\eta,\eta} = \left(\frac{\partial w_\eta}{\partial \eta} + \frac{\xi}{g} w_\xi - \frac{\eta}{g} w_\eta \right) / g$$



$(ds)^2 = g_{ij} dx^i dx^j$ for the deformed geometry

$(ds)^2 = h_{ij} dx^i dx^j$ for the undeformed geometry

Figure 2.1 Coordinate System

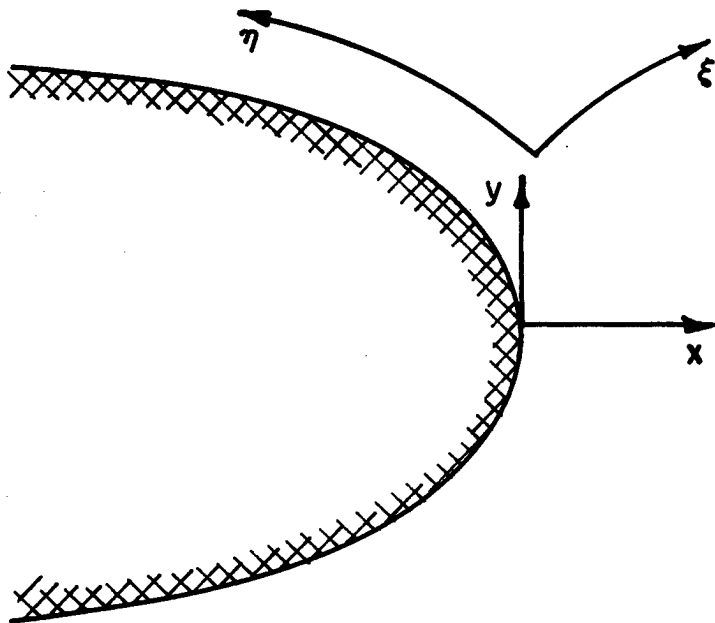


for the elliptical coordinates

$$x = \cosh \xi \cosh \eta, \quad y = \sinh \xi \sinh \eta$$

$$g_{22} = g_{11} = \frac{\cosh 2\xi - \cos 2\eta}{2}, \quad g_{12} = g_{21} = 0$$

Figure 2.2 Problem Geometry



for the parabolic coordinates

$$x = \frac{(\xi^2 - \xi_0^2 - \eta^2)}{2}, \quad y = \xi\eta, \quad g_{ss} = g_{zz} = g = (\xi^2 + \eta^2)$$

Figure 2.3 Inner Region Geometry

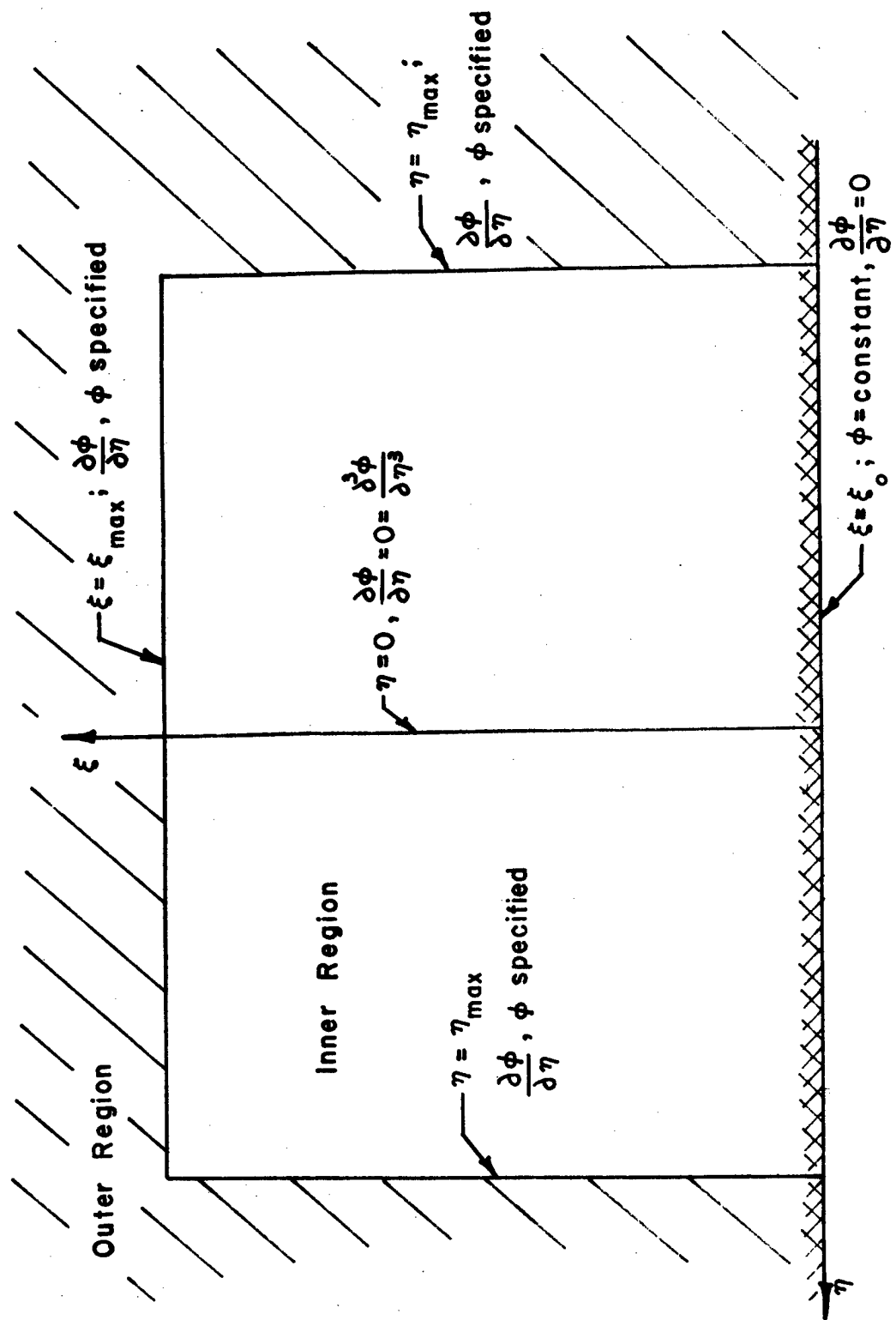
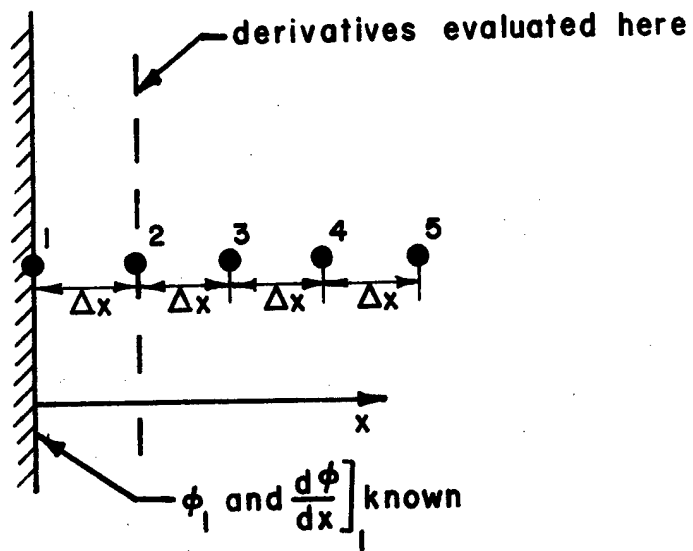
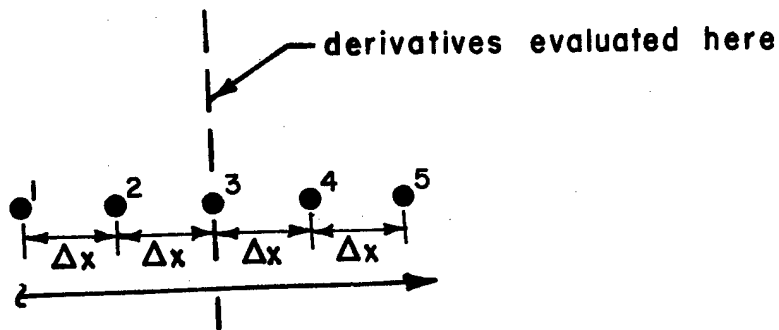


Figure 2.4 Perturbation Scheme

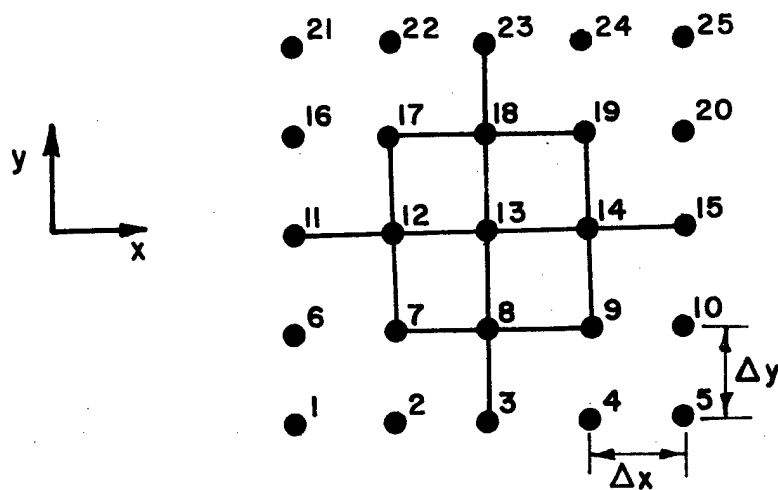


(a) Scheme Used Near a Boundary

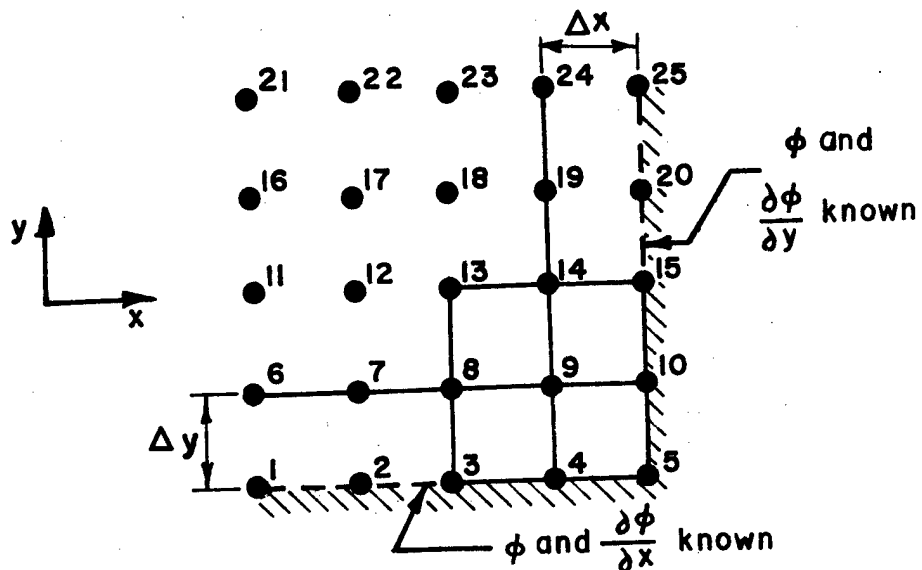


(b) Scheme Used Away From a Boundary

Figure 3.1 One-Dimensional Finite Difference Schemes



(a) Scheme Used Away From All Boundaries



(b) Scheme Used Near Two Boundaries

Figure 3.2 Two-Dimensional Finite Difference Schemes

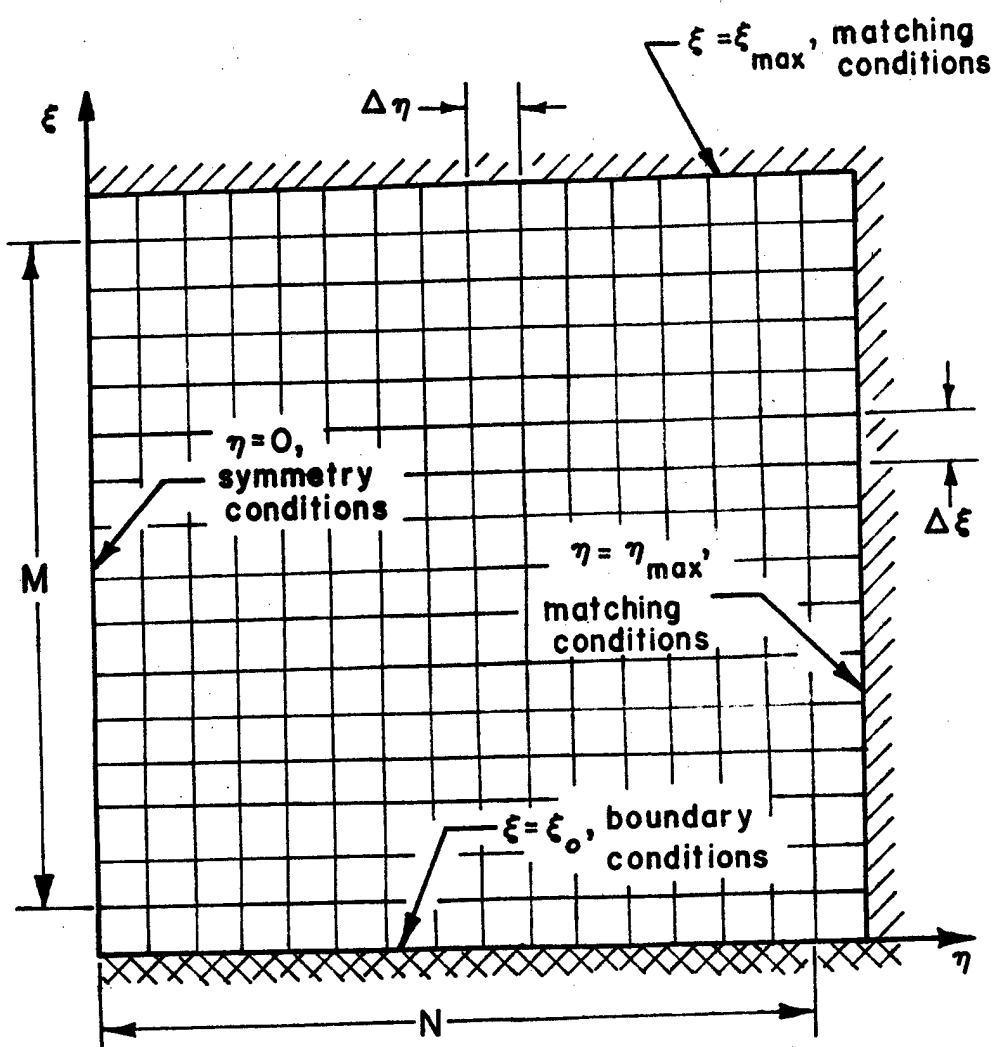


Figure 3.3 Grid Pattern

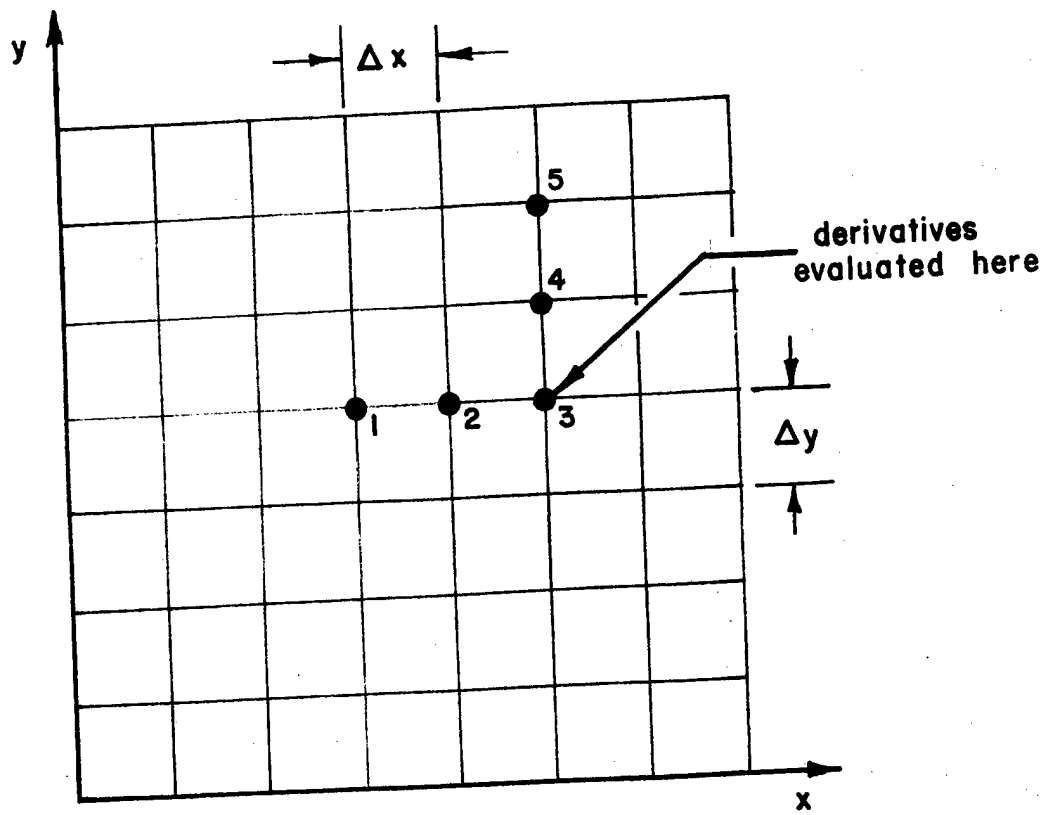


Figure 3.4 Finite Difference Scheme Used for Strain Integration

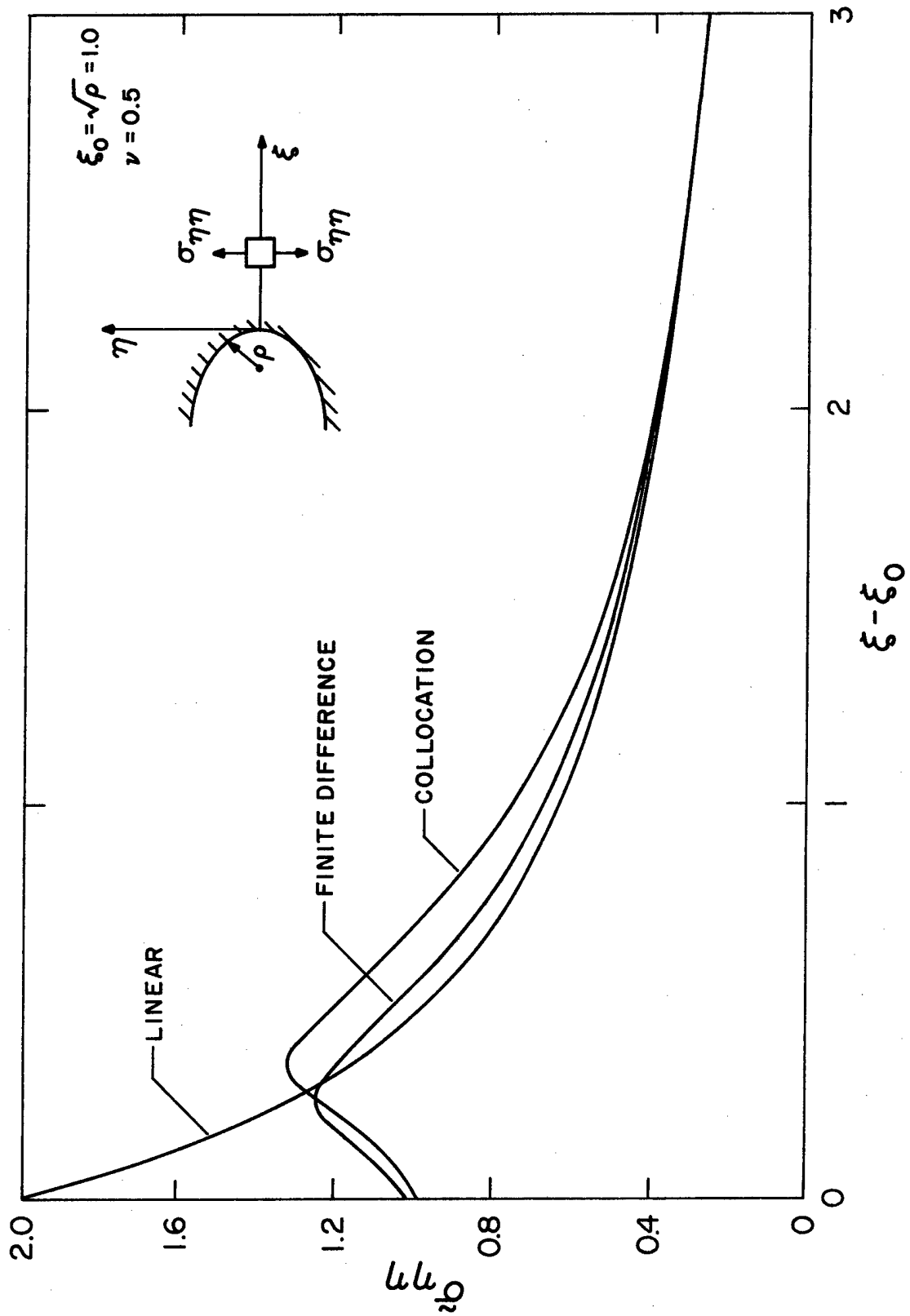


Figure 4.1a Physical Normal Stress $\tilde{\sigma}_{\eta\eta}$ Distribution Along the Line of Symmetry for $\xi_0 = 1.0$.

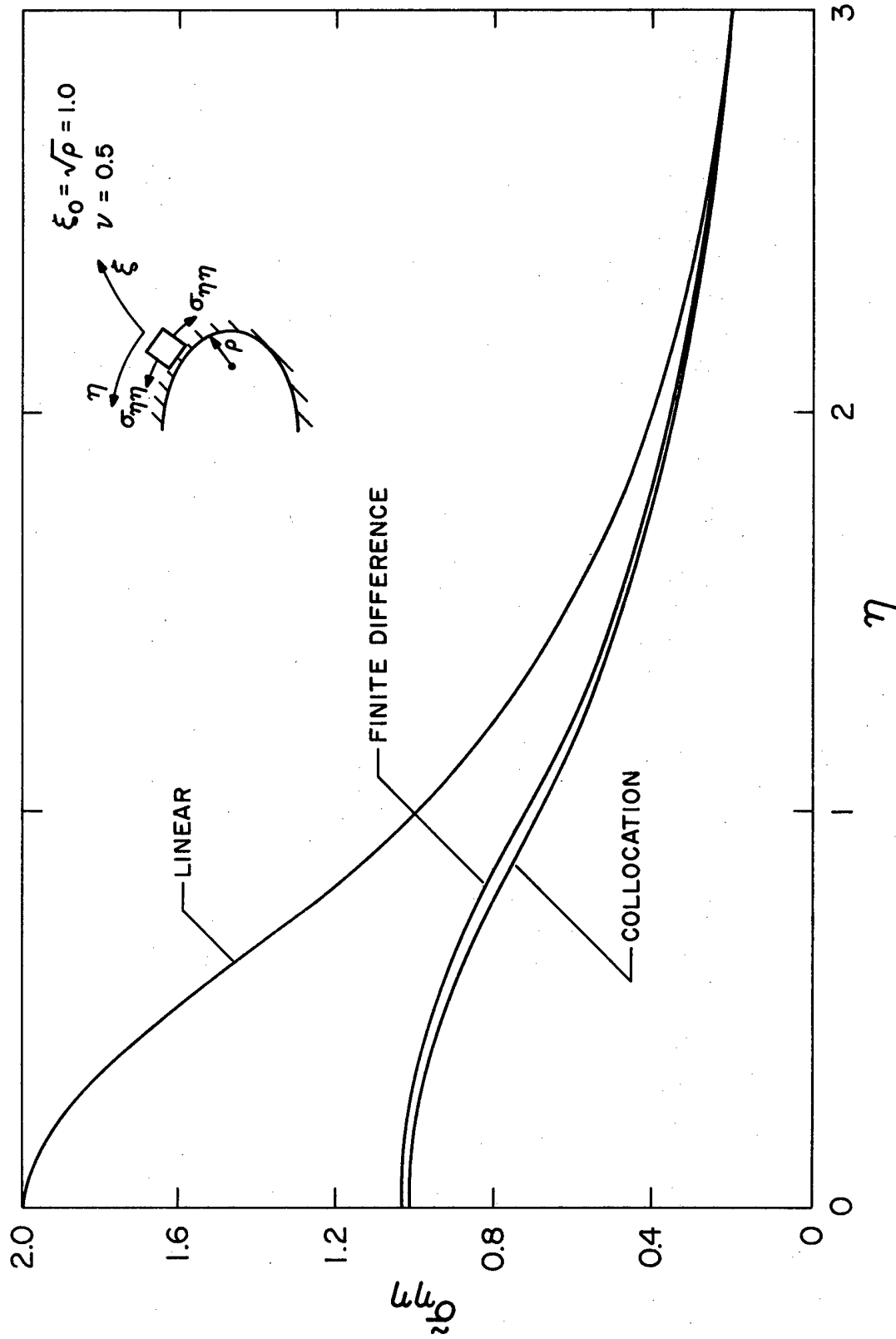


Figure 4.1b Physical Normal Stress ξ_0 Distribution Along the Ellipse Border for $\xi_0 = 1.0$.

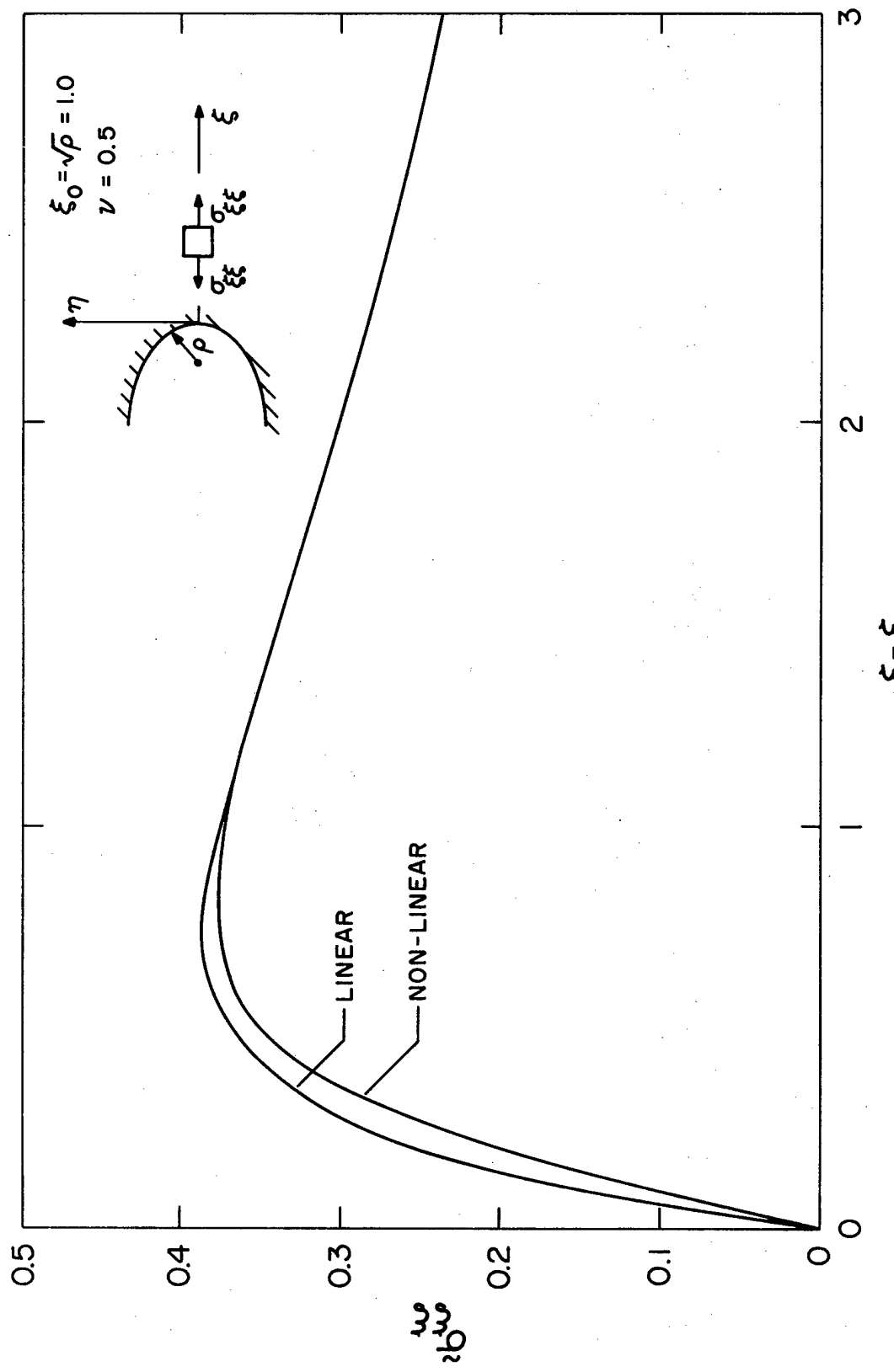


Figure 4.1c Physical Normal Stress $\tilde{\sigma}_{\xi\xi}$ Distribution Along the Line of Symmetry for $\xi_0 = 1.0$.

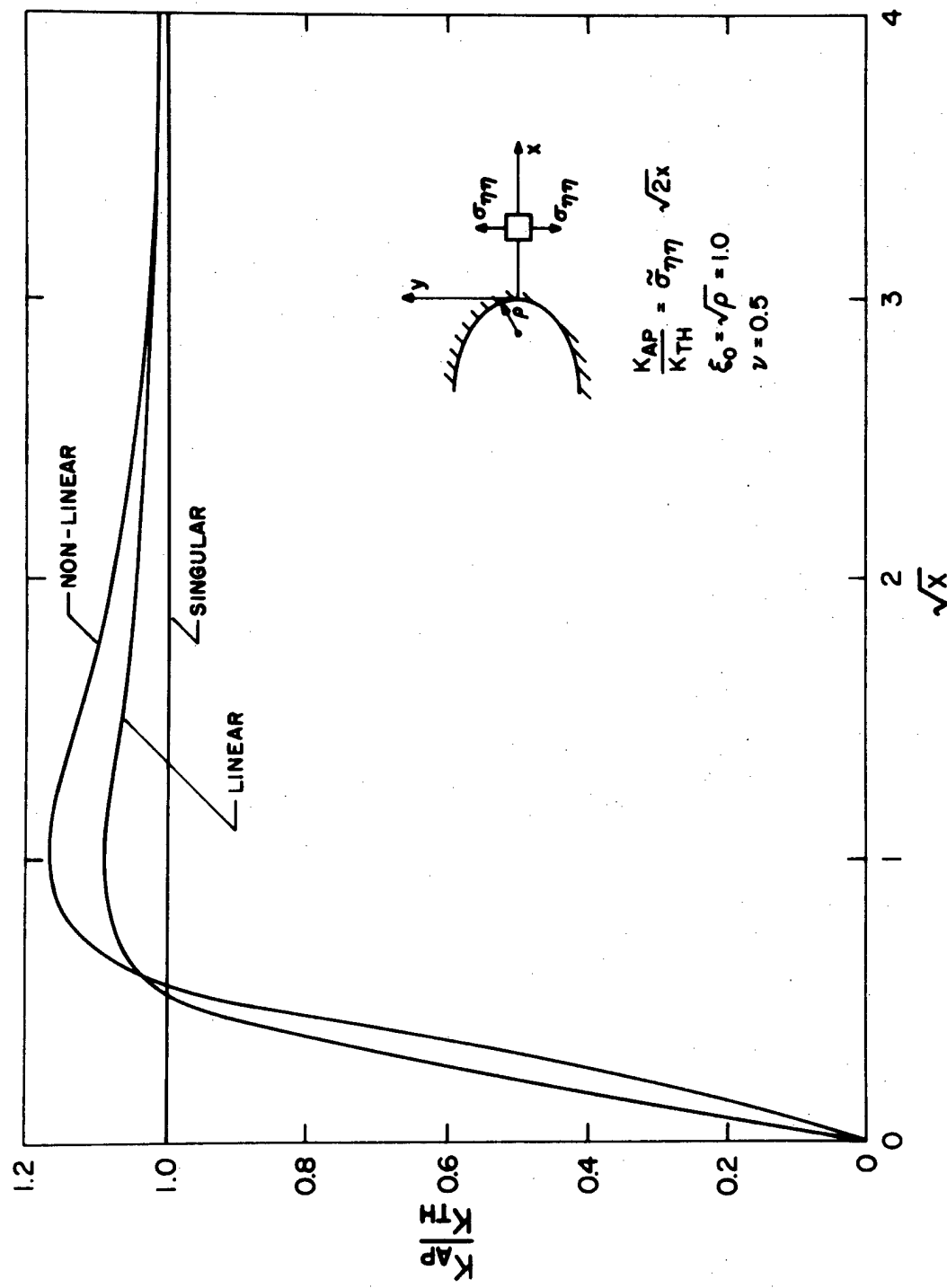


Figure 4.1d Apparent Stress Intensity Factor Distribution Along the Line of Symmetry for $\xi_0 = 1.0$.

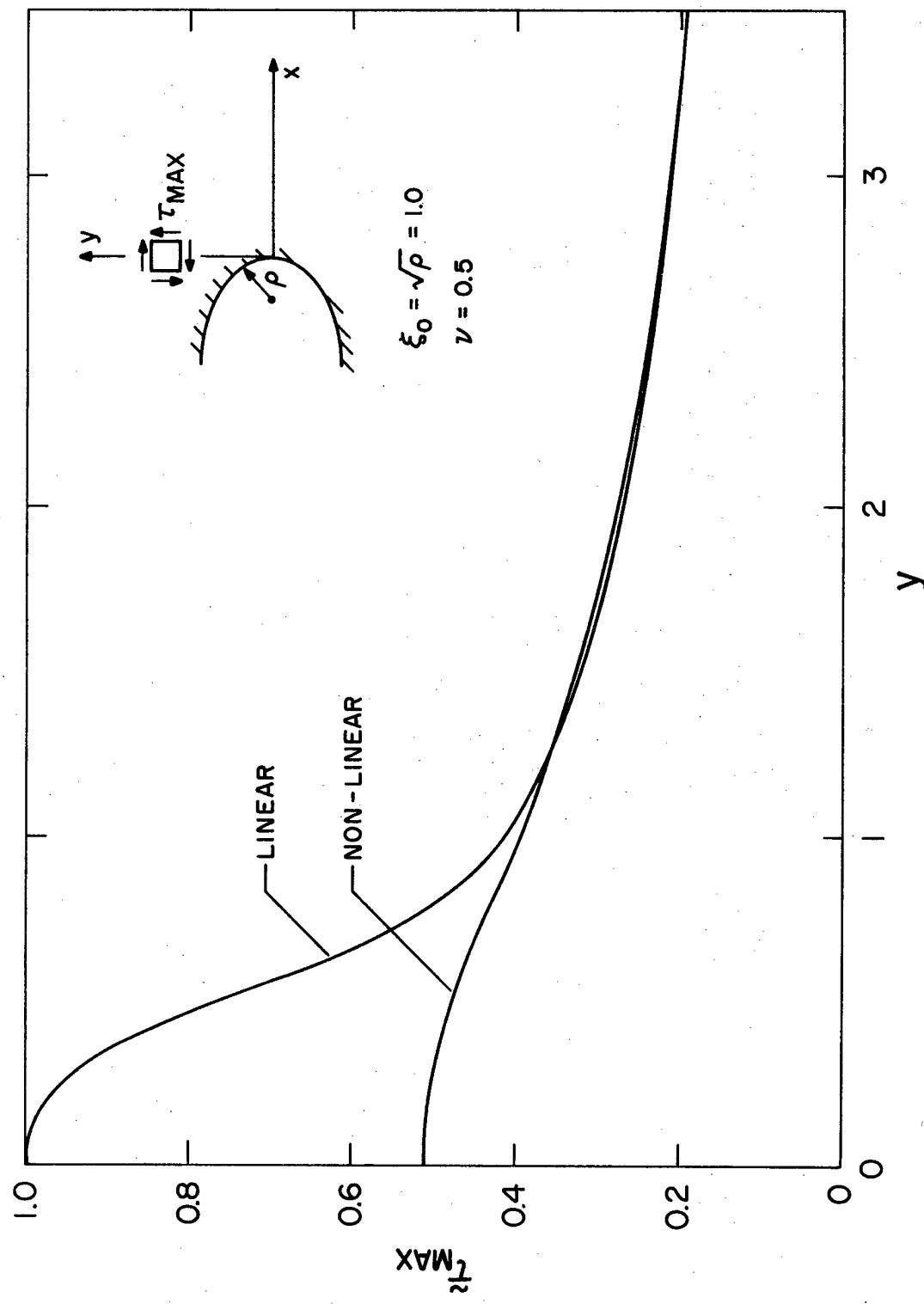


Figure 4.1e Physical Maximum In-Plane Shear Stress Distribution for $\xi_0 = 1.0$.

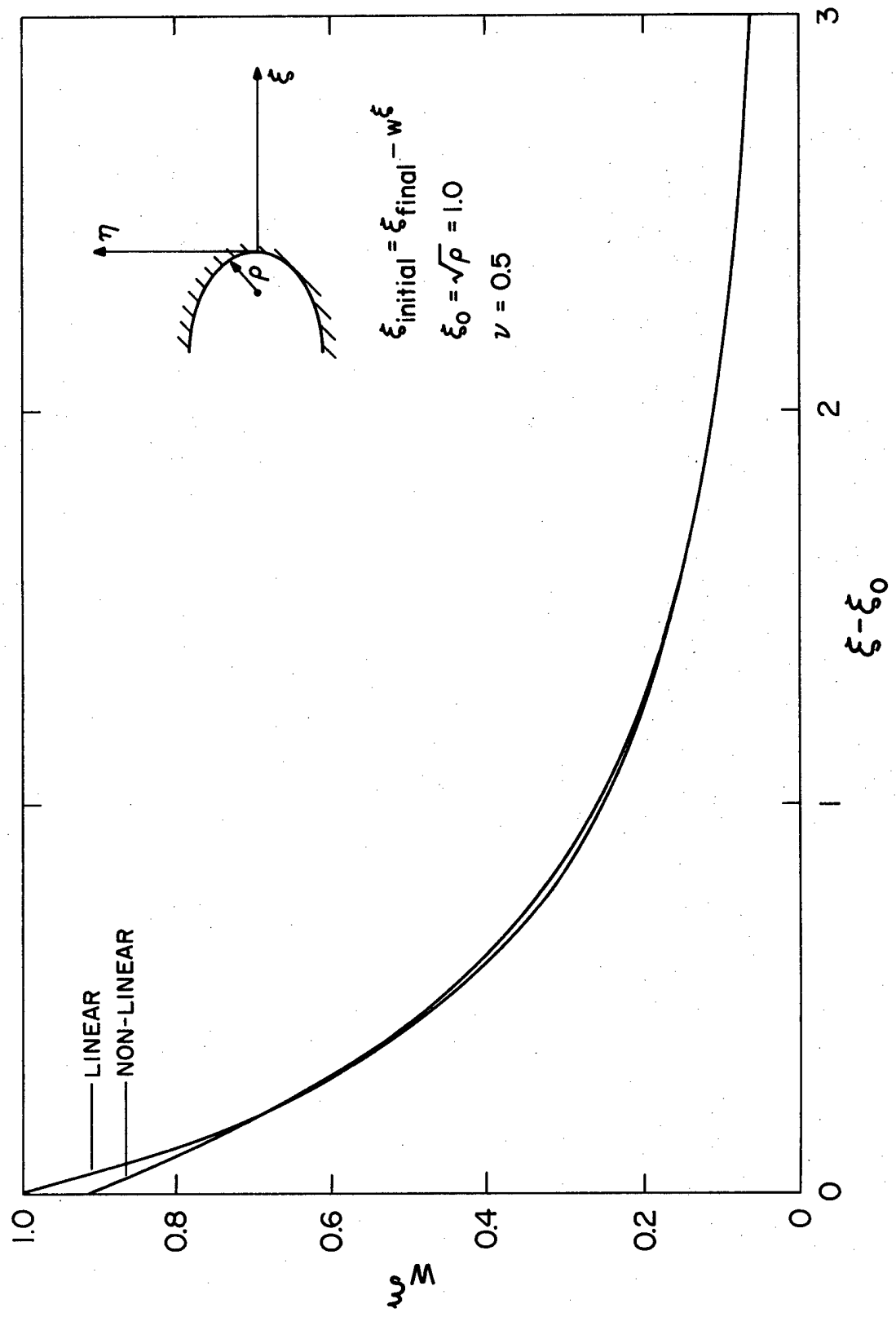


Figure 4.1f Contravariant Displacement $w\xi$ Distribution Along the Line of Symmetry for $\xi_0 = 1.0$.

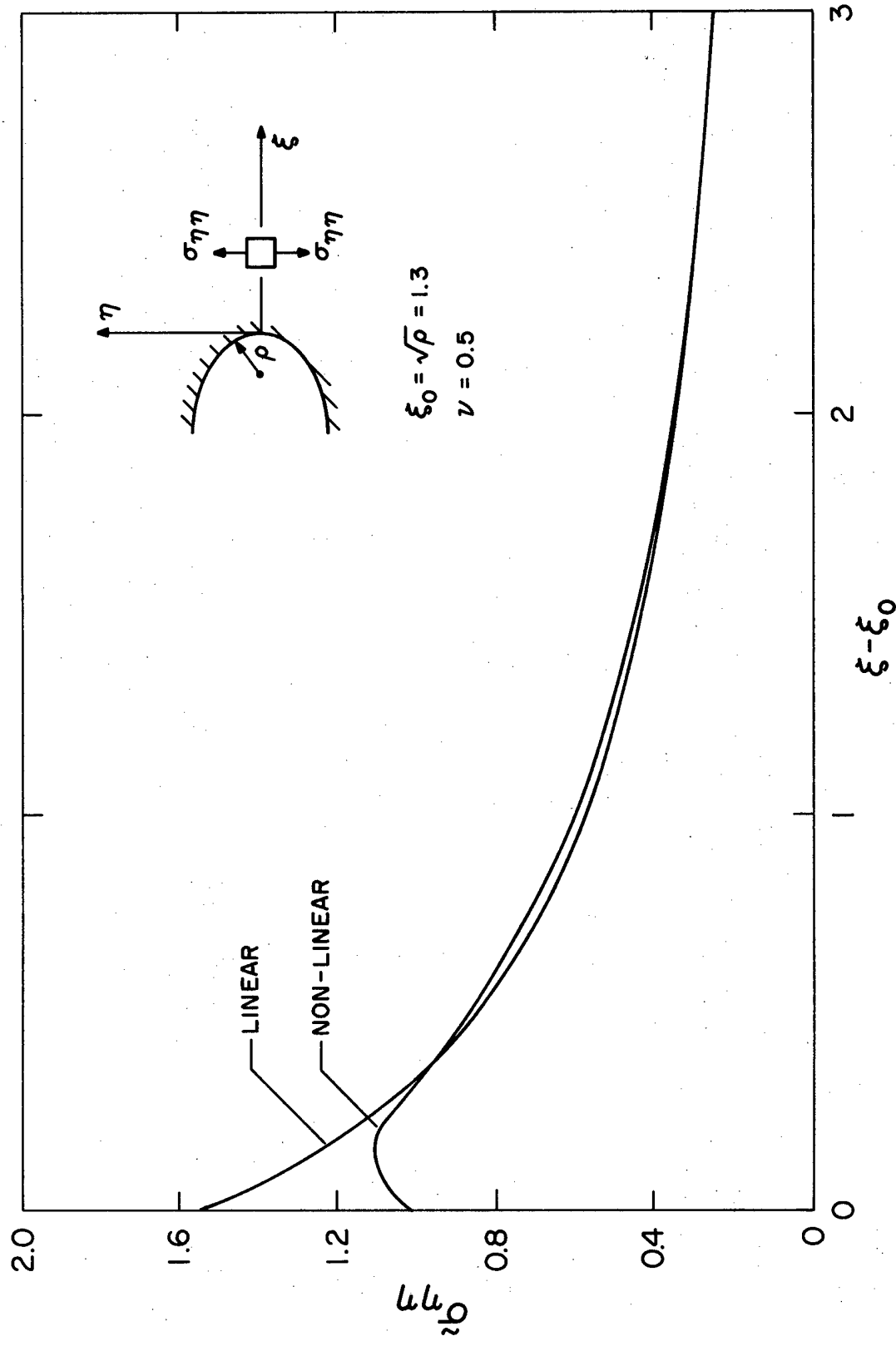


Figure 4.2a Physical Normal Stress $\tilde{\sigma}_{\eta\eta}$ Distribution Along the Line of Symmetry for $\xi_0 = 1.3$.

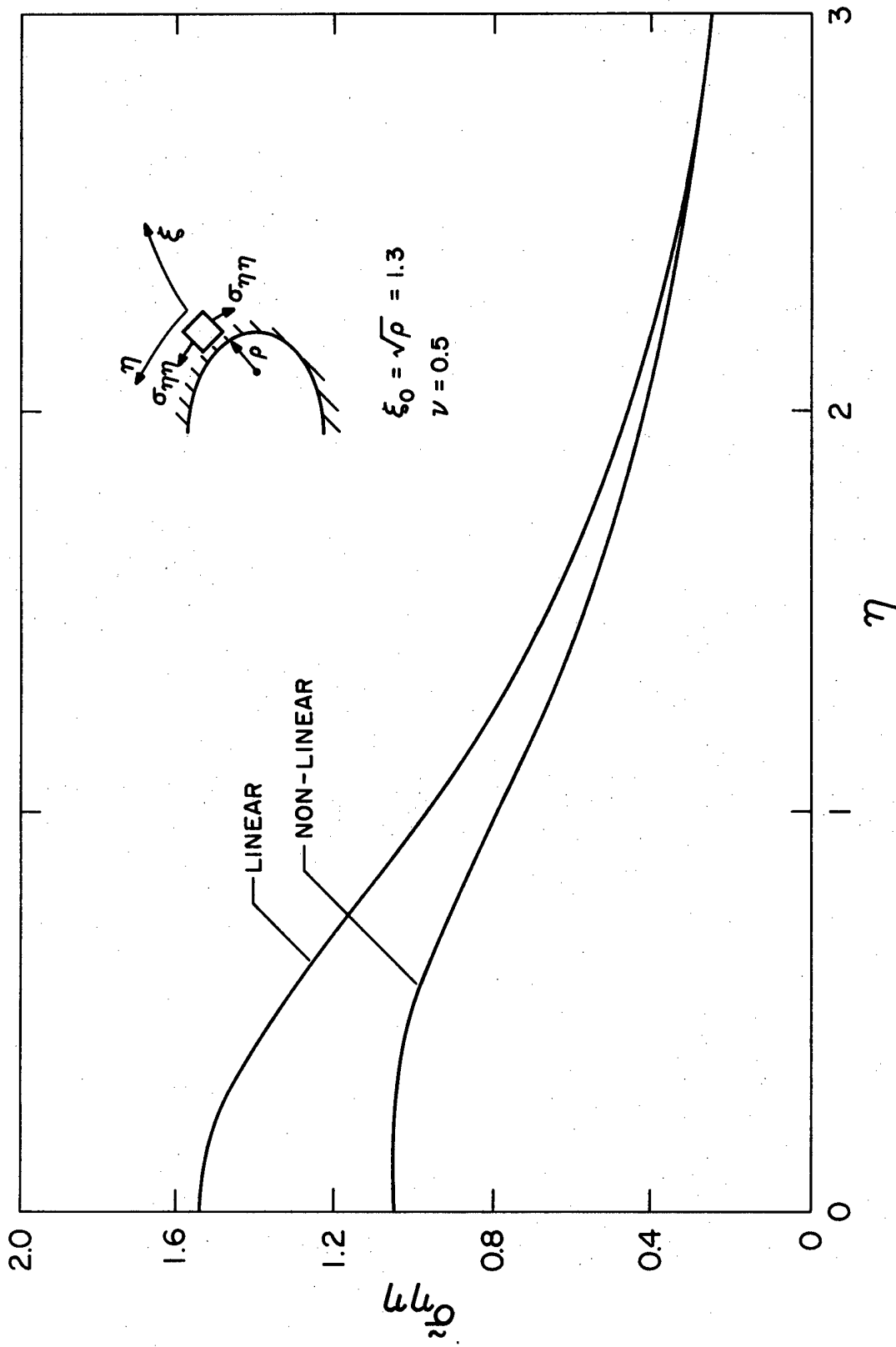


Figure 4.2b Physical Normal Stress $\sigma_{\eta\eta}$ Distribution Along the Ellipse Border for $\xi_0 = 1.3$.

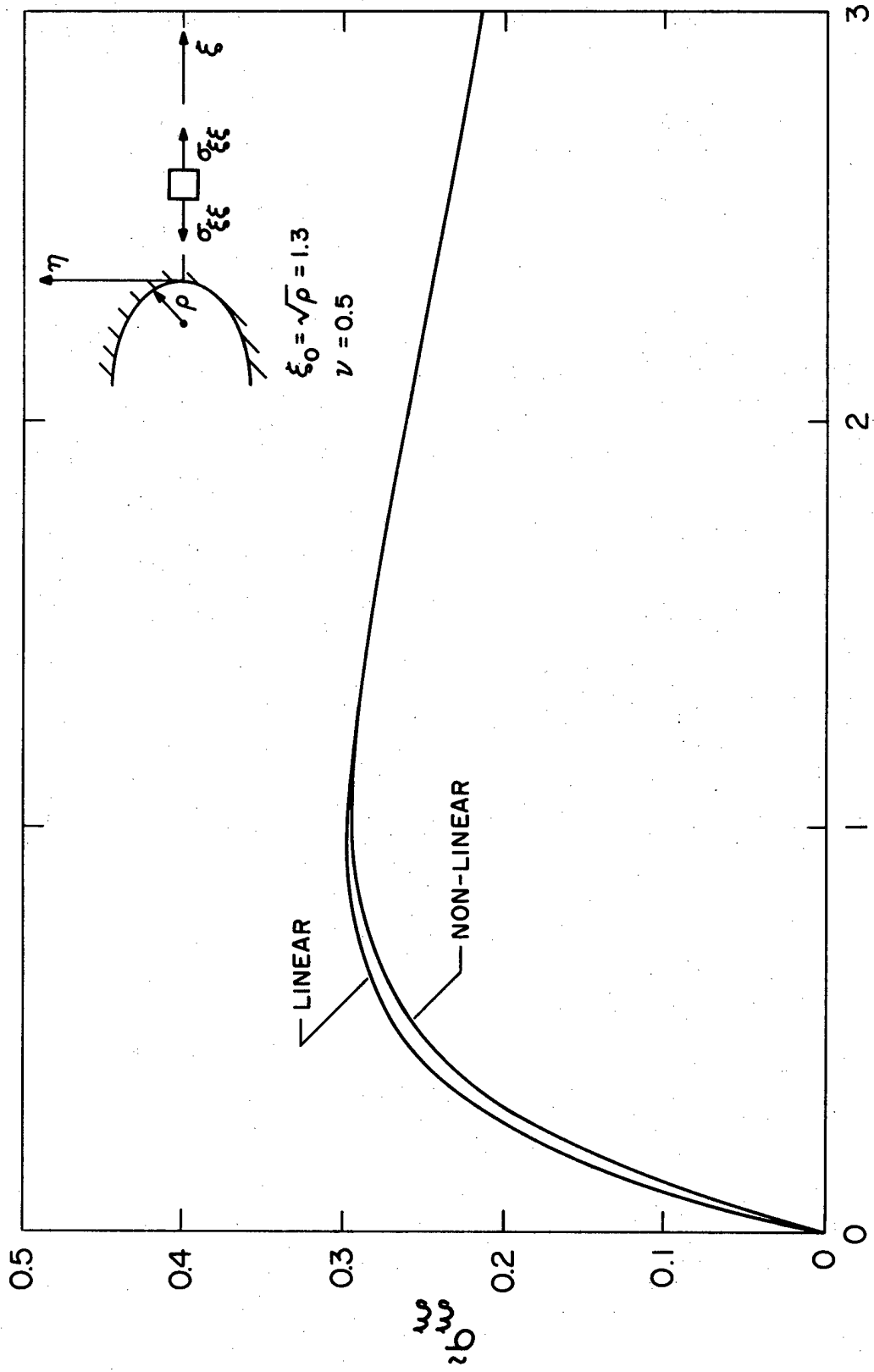


Figure 4.2c Physical Normal Stress $\sigma_{\xi\xi}$ Distribution Along the Line of Symmetry for $\xi_0 = 1.3$.

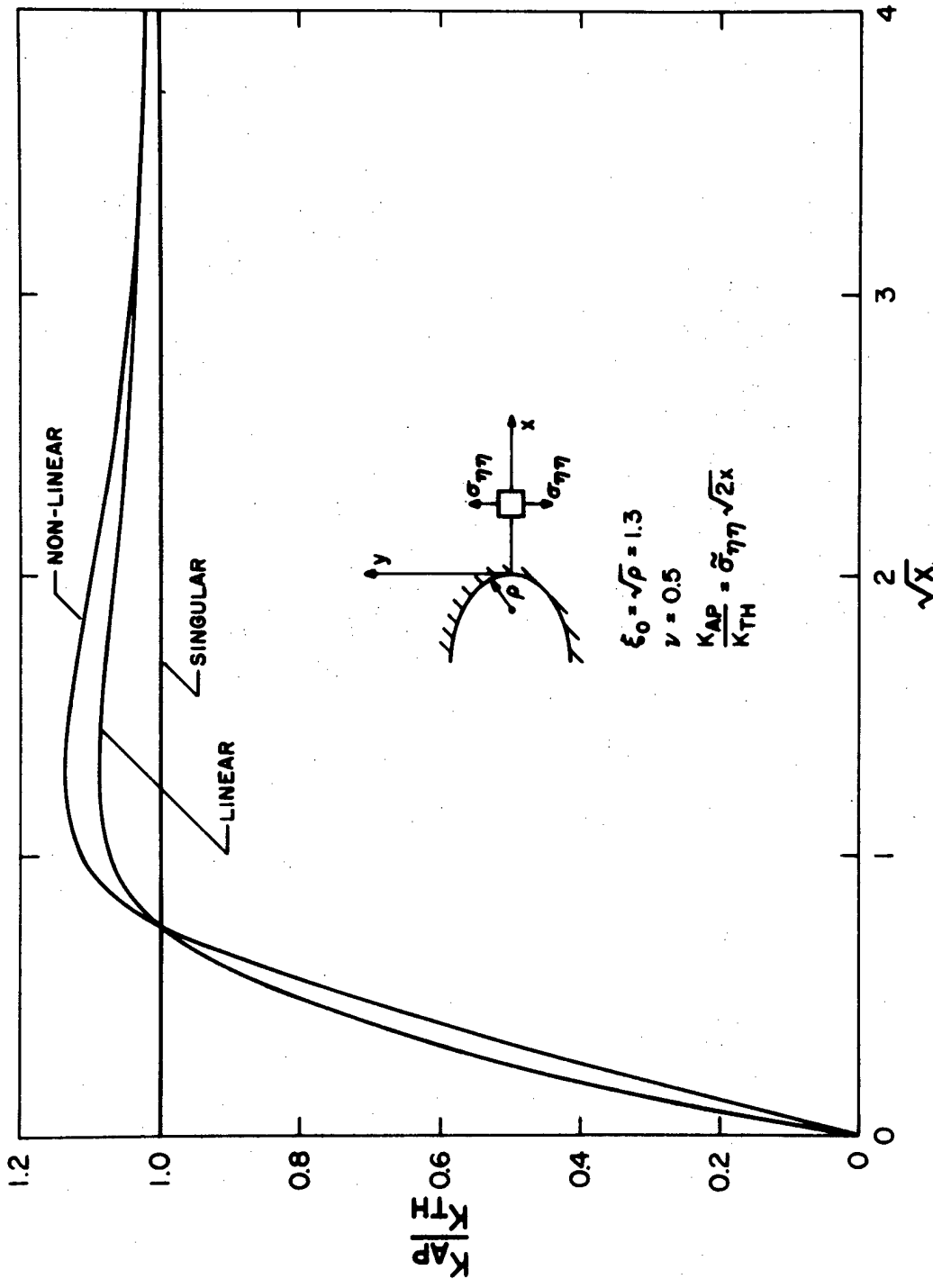


Figure 4.2d Apparent Stress Intensity Factor Distribution Along the Line of Symmetry for $\xi_0 = 1.3$.

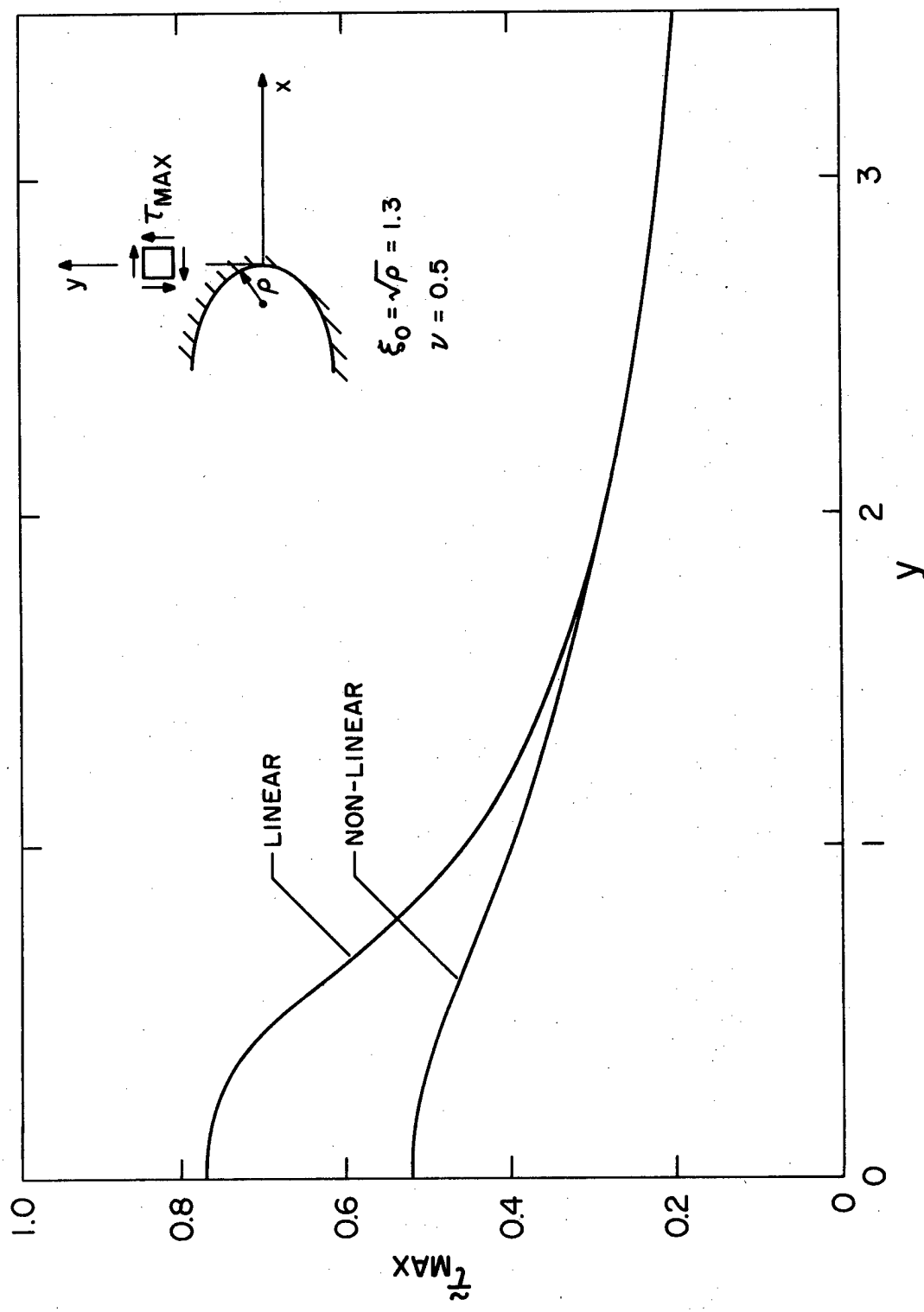


Figure 4.2e Physical Maximum In-Plane Shear Stress Distribution for $\xi_0 = 1.3$.

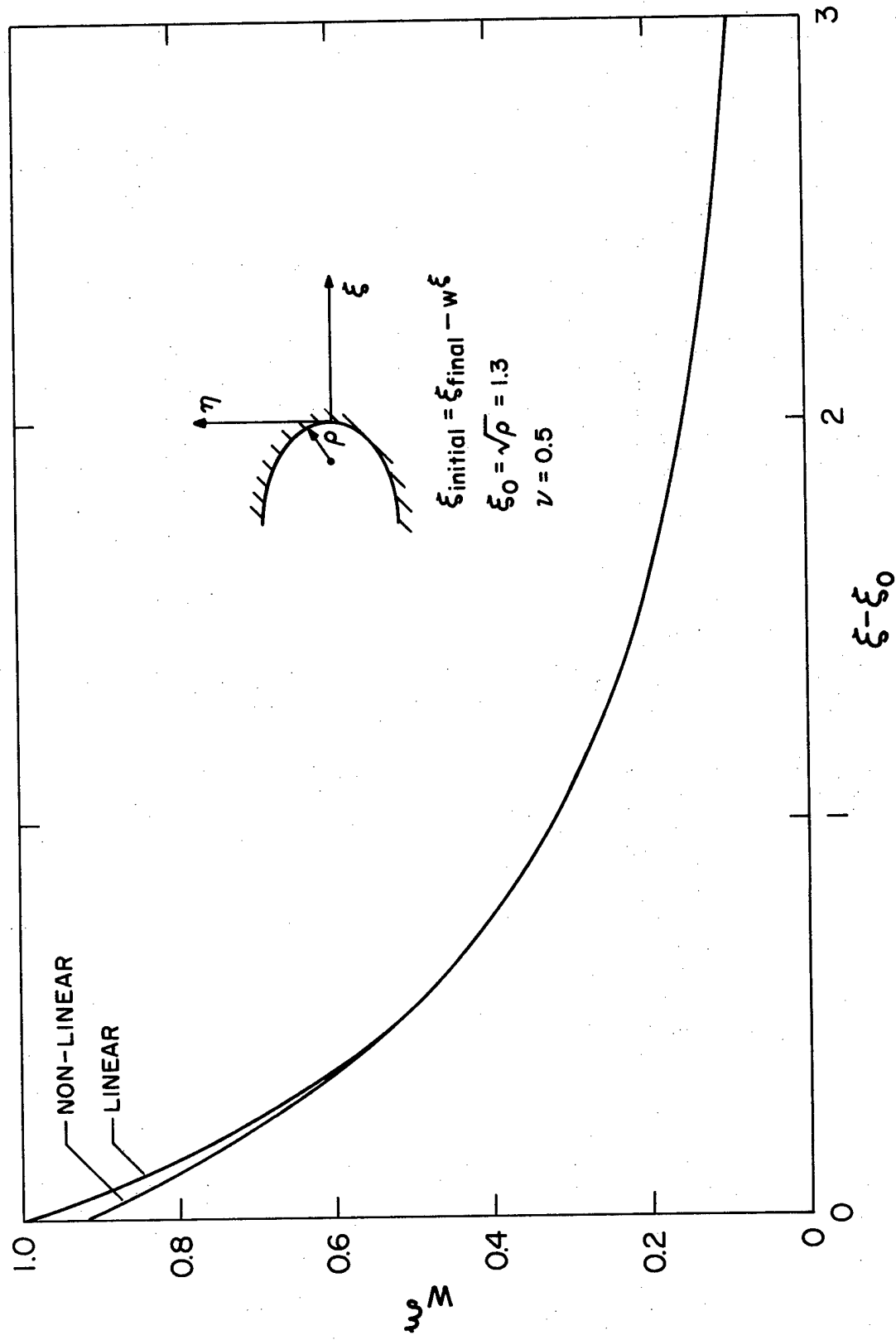


Figure 4.2f Contravariant Displacement w^ξ Distribution Along the Line of Symmetry for $\xi_0 = 1.3$.

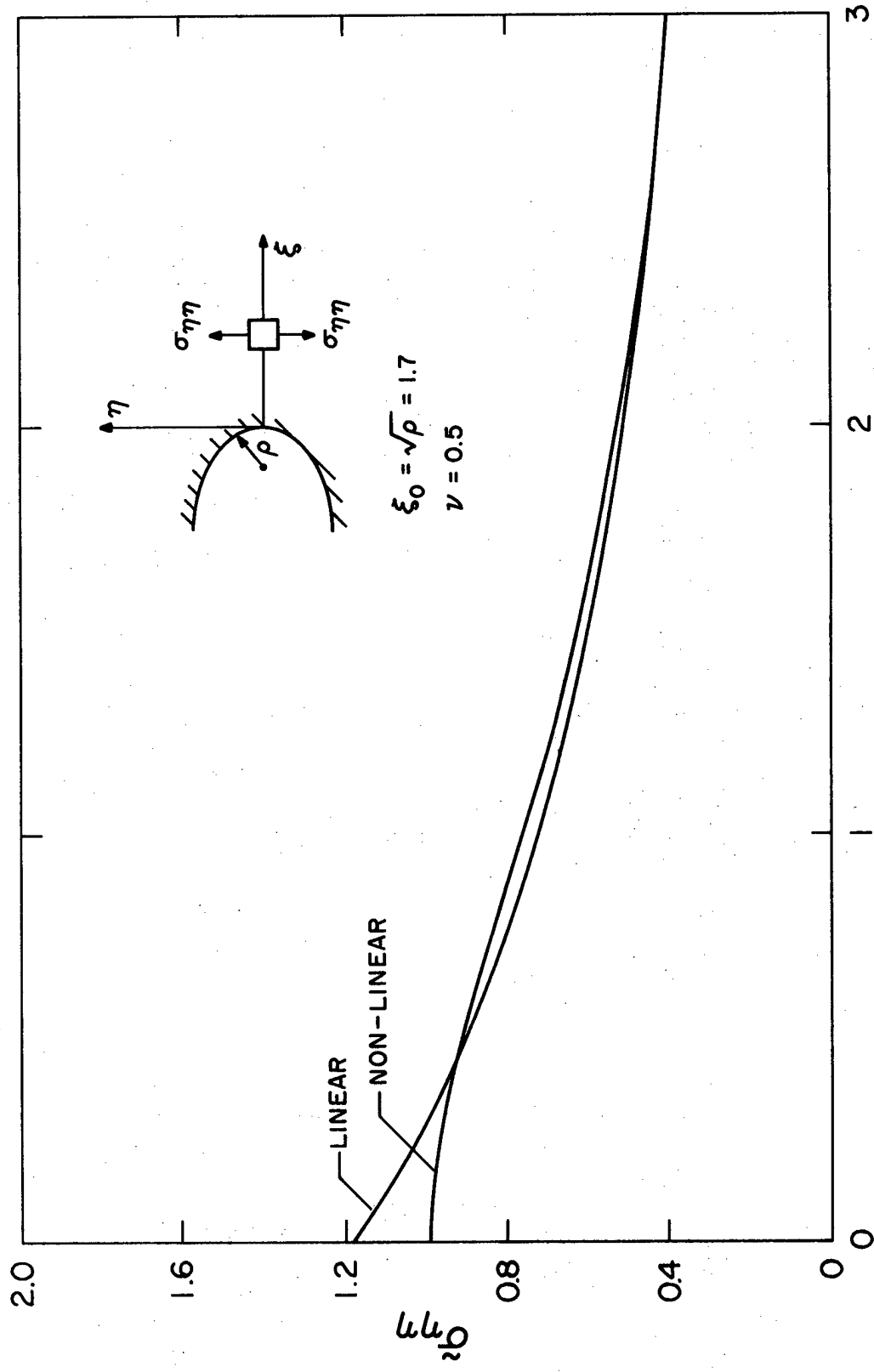


Figure 4.3a Physical Stress $\sigma_{\eta\eta}$ Distribution Along the Line of Symmetry for $\xi_0 = 1.7$.

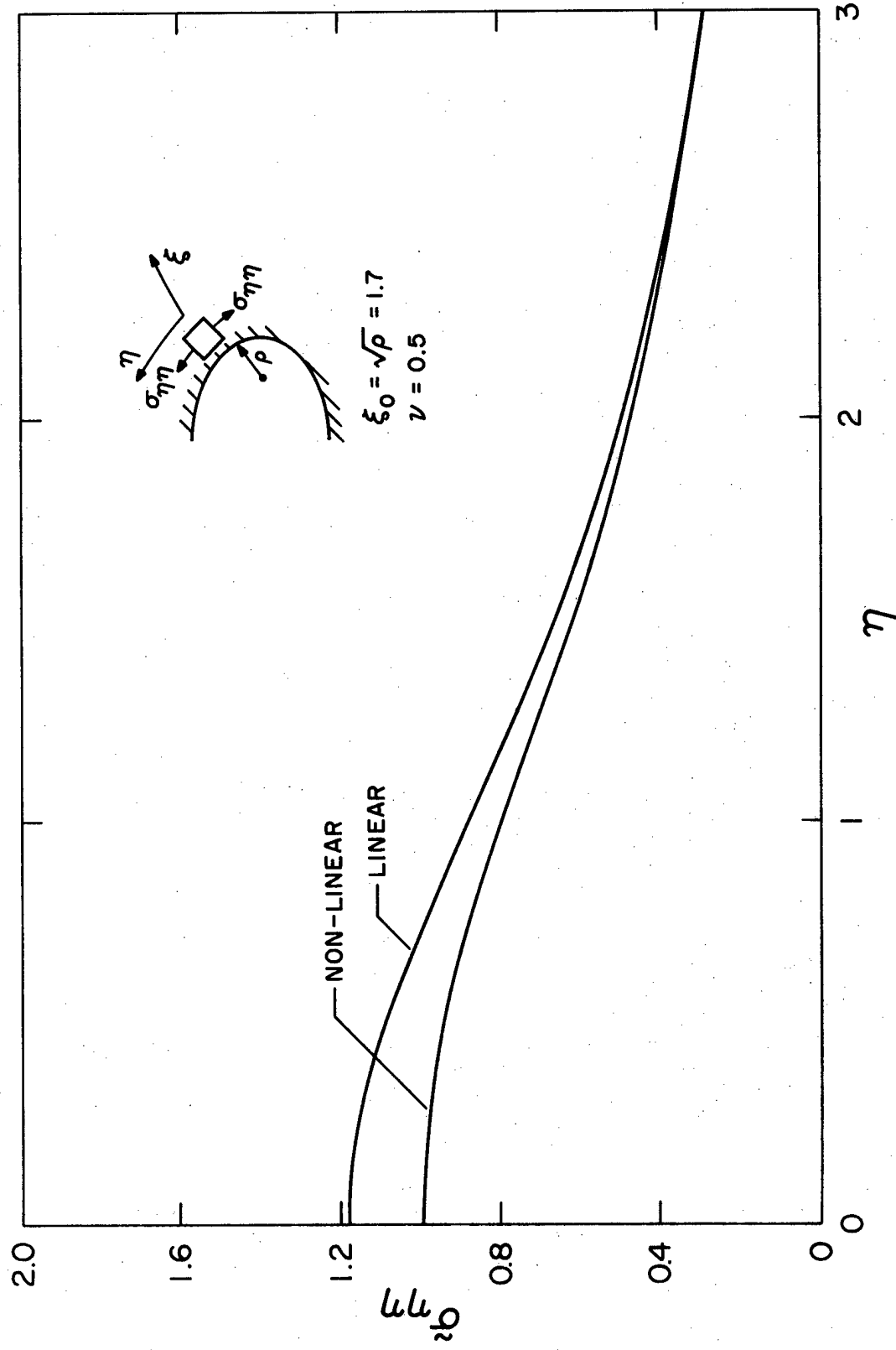


Figure 4.3b Physical Normal Stress $\tilde{\sigma}_{nn}$ Distribution Along the Ellipse Border for $\xi_0 = 1.7$.

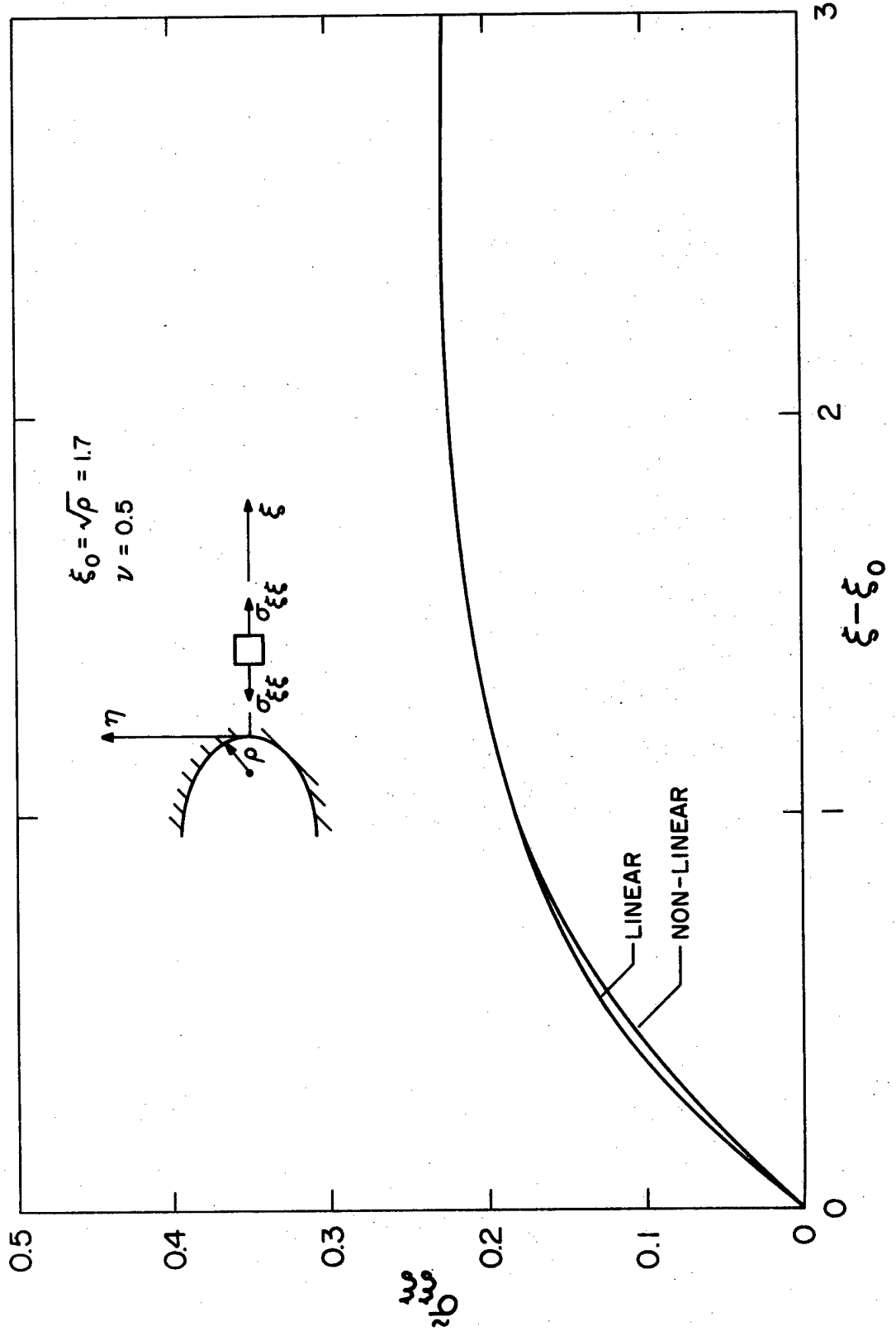


Figure 4.3c Physical Normal Stress $\sigma_{\xi\xi}$ Distribution Along the Line of Symmetry for $\xi_0 = 1.7$.

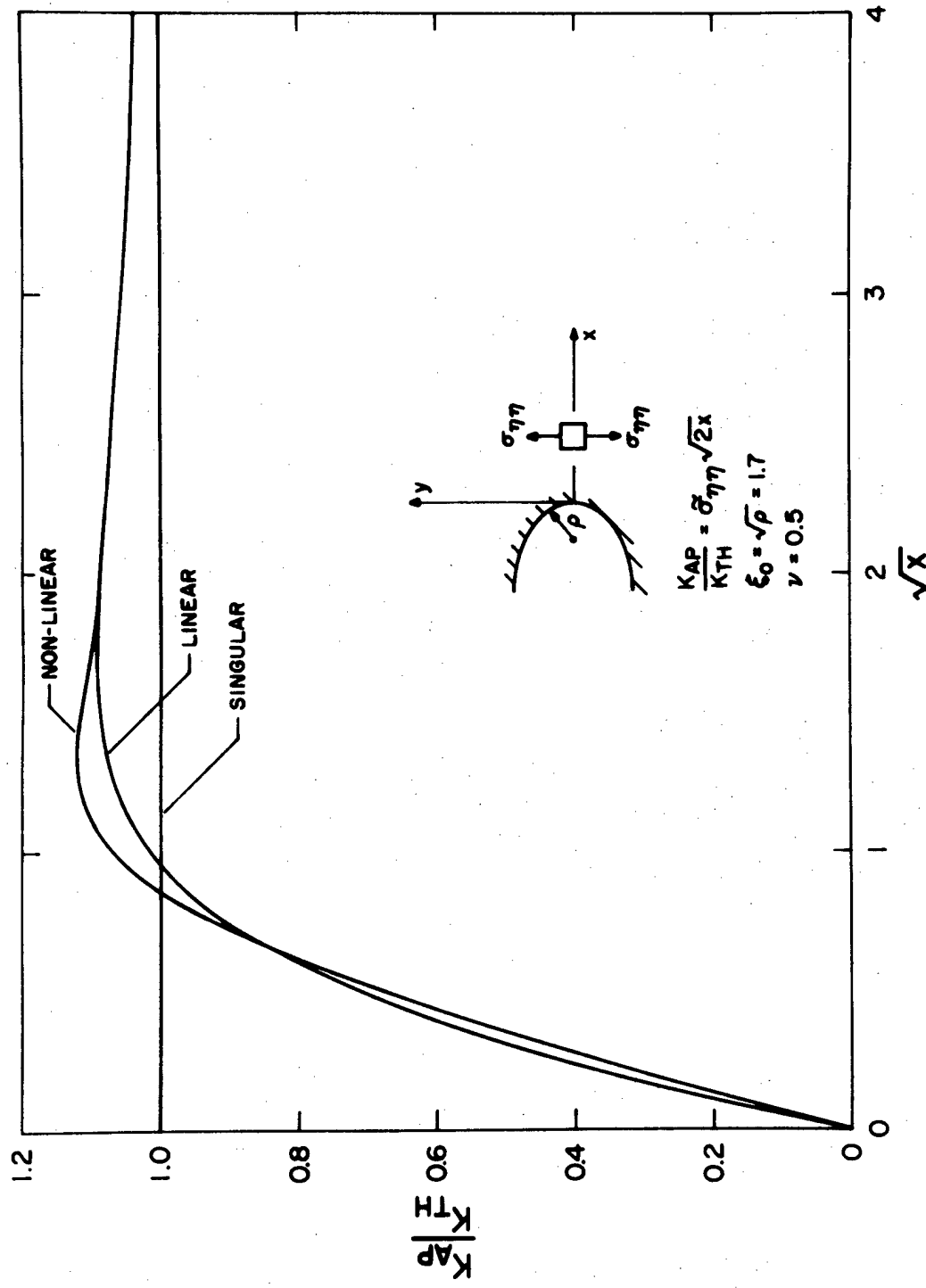


Figure 4.3d Apparent Stress Intensity Factor Distribution Along the Line of Symmetry for $\xi_0 = 1.7$.

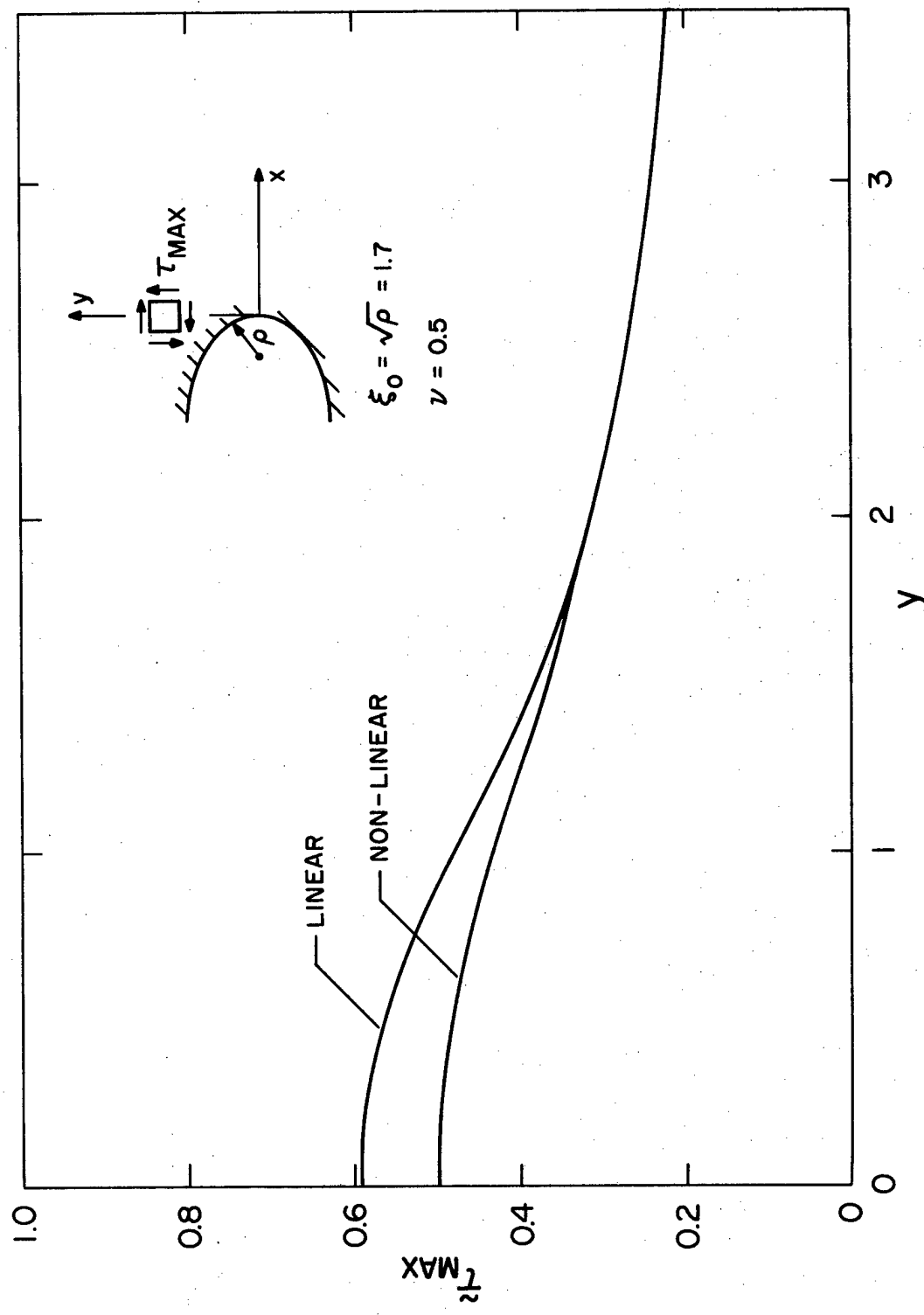


Figure 4.3e Physical Maximum In-Plane Shear Stress Distribution for $\xi_0 = 1.7$.

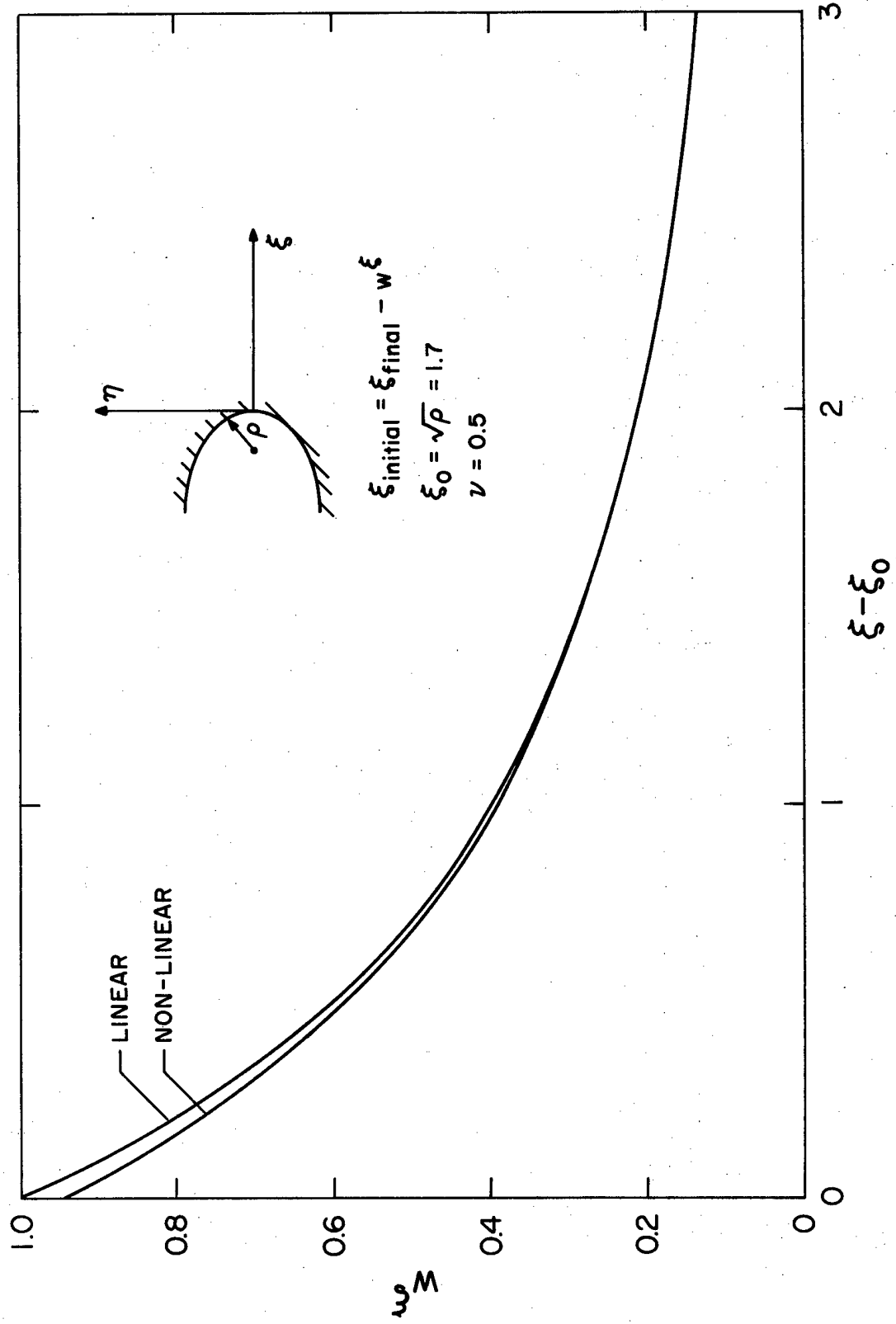


Figure 4.3f Contravariant Displacement w^ξ Distribution Along the Line of Symmetry for $\xi_0 = 1.7$.

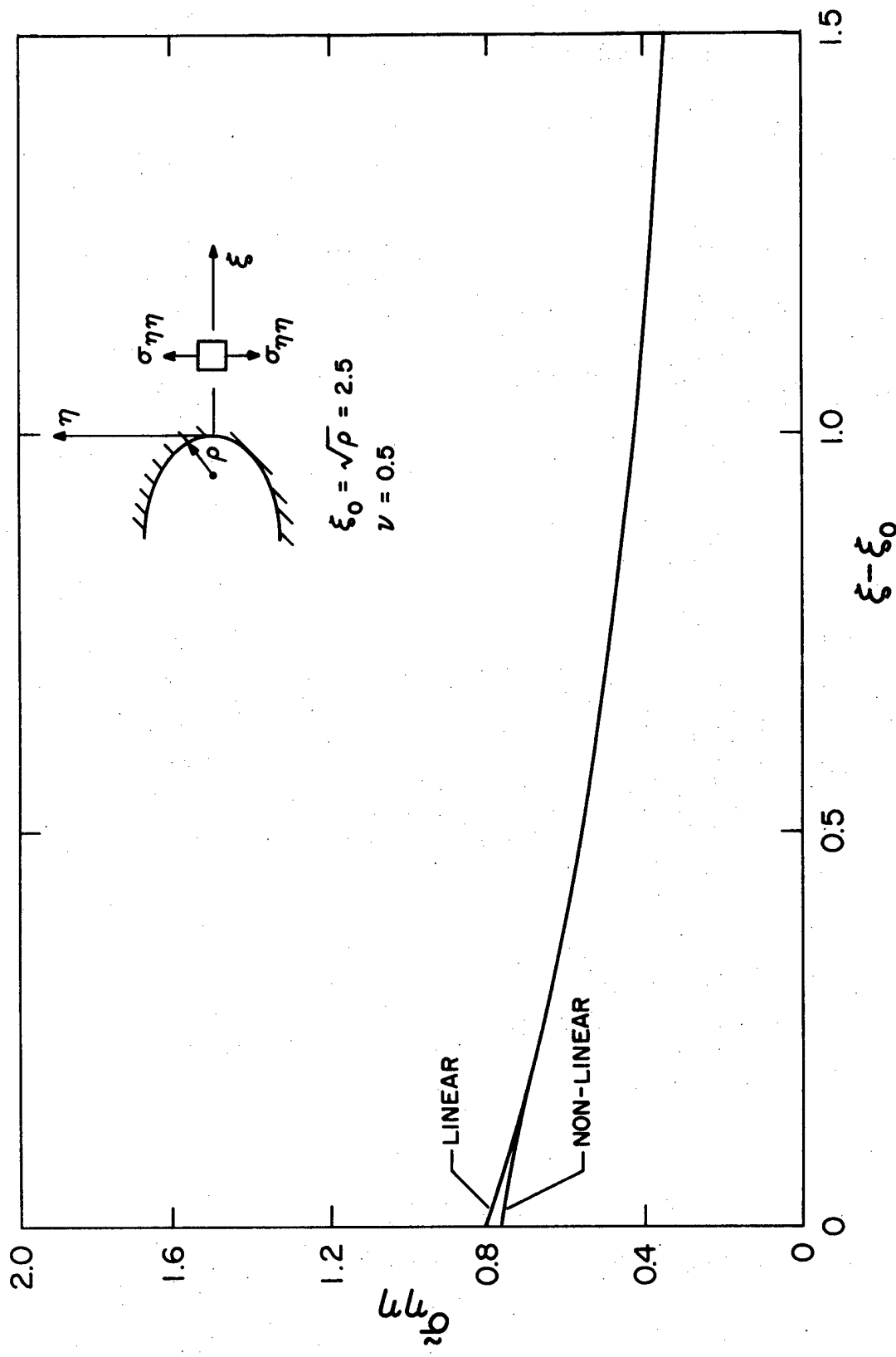


Figure 4.4a Physical Normal Stress $\tilde{\sigma}_{\eta\eta}$ Distribution Along the Line of Symmetry for $\xi_0 = 2.5$.

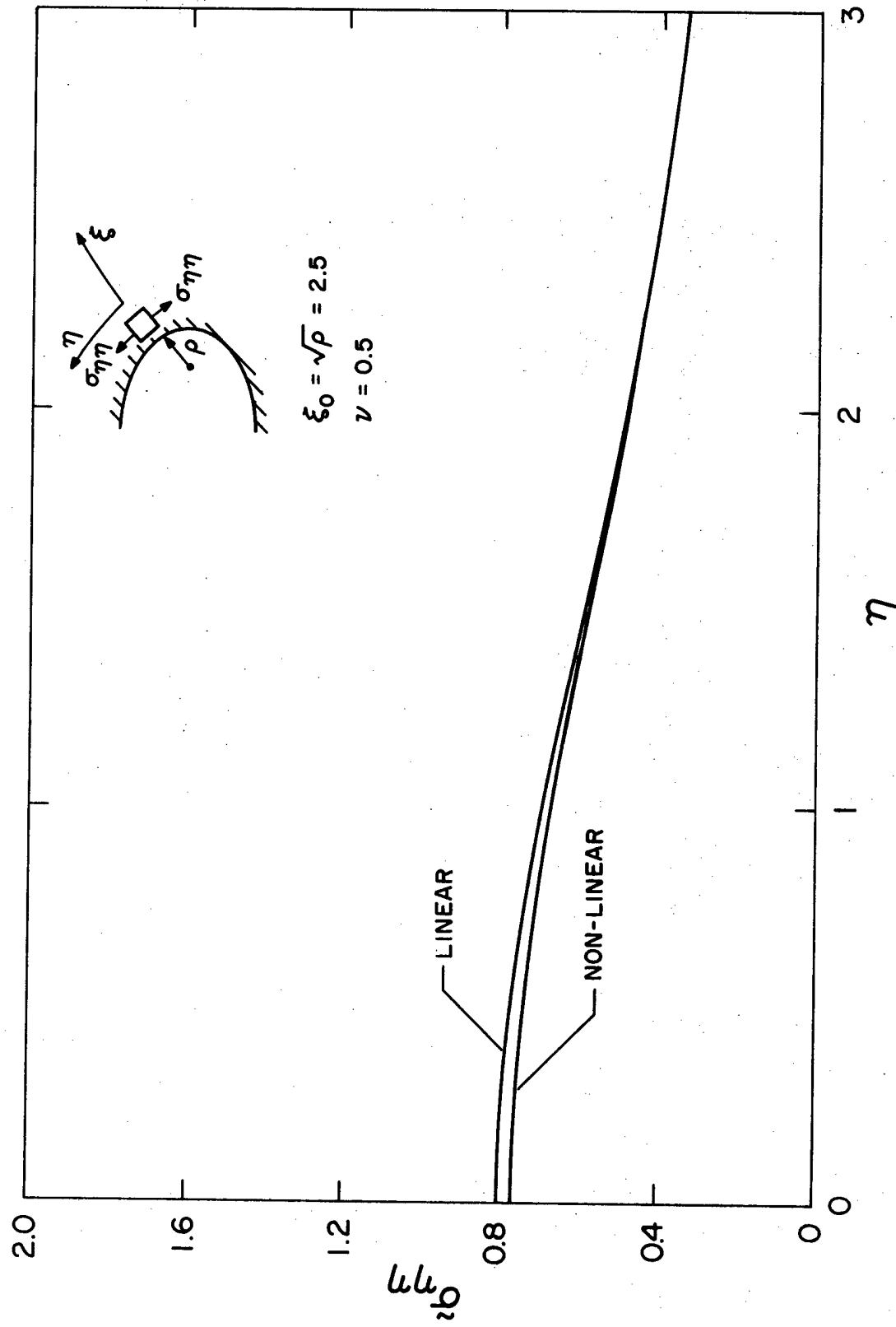


Figure 4.4b Physical Normal Stress $\tilde{\sigma}_{\eta\eta}$ Distribution Along the Ellipse Border for $\xi_0 = 2.5$.

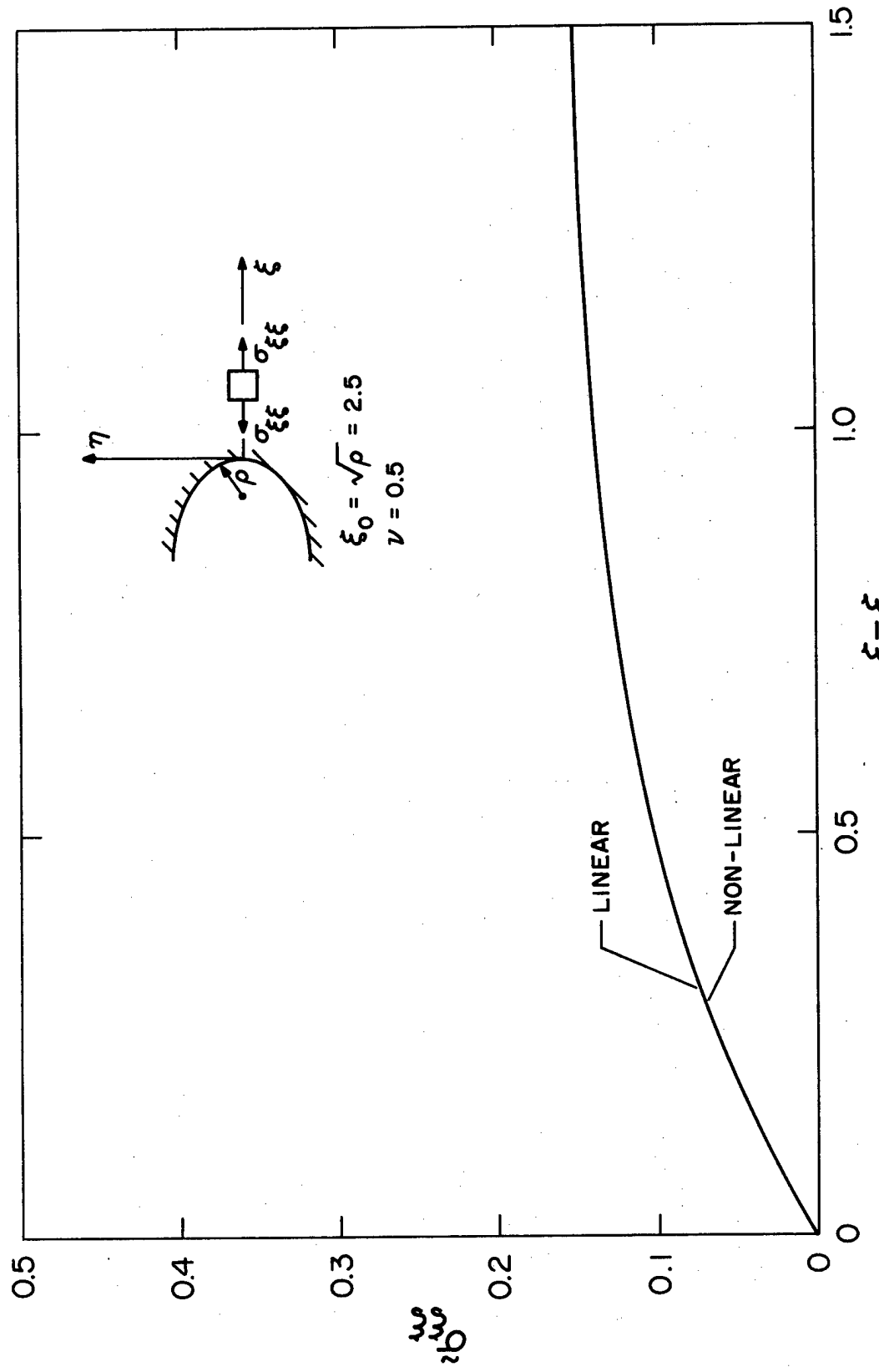


Figure 4.4c Physical Normal Stress $\sigma_{\xi\xi}$ Distribution Along the Line of Symmetry for $\xi_0 = 2.5$.

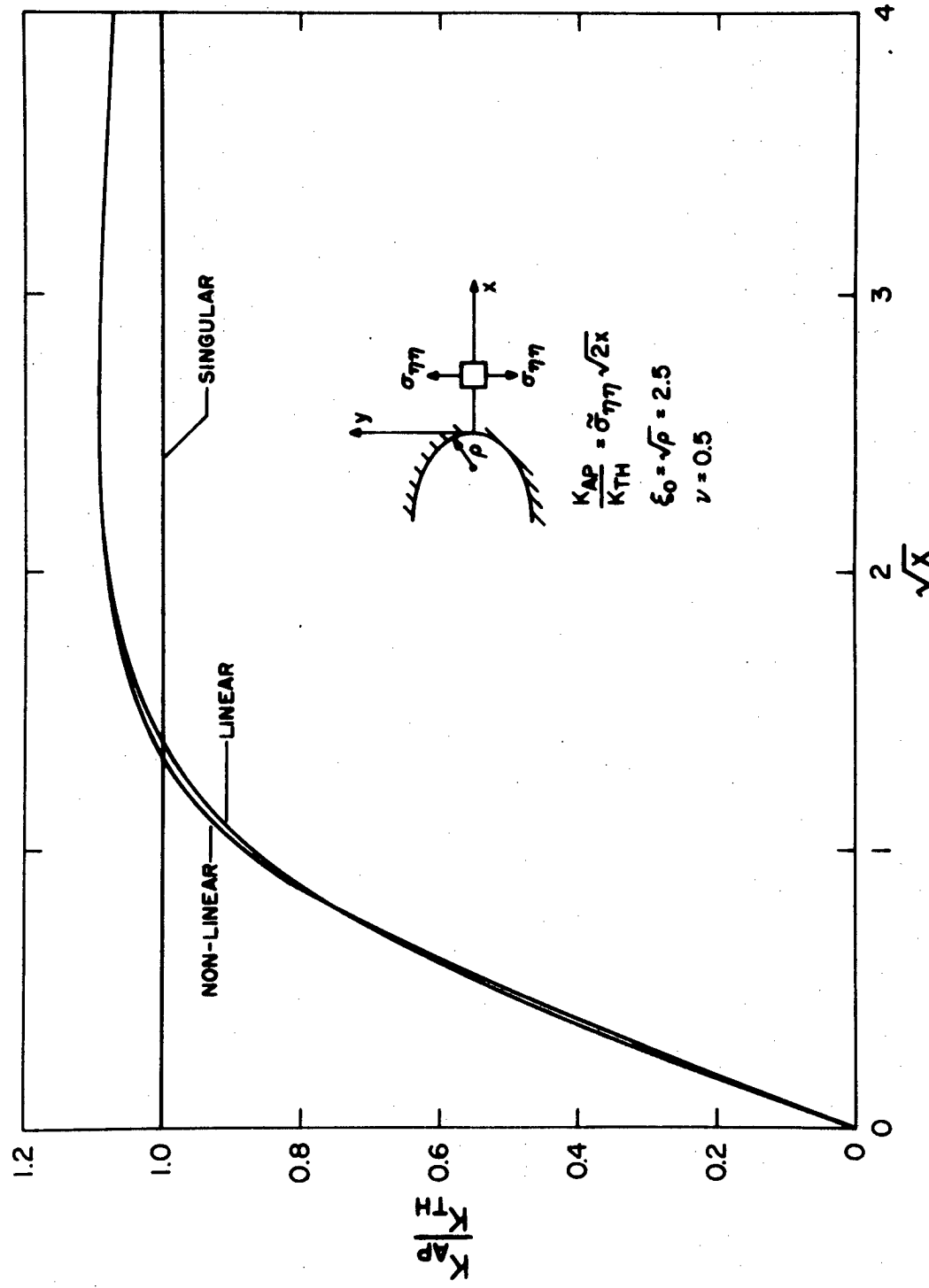


Figure 4.4d Apparent Stress Intensity Factor Distribution Along the Line of Symmetry for $\xi_0 = 2.5$.

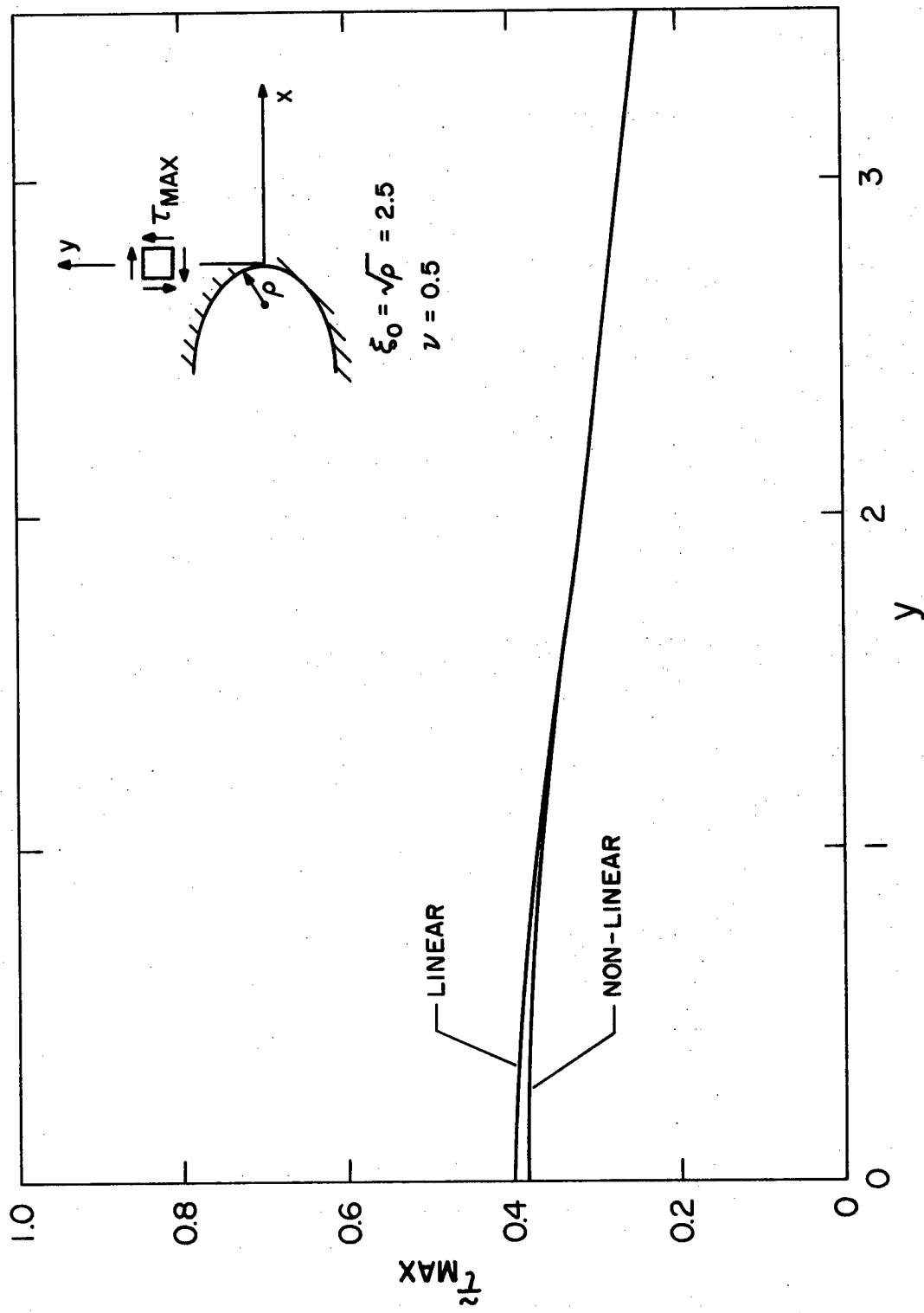


Figure 4.4e Physical Maximum In-Plane Shear Stress Distribution for $\xi_0 = 2.5$.

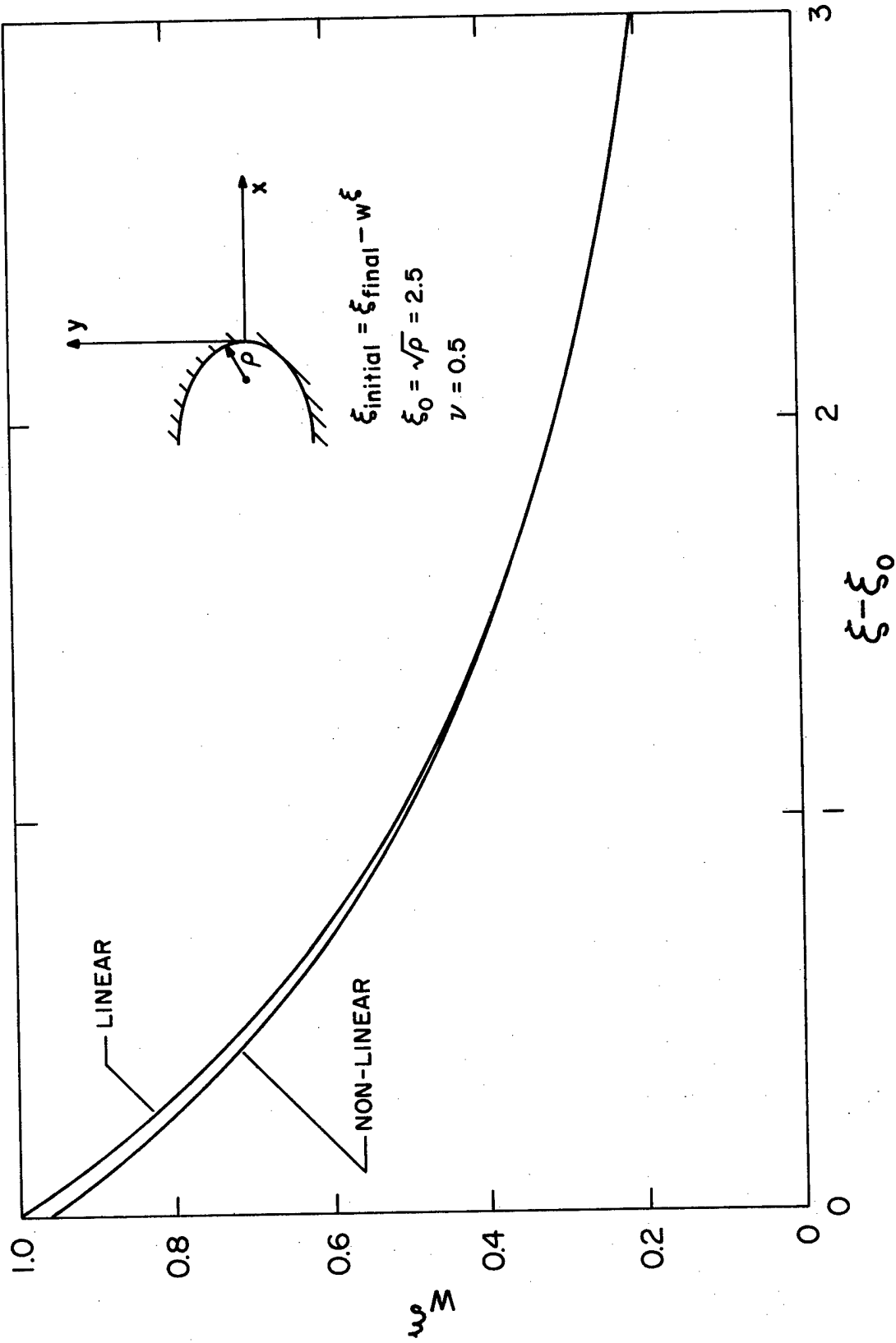


Figure 4.4f Contravariant Displacement $w\xi$ Distribution Along the Line of Symmetry for $\xi_0 = 2.5$.

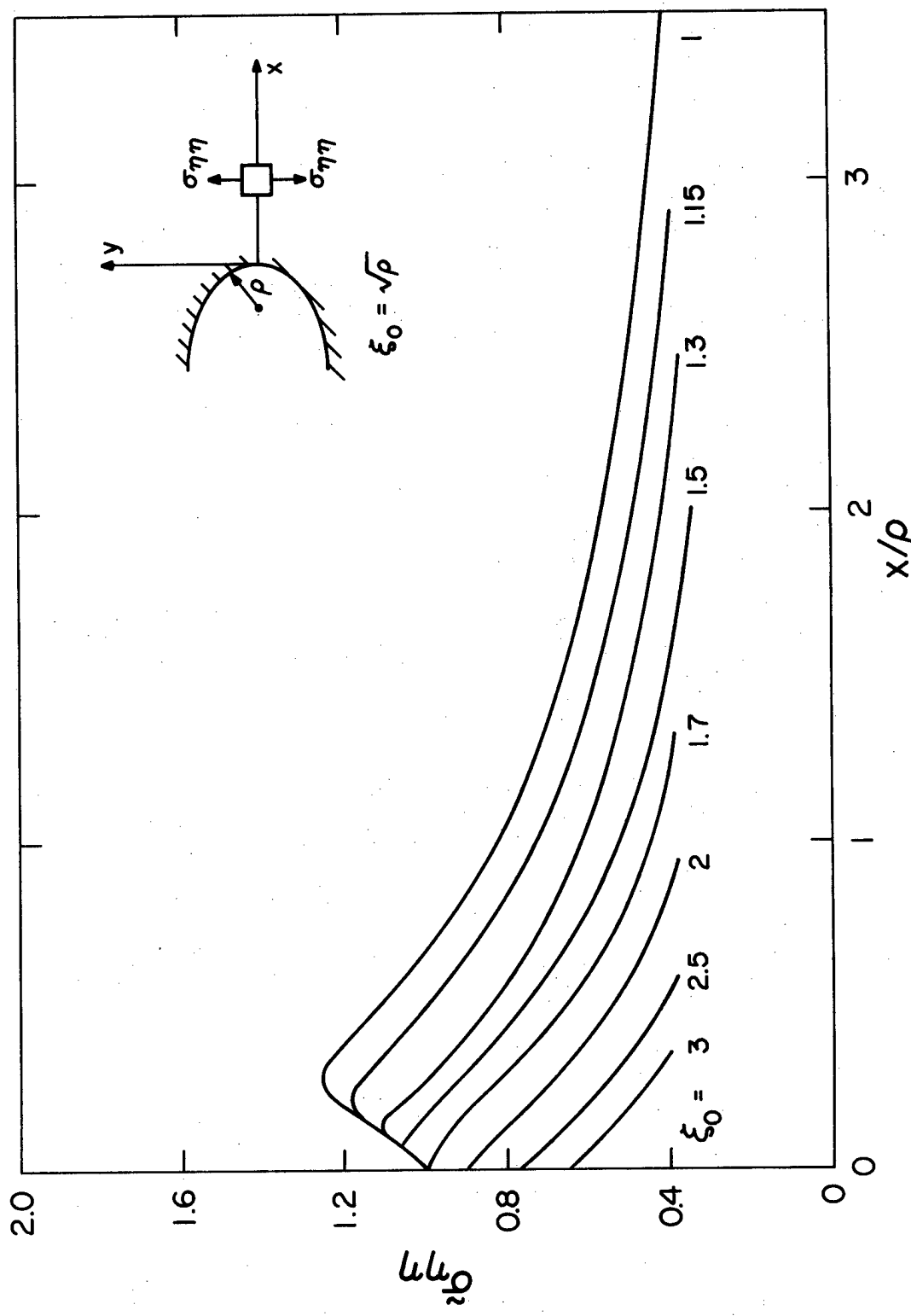


Figure 4.5 Physical Normal Stress $\tilde{\sigma}_{nn}$ Distribution Along the Line of Symmetry for Various Ellipse Root Radii.

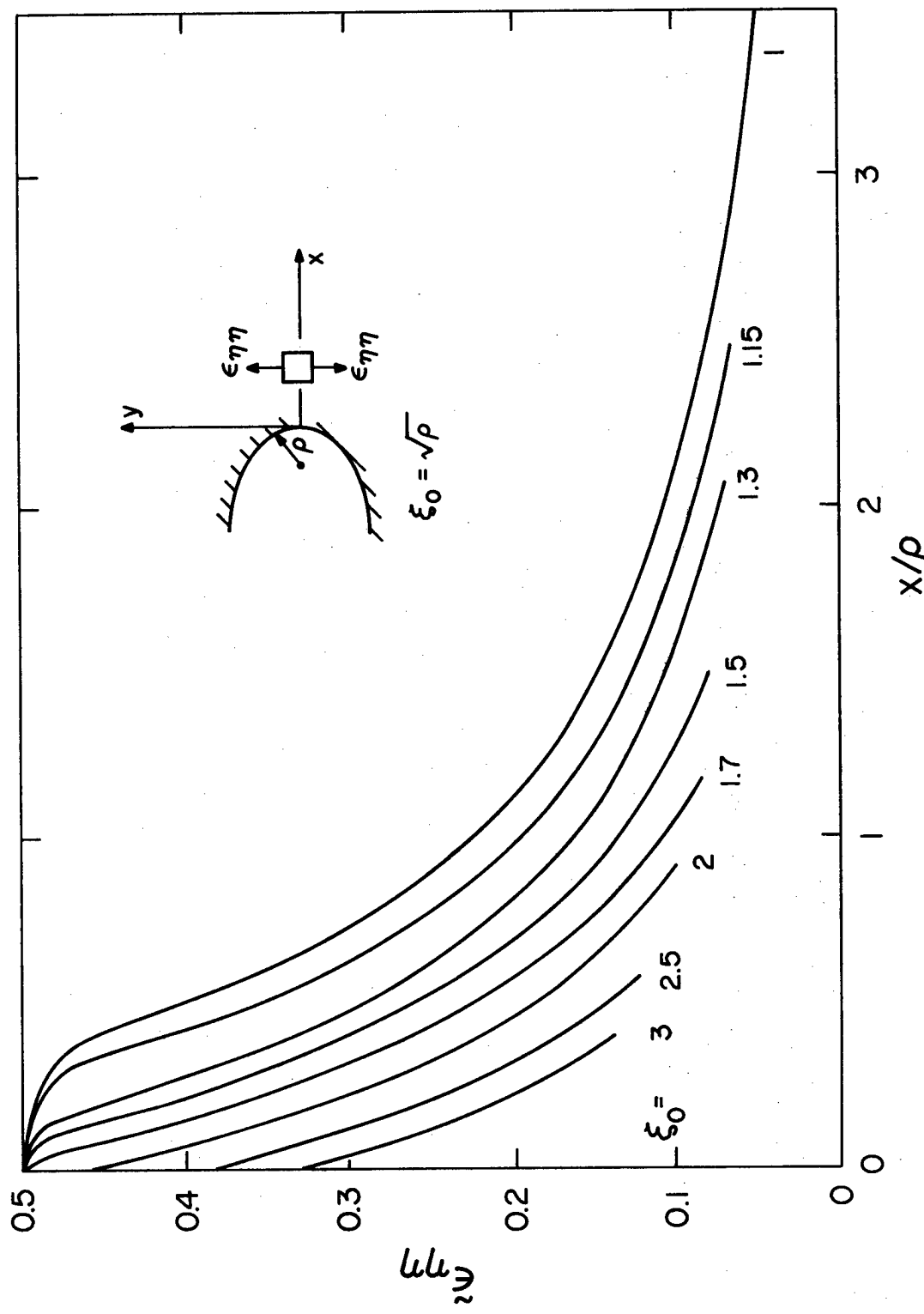


Figure 4.6 Physical Normal Strain $\tilde{\epsilon}_{\eta\eta}$ Distribution Along the Line of Symmetry for Various Ellipse Root Radii.

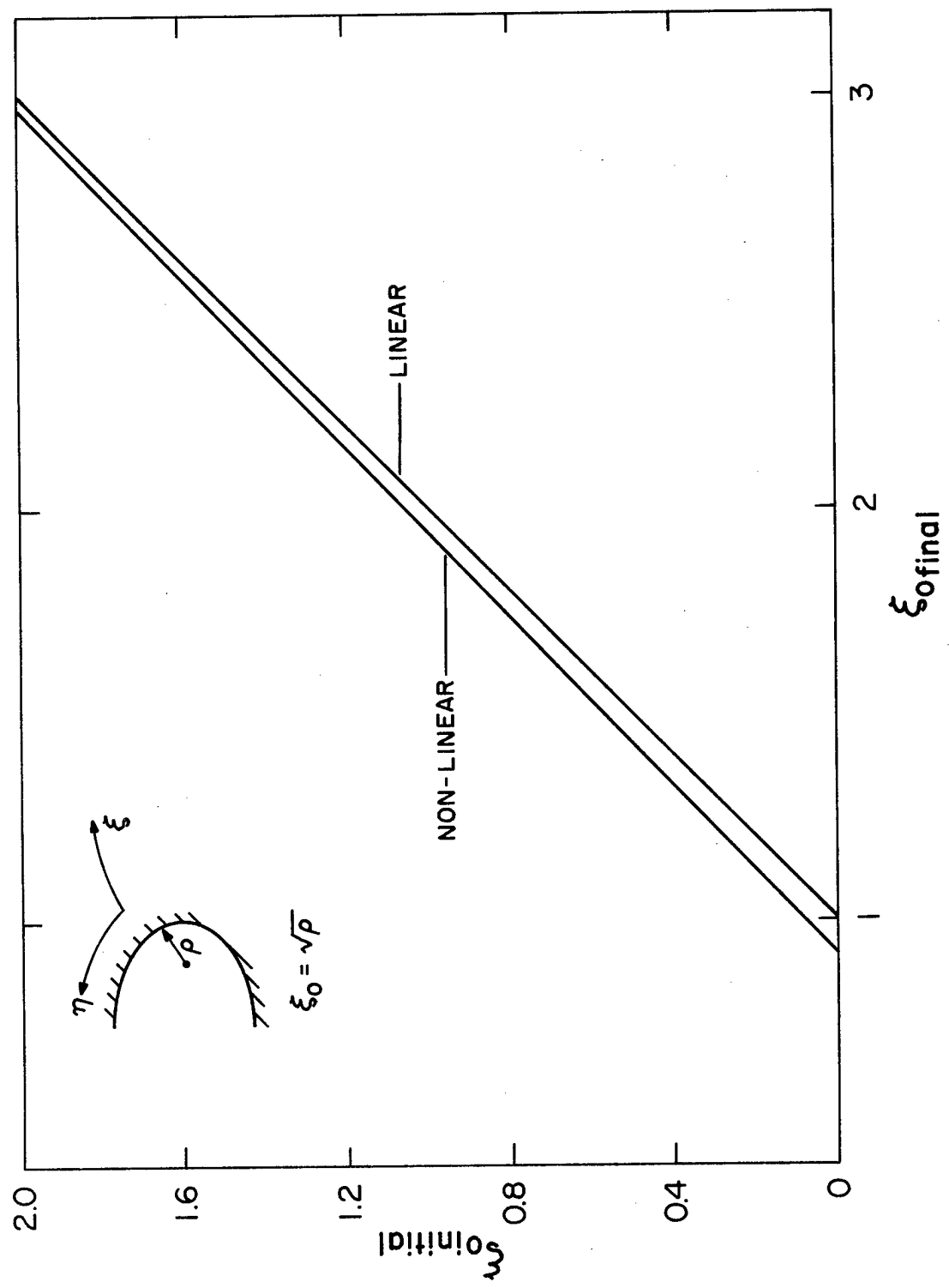


Figure 4.7 Variation of Initial Root Radius with Respect to Final Ellipse Root Radius.

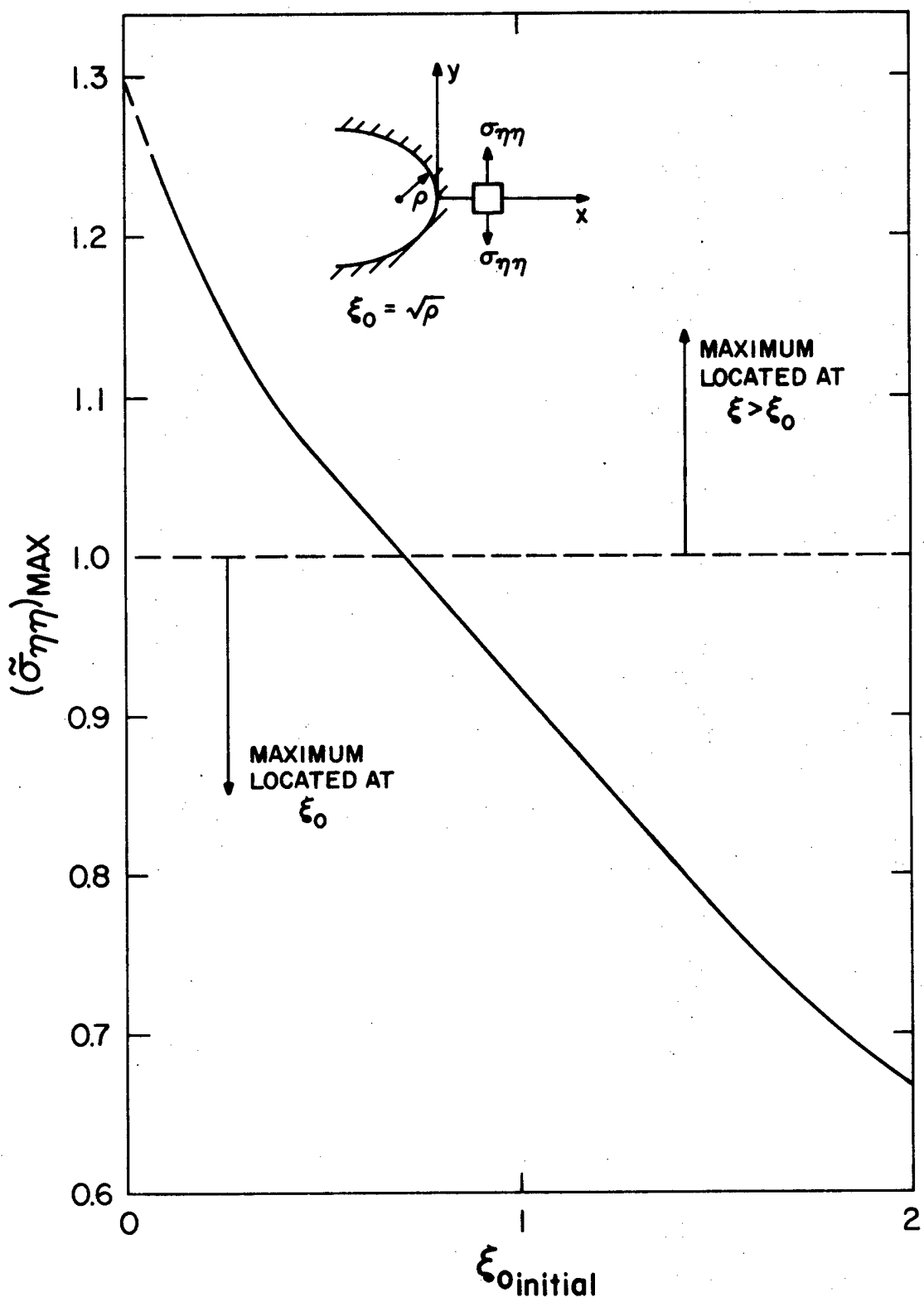


Figure 4.8 Variation of Physical Normal Stress $\tilde{\sigma}_{\eta\eta}$ Maximum with Respect to Initial Root Radius.

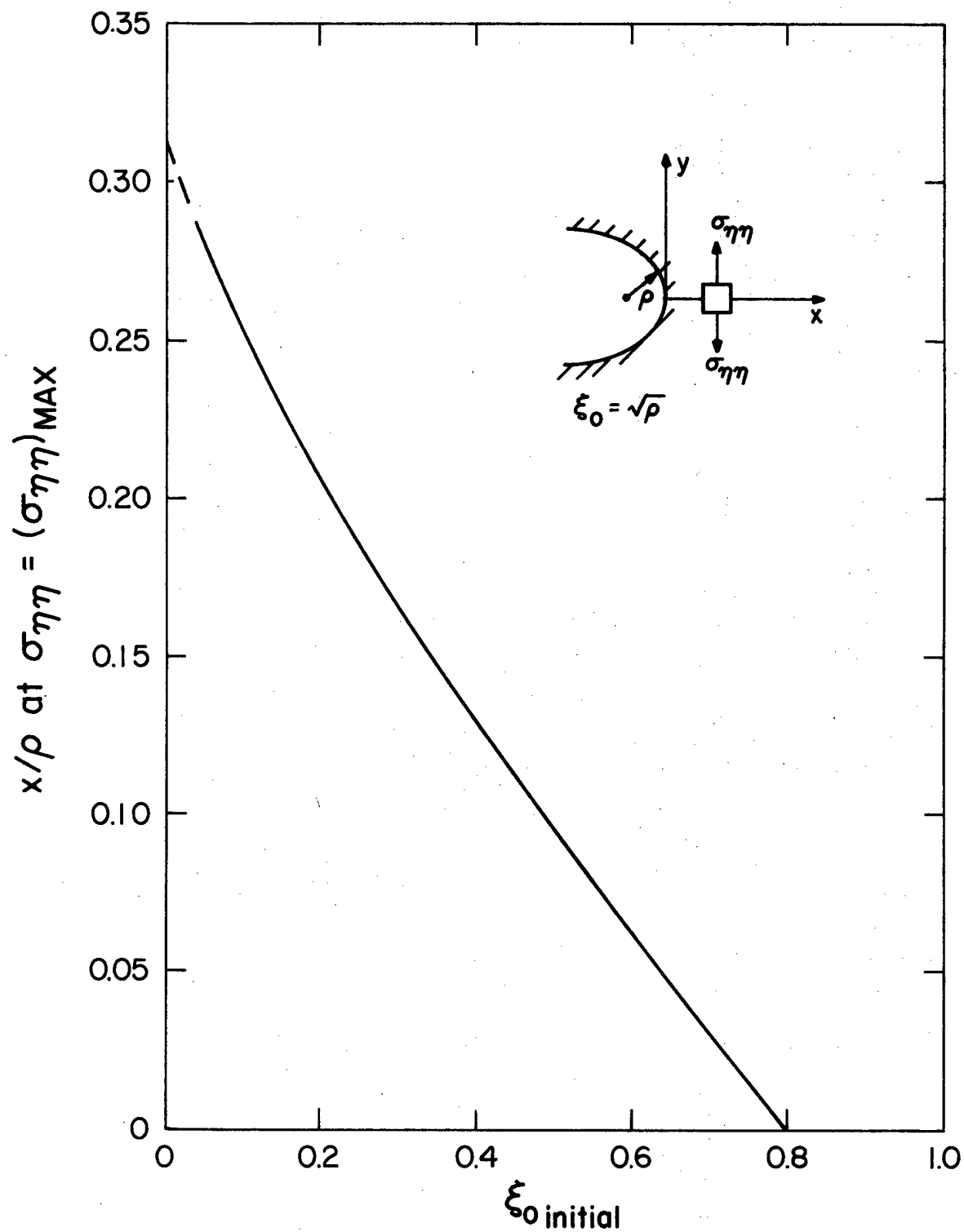


Figure 4.9 Variation of Location of Physical Normal Stress $\tilde{\sigma}_{\eta\eta}$ Maximum with Respect to Initial Root Radius.

DISTRIBUTION LIST

(Virginia Polytechnic Institute and State University)

Commanding General
U.S. Army Natick Laboratories
ATTN: Mr. E. W. Ross, Jr.
Natick, Mass. 01762

Lehigh University
ATTN: Dr. G. C. Sih
Bethlehem, Pa. 18015

Commanding Officer
Frankford Arsenal
ATTN: Mr. P. D. Flynn
Bridge & Tacony Streets
Philadelphia, Pa. 19137

Battelle Memorial Institute
ATTN: Dr. G. T. Hahn
505 King Avenue
Columbus, Ohio 43201

General Electric Company
ATTN: A. J. Brothers, Materials and
Processes Lab.
Schenectady, New York 12010

United States Steel Corporation
ATTN: Mr. S. T. Rolfe, Applied
Research Lab.
Monroeville, Pa. 15146

University of Illinois
ATTN: Mr. H. T. Corten, Department of
Theoretical & Applied Mechanics
212 Talbot Lab.
Urbana, Illinois 61803

Westinghouse Electric Company
ATTN: Mr. E. T. Wessel, R&D Center
Pittsburgh, Pa. 15200

Carnegie Institute of Technology
ATTN: Dr. J. L. Swedlow
Schenley Park
Pittsburgh, Pa. 15213

Rensselaer Polytechnic Institute
ATTN: Prof. J. C. Janz, Chairman of
Chemistry Department
Troy, New York 12180

Syracuse University
ATTN: Dr. H. W. Liu
Syracuse, New York 13210

Commanding Officer
U.S. Army Aviation Material
Laboratories
ATTN: Mr. C. D. Roach
Fort Eustis, Virginia 23604

University of California
ATTN: W. W. Gerberich, Department of
Mineral Technology
Berkeley, Calif. 94700

University of Illinois
ATTN: Prof. D. Drucker, Dean of School
of Engineering
Champaign, Illinois 61820

University of Washington
ATTN: Prof. A. Kobayashi, Department
of Mechanical Engineering
Seattle, Washington 98105

Technical Director
U.S. Army Materials & Mechanics
Research Center
ATTN: Mr. J. Bluhm
Watertown, Mass. 02172

Brown University
ATTN: Dr. J. R. Rice
Providence, Rhode Island 02912

University of Connecticut
ATTN: Dr. A. J. McEvily, Head
Dept. of Metallurgy U-139
Dr. N. D. Greene, Metallurgy
Dept.
Storrs, Conn. 06268

No. of
Copies

Office of the Director of Defense Research & Engineering
ATTN: Assistant Director of Materials
The Pentagon
Washington, D. C. 20315

1

Commander
Defense Documentation Center
Cameron Station, Bldg. 5
5010 Duke Street
Alexandria, Virginia 22314

2

Commanding General
U.S. Army Material Command
ATTN: AMCRD
AMCRD-R, Mr. H. Cohen
AMCRD-W
AMCRD-TC

1
1
1
1

Bldg. T-7
Washington, D. C. 20315

Commanding General
U.S. Army Weapons Command
ATTN: AMSWE-LCD
AMSWE-PPR
AMSWE-RDA
AMSWE-RDR

1
1
1
1

Rock Island, Illinois 61201

Commanding General
U.S. Army Tank-Automotive Command
ATTN: AMSTA-BSL
AMSTA-BMM

1
1

Warren, Michigan 48090

Commanding General
U.S. Army Munitions Command
ATTN: AMSMU-SS-EC

1

Dover, New Jersey 07801

Commanding Officer
Army Research Office
Office Chief Research & Development
ATTN: Physical Sciences Division
3045 Columbia Pike
Arlington, Virginia 22207

2

Commanding Officer
U.S. Army Research Office (Durham)
Box CM, Duke Station
Durham, North Carolina

6

Commanding Officer
Rock Island Arsenal
ATTN: SWERI-RDD
Rock Island, Illinois 61202

1

No. of
Copies

Director Naval Research Laboratory ATTN: Dr. J. M. Krafft, Code 8430 Mr. W. S. Pellini, Code 6300 Washington, D. C. 20390	1 1
Dr. G. R. Irwin University of Maryland Department of Mechanical Engineering College Park, Maryland 20742	1
Commander Wright-Patterson Air Force Base ATTN: AFML(MAAA) Hq., Aeronautical Systems Division Ohio 45433	5
Commander George C. Marshall Space Flight Center ATTN: M-S&M-M M-F&AEM, Bldg. 4720 Huntsville, Alabama 35809	1 1
NASA Scientific and Technical Information Facility ATTN: Acquisitions Branch P. O. Box 33 College Park, Maryland 20740	1
Mr. Robert L. Shannon, Extension Manager U.S. Atomic Energy Commission Division of Technical Information Ext. P. O. Box 62 Oak Ridge, Tennessee 37831	2
Defense Metals Information Center Battelle Institute 505 King Avenue Columbus, Ohio 43201	1
Commanding Officer U.S. Army Materials Research Agency ATTN: AMXMR-Technical Information Center Watertown, Mass. 02172	2
Commanding General Aberdeen Proving Ground ATTN: AMXCC - Dr. C. Pickett AMXCC - Technical Library Maryland 21003	1 1
Commanding Officer U.S. Army Mob Equip Research & Dev. Center ATTN: Technical Documents Center Fort Belvoir, Va. 22060	2
Commanding General U.S. Army Electronics Command Fort Monmouth, New Jersey 07703	1

No. of
Copies

Commandant HQ, U.S. Army Aviation School ATTN: Office of the Librarian Fort Rucker, Alabama 36362	1
Commanding Officer Frankford Arsenal Philadelphia, Pa., 19137	1
Commanding Officer Picatinny Arsenal Dover, New Jersey 07801	1
Commanding General Redstone Arsenal ATTN: Documentation & Technical Information Branch AMSMI-RRS AMSMI-RKK AMSMI-RSM Alabama 35809	2 1 1 1
Commanding Officer Plastics Technical Evaluation Center ATTN: SMUPA-VP3 Picatinny Arsenal Dover, New Jersey 07801	1
Commanding Officer Watervliet Arsenal ATTN: SWEWV-RDR Dr. M. Hussain SWEWV-RDR Dr. J. H. Underwood SWEWV-RDR Mr. J. F. Throop Watervliet, New York 12189	1 1 1
Mr. George Vrooman SWEWV-RDT-6 Document Libraries, Watervliet Arsenal Watervliet, New York 12189	1
Mr. Charles Eldridge Structures and Mechanics Laboratory Research and Development Director U.S. Army Missile Command Huntsville, Alabama	1
Mr. John G. Merkle Building 9204-1 Oak Ridge National Laboratory P. O. Box Y Oak Ridge, Tenn. 37830	1
Mr. J. G. Kaufman Alcoa Research Laboratory P. O. Box 772 Freeport Rd. New Kensington, Pa. 15068	1

No. of
Copies

Mr. E. Ken Lynn
Materials Engineering Branch
Directorate of Licensing
Regulatory BETH-008
USAEC-L
Washington, D. C. 20545

1

Dr. T. D. Dudderar
Room 1A-105
Bell Telephone Labs
Mountain Avenue
Murray Hill, N. J. 07971

1

Mr. W. F. Brown
NASA
Lewis Research Center
Cleveland, Ohio 44135

1

Dr. Royce Forman
NASA
Manned Spacecraft Center
Houston, Texas 77058

1

Dr. F. W. Smith
Dept. of Mechanical Engineering
Colorado State University
Fort Collins, Colorado

1

Mr. N. G. Tupper
AFFDL/FBA
Wright-Patterson AFB, Ohio 45433

1

NASA Langley Research Center
Hampton, Va. 23365
ATTN: Dr. J. R. Davidson

1

Mr. Howard Wood
AFFDL/FBA
Wright-Patterson AFB, Ohio 45433

1

Mr. Al Gunderson
AFFDL/FBA
Wright-Patterson AFB, Ohio 45433

1

Dr. N. Basdekis
Office of Naval Research
Mathematics and Information Sciences Division
Structural Mechanics Branch
800 N. Quincy Blvd.
Arlington, Va. 22217

1

Dr. J. Pomerantz
U.S. Air Force Office of Scientific Research
1400 Wilson Blvd.
Arlington, Va. 22209

1